



BERGISCHE
UNIVERSITÄT
WUPPERTAL

Computational Modeling of Skeletal Muscle in the Hierarchical Microstructure

Genehmigte Dissertation
zur Erlangung des akademischen Grades
Doktor-Ingenieur (Dr.-Ing.)

in der
Fakultät für Maschinenbau und Sicherheitstechnik
der
Bergischen Universität Wuppertal

vorgelegt von
Jens Lamsfuß
aus Wipperfürth

Wuppertal 2023

Dissertation eingereicht am: 25.01.2023

Tag der Disputation: 08.09.2023

Erste Gutachterin: Prof. Dr.-Ing. Swantje Bargmann

Zweiter Gutachter: Prof. Dr. Heiko Wagner

Acknowledgements

The present dissertation was completed under the supervision of Prof. Swantje Bargmann at the Chair of Solid Mechanics, University of Wuppertal, Germany. First of all, I would like to thank Prof. Swantje Bargmann for providing the opportunity to work in the interesting field of biomechanics, for her support and guidance through all these years.

Moreover, I would like to express my appreciation to Prof. Heiko Wagner for kindly accepting to be the second reviewer of this thesis. Thanks for the interest in my work, the careful reading and insightful suggestions. I am very grateful to Prof. Bilal Gökce for being part of the examination committee and to Prof. Axel Schumacher for being chairman of the committee.

Furthermore, I would like to express my deep gratitude to Dr.-Ing. Jana Wilmers and Dr.-Ing. Xianglong Peng for their extensive cooperation and the opportunity for regular professional discussions which were inspirational and have facilitated my research. I would like to thank all my fellow colleagues at the Chair of Solid Mechanics for their friendship, support and diverse contributions to this thesis.

Thanks to my siblings Diana, Sarah and Mark and my parents Andreas and Ute, as their belief in me has kept my spirits and motivation high during this work. Finally, I would like to thank my wife, Aylin, for her endless support, patience and encouragement during the entire work.

Abstract

Muscles are contractile organs referring to their ability to alternate between contracting and relaxing. This interplay of contraction and relaxation enables both the consciously controlled movements and the functions that take place unconsciously inside the body. However, only skeletal muscles can be controlled consciously.

Skeletal muscles are fiber-matrix-composites with a complex hierarchical microstructure, i.e. nested structures exist on different length scales. The components in hierarchically structured materials match together perfectly allowing for an optimal interaction of the individual components with each other resulting in a combination of exceptional properties. Skeletal muscles exhibit a very high elasticity, a high tensile strength as well as a high damage tolerance. The fields of interest for making use of these unique properties range from medicine for body-like prostheses to even advanced robotics. In order to gain a better understanding of the interaction between the components on different hierarchical levels and how individual components impact the overall behavior of the skeletal muscle as a whole, the muscle needs to be studied at different length scales.

In order to enable the analysis of how the muscle works at different length scales, Python codes are created in this dissertation which generate computer models in Abaqus FEA on each of the five hierarchical levels of a skeletal muscle (see Chapter 2).

Some of the created models are used to analyze the hierarchical levels “muscle fiber” and “fascicle” in the chapters 3-5 in more detail by developing constitutive models on these levels and using the finite element method to predict the material behavior in multiphysics simulations. The fascicle models are considered as two-phase composites consisting of muscle fibers embedded in the connective tissue endomysium. Hyperelastic material models are developed to describe the material behavior of both components. The material behavior of the muscle fiber is subdivided into a passive and an active part, since the electrical activation of muscle fibers to initiate contraction results in strongly different material behavior compared to the one of passive relaxed muscle fibers. The models intend to provide detailed information on the material behavior of the entire fascicle as well as on its components, muscle fiber and endomysium.

In Chapter 3, a chemo-electro-mechanical model with a representative volume element (RVE) for fascicles is introduced. By considering the activation process of muscle fibers, which consists of strongly coupled chemical, electrical and mechanical processes, the impact of the temporal and spatial change of the activation level in fibers on the stress development in the muscle fiber and in the endomysium is examined. Furthermore, a real loading case of fascicles is considered and the influence of the pennation angle on the lifting force and lifting height of unipennate muscles is investigated. For the same loading case, the local minimum and maximum strains and stresses in the muscle fiber and endomysium are analyzed with increasing macroscopic strain to identify areas with high risk of damage.

Chapter 4 examines the damage behavior during eccentric contraction on muscle fiber and fascicle level on which the most common serious muscle injuries occur. Two differently sized

two-phase fascicle RVEs with electrically activated muscle fibers are used to model the crack propagation and damage evolution in a pre-damaged muscle fiber and to investigate the interaction between muscle fiber and endomysium. The used multiscale continuum model allows to study the influence of the giant molecule titin of the lowest hierarchical level on the mechanical behavior in pre-damaged fascicles. In addition, endomysium's protective properties for neighboring undamaged muscle fibers in a case of a highly pre-damaged fiber are examined.

Chapter 5 studies the thermomechanical behavior of muscle fibers and endomysium in fascicles. Detailed information is provided on the mechanisms of heat and cold treatment in trigger points (hyperirritable spots in tensed muscle fibers) to relieve muscle tension. For this purpose, a complete two-phase cylindrical fascicle model is generated and a trigger point is induced in the central muscle fiber. The effect of short-term and long-term heat and cold treatment of the entire fascicle on the strains and stresses along the tensed central muscle fiber is simulated. The aim of the study is to investigate how the different thermomechanical behavior of the trigger point and the neighboring fiber regions impacts the thermal treatment of trigger points.

Zusammenfassung

Muskeln sind kontraktile Organe, d.h. sie sind in der Lage sich zusammenzuziehen und wieder zu entspannen. Dieses Wechselspiel von Anspannung und Entspannung ermöglicht sowohl die bewusst gesteuerten Bewegungen als auch die unbewusst ablaufenden Funktionen im Körper, allerdings kann nur die Skelettmuskulatur bewusst angesteuert werden.

Skelettmuskeln sind Faser-Matrix-Komposite mit einer komplexen hierarchischen Mikrostruktur, d.h. ein verschachtelter Aufbau auf verschiedenen Längenskalen existiert. Die Komponenten von hierarchisch aufgebauten Materialien sind perfekt aufeinander abgestimmt, sodass ein optimales Zusammenspiel der einzelnen Komponenten erreicht wird. Daraus resultieren herausragende Eigenschaften, was sich beim Skelettmuskel durch eine hohe Elastizität, Zugfestigkeit und Schädigungstoleranz bemerkbar macht. Aufgrund der einzigartigen Eigenschaften herrscht auf vielen Gebieten großes Interesse am Einsatz von skelettmuskelähnlichen, künstlichen Materialien, z.B. für körperähnliche Prothesen in der Medizin oder für humanoide Roboter, vor allem für Soft Robots, in der Technik. Um ein besseres Verständnis über das Zusammenspiel der Komponenten auf verschiedenen Hierarchieebenen und den Einfluss einzelner Komponenten auf das Gesamtverhalten des Skelettmuskels zu erlangen, muss der Skelettmuskel auf unterschiedlichen Längenskalen untersucht werden.

Um die Arbeit auf verschiedenen Längenskalen des Skelettmuskels zu ermöglichen, werden in der vorliegenden Dissertation vorerst Python Codes zur Generierung von Computermodellen in Abaqus FEA auf jeder der fünf Hierarchieebenen des Skelettmuskels erstellt (siehe Kapitel 2).

Ein paar der erstellten Modelle werden verwendet, um in den Kapiteln 3-5 die Hierarchieebenen „Muskelfaser“ und „Muskelfaserbündel“ genauer zu untersuchen. Hierfür werden konstitutive Modelle aufgebaut und multiphysikalische Simulationen mit der Finiten Elemente Methode durchgeführt, um Vorhersagen über das Materialverhalten treffen zu können. Das Muskelfaserbündel wird als zweiphasiges Modell, bestehend aus Muskelfasern, welche in das Bindegewebe Endomysium eingebettet sind, erstellt. Zur Beschreibung des Materialverhaltens werden für beide Komponenten hyperelastische Materialmodelle verwendet. Dabei wird im Materialmodell der Muskelfaser zwischen passiven und aktiven Eigenschaften unterschieden, da die elektrische Aktivierung zur Bewegungsansteuerung von Muskelfasern im Vergleich zur passiven, entspannten Faser zu stark unterschiedlichem Materialverhalten führt. Anhand der Modelle sollen sowohl gezielte Aussagen über das Materialverhalten des gesamten Muskelfaserbündels als auch über dessen Komponenten Muskelfaser und Endomysium getroffen werden.

In Kapitel 3 wird ein chemo-elektro-mechanisches Modell mit einem repräsentativen Volumenelement (RVE) für Muskelfaserbündel erstellt. Durch die Berücksichtigung des Aktivierungsprozesses von Muskelfasern, der eine starke Kopplung aus chemischen, elektrischen und mechanischen Prozessen darstellt, wird der Einfluss des zeitlich und räumlich veränderlichen Aktivierungsgrads der Muskelfaser auf den Spannungsverlauf in der Muskelfaser und im Endomysium genauer untersucht. Des Weiteren wird ein möglichst realer Belastungsfall von Muskelfaserbündeln betrachtet und der Einfluss des Fiederungswinkels auf die Hubkraft und

Hubhöhe von einfach gefiederten Muskeln untersucht. Für den gleichen Belastungsfall werden zudem die lokalen, minimalen und maximalen Dehnungen und Spannungen in der Muskelfaser und dem Endomysium mit zunehmender makroskopischer Dehnung analysiert, um unter anderem Bereiche mit erhöhter Schädigungsgefahr lokalisieren zu können.

In Kapitel 4 wird das Schädigungsverhalten bei exzentrischer Kontraktion auf Muskelfaser- und Muskelfaserbündelebene untersucht, auf denen die meisten schwerwiegenden Muskelverletzungen auftreten. Mit zwei unterschiedlich großen, zweiphasigen Muskelfaserbündel RVEs wird die Rissausbreitung und Schadensentwicklung in einer vorgeschädigten Muskelfaser, die sich innerhalb eines aktivierten Muskelfaserbündels befindet, simuliert und das Zusammenspiel von Muskelfaser und Endomysium untersucht. Das erstellte Multiskalenmodell ermöglicht den Einfluss des Makromoleküls Titin, das sich auf der untersten Hierarchieebene des Muskels befindet, auf das mechanische Verhalten in vorgeschädigten Muskelfaserbündeln zu analysieren. Zudem wird die Schutzfunktion des Endomysiums für benachbarte, ungeschädigte Fasern vor der Rissausbreitung in der geschädigten Faser genauer betrachtet.

In Kapitel 5 wird das thermomechanische Verhalten von Muskelfasern und Endomysium in Muskelfaserbündeln untersucht. Es werden detaillierte Informationen über die Mechanismen von Wärme- und Kältebehandlung von Triggerpunkten (lokale Muskelverhärtungen) in Muskelfasern zur Reduzierung der Muskelverhärtung bereitgestellt. Dafür wird ein komplettes zweiphasiges, zylindrisches Muskelfaserbündelmodell erstellt und ein Triggerpunkt in die mittlere Muskelfaser induziert. Der Einfluss von unterschiedlich langer Wärme- und Kältebehandlung des gesamten Bündels auf die Dehnungen und Spannungen entlang der verspannten Muskelfaser wird simuliert. Ziel der Studie ist die Auswirkung des unterschiedlichen thermomechanischen Verhaltens im Triggerpunkt und in den benachbarten Faserbereichen auf die thermische Behandlung von Triggerpunkten zu analysieren.

List of Papers

This thesis consists of an introduction and four papers about computational modeling of skeletal muscles on microstructure level. The introduction in Chapter 1 provides an overview of the state-of-the-art in skeletal muscle modeling, describes the studied research topics, sums up the main conclusions from the papers and presents an outlook for future research in this field. All papers are published in international scientific peer-reviewed journals. The following four papers are included in the thesis:

Chapter 2 [120]: J. Lamsfuss and S. Bargmann. Python codes to generate skeletal muscle models on each hierarchical level. *Software Impacts*, 14:100437, 2022.

Chapter 3 [118]: J. Lamsfuss and S. Bargmann. Skeletal muscle: Modeling the mechanical behavior by taking the hierarchical microstructure into account. *Journal of the Mechanical Behavior of Biomedical Materials*, 122:104670, 2021.

Chapter 4 [119]: J. Lamsfuss and S. Bargmann. Computational modeling of damage in the hierarchical microstructure of skeletal muscles. *Journal of the Mechanical Behavior of Biomedical Materials*, 134:105386, 2022.

Chapter 5 [121]: J. Lamsfuss and S. Bargmann. Mechanisms of thermal treatments in trigger points of the skeletal muscle: computational microstructural modeling. *European Journal of Mechanics - A/Solids*, 99:104906, 2023.

Contents

1	Introduction	1
1.1	State-of-the-art in skeletal muscle modeling	2
1.2	Research topics of the dissertation	4
1.3	Conclusions and Outlook	6
2	Article 1:	
	Python codes to generate skeletal muscle models on each hierarchical level	10
2.1	Abstract	10
2.2	Code metadata	10
2.3	Code description	11
2.4	Design and methods	16
2.5	Impact	16
3	Article 2:	
	Skeletal muscle: Modeling the mechanical behavior by taking the hierarchical micro-structure into account	18
3.1	Abstract	18
3.2	Introduction	18
3.3	Micromechanical behavior of skeletal muscles	20
3.3.1	Mechanical behavior on levels 1 (sarcomere) and 2 (myofibril)	20
3.3.2	Mechanical behavior on level 3 (muscle fiber)	22
3.3.3	Mechanical behavior on level 4 (fascicle)	23
3.3.4	Mechanical behavior on level 5 (entire muscle)	23
3.4	Micromechanical model	25
3.4.1	Muscle fiber (level 3)	25
3.4.2	Connective tissue endomysium	27
3.4.3	Material Data	28
3.5	3D Computational Model of Fascicle	29
3.6	Results and Discussion	30
3.6.1	Mechanical behavior of fascicles, muscle fibers and endomysium: Loading in fiber direction	31

3.6.2	Mechanical behavior of fascicles and its components in uni-pennate muscles under real loading conditions	35
3.7	Conclusion	42
4	Article 3:	
	Computational modeling of damage in the hierarchical microstructure of skeletal muscles	44
4.1	Abstract	44
4.2	Introduction	44
4.3	Micromechanical damage model	47
4.3.1	Muscle fiber (level 3)	47
4.3.2	Connective tissue endomysium	52
4.4	3D computational models of fascicles	53
4.5	Results: Computational modeling of damage in fascicles	54
4.5.1	Damage behavior and injury of previously fully intact muscle fibers on the fascicle level	54
4.5.2	Damage behavior and injury with pre-damaged muscle fibers on the fascicle level	56
4.6	Discussion	61
4.7	Conclusion	62
5	Article 4:	
	Mechanisms of thermal treatments in trigger points of the skeletal muscle: computational microstructural modeling	63
5.1	Abstract	63
5.2	Introduction	63
5.3	Micro-thermomechanical model	65
5.3.1	Endomysium	66
5.3.2	Muscle fiber	68
5.4	3D computational model of fascicle	70
5.5	Results: Computational modeling of thermomechanical behavior on the fascicle level	71
5.6	Discussion	76
5.7	Conclusion	78
A	Appendix of article 1	80
B	Appendix of article 2	81
B.1	Chemoelectrical part of muscle fiber material model	81
B.2	Further simulation results	83
B.2.1	Influence of the activation parameter $\bar{\gamma}$ on the stress-strain curve of fascicles	83

B.2.2	Interaction of chemoelectrical processes and mechanical processes during fiber activation	84
B.2.3	Total fascicle RVE force in fascicles with varying states of stretch and compression depending on the speed of contraction	85
C	Appendix of article 3	87
C.1	Material Data	87
C.1.1	Muscle fiber	87
C.1.2	Connective tissue endomysium	89
C.2	Further simulation results	89
C.2.1	Damage behavior and injury of muscle fibers loaded in fiber direction . . .	89
C.2.2	Local strains in a 90 % pre-damaged muscle fiber at fascicle level in a realistic loading case	91
D	Supplementary Material of article 3	93
D.1	Validation of titin's and endomysium's observed behavior in pre-damaged fascicles	93
D.1.1	Comparison between different fiber-endomysium-Young's modulus ratios	93
D.1.2	Comparison between different fiber shapes and fiber volume fractions . . .	93
D.2	Initiation of fiber rupture in RVEs with different arranged polygonal muscle fibers .	97
E	Appendix of article 4	99
E.1	Material Data	99
E.1.1	Endomysium	99
E.1.2	Muscle fiber	100
E.2	Influence of temperature on active muscle fiber force	102
E.3	Further results	104
F	Supplementary Material of article 4	108
F.1	Validation of the observed influence of thermal treatment on muscle fibers with trigger points	108
	Bibliography	112

1 | Introduction

Skeletal muscles are hierarchically structured fiber-matrix-composites, so nested structures exist on different length scales. The interaction of the different hierarchy levels results in a combination of a variety of exceptional properties. What makes the skeletal muscle so unique is the combination of high elasticity, high tensile strength and high damage tolerance. Due to these properties, synthetic skeletal muscles with similar characteristics are in high demand for different fields, e.g. for body-like prostheses in medicine or for humanoid robots in technology. In particular, the use of artificial muscles is regarded as a crucial element for “soft robots” which consist of flexible, organic structures and rely on the imitation of movement sequences found in nature. Therefore, powerful, flexible and light muscles will allow the replacement of heavy motors in the field of technology. Understanding the mechanics of skeletal muscles enables to look beyond the field of technology and apply the gained knowledge when analyzing the prevention of sports injuries and rehabilitation. Due to the wide range of applications and the unique properties of skeletal muscles, worldwide interest has arisen in order to examine this biological material in more detail.

The complex structure of skeletal muscles consisting of connective tissue, blood vessels, nerves and contractile material is subdivided into five hierarchical levels [99, 124, 155, 190], where, visually speaking, level 5 corresponds to the most macroscopic layer: skeletal muscle (hierarchical level 5) - fascicle (hierarchical level 4) - muscle fiber (hierarchical level 3) - myofibril (hierarchical level 2) - sarcomere (hierarchical level 1) (Fig. 4.1 in Chapter 4 shows the complex structure of skeletal muscles on all levels). Fascicles and muscle fibers are both embedded in a connective tissue matrix. On the lower levels, myofibrils consist of parallel aligned contracting units, called sarcomeres. Sarcomeres contain multiple protein filaments which are responsible for the entire muscle movement.

In the past, vast numbers of experimental investigations have been performed on skeletal muscles. As experimental sample sizes and mechanical loading rates are restricted, experiments are limited by length and time scales. Furthermore, detailed examinations of the microstructure often cause major challenges for experiments, which is why computational modeling of solid materials based on the theory of continuum mechanics provides us with a high potential alternative, as it is not constricted by length and time scales. For computational modeling, the structure of materials can be modeled on a macroscopic and microscopic level and material models can be developed which describe the physical properties of either the entire structure or specific components via

constitutive equations. Constitutive equations describe the material response to external stimuli by relating two physical quantities to each other, as e.g. stresses to strains.

In many continuum mechanical muscle models, the constitutive equations for muscles have been divided into a passive and an active part. The active part contains the active properties of muscle fibers, which are stimulated by electrical impulses from the brain to induce the shortening or lengthening of the muscle fiber.

When a muscle is compressed or stretched, the muscle exerts passive forces, which are mainly generated by the connective tissues. Thus, the passive part is mainly represented by the properties of the connective tissues.

1.1 State-of-the-art in skeletal muscle modeling

Computational models can be used to study the skeletal muscle on different length scales, i.e. on different hierarchical levels, to predict the mechanical behavior of different components and their interaction with each other. In the past, most mechanical models examined the skeletal muscle on the highest hierarchical level, which means that the models were generated for the entire skeletal muscle.

Hill [93] was the first who created a mechanical muscle model describing the muscle force in a one-dimensional, three-parameter model. Since then, Hill's model has been expanded in many different one-dimensional mathematical models, e.g. in [83, 217, 221]. Other works [20, 108, 152] have shown, that three-dimensional finite element models are able to capture the functional and structural properties of skeletal muscles more precisely than the developed one-dimensional models. Johansson et al. [108] determined the mechanical properties in all three dimensions of the skeletal muscle, Oomens et al. [152] integrated the sliding-filament theory from [98] to develop a continuum model for contracting skeletal muscles and Blemker et al. [20] determined the influence of different geometrical arrangements of fascicles on their nonuniform shortening behavior. Some finite element models [35, 215] even involved the tendon in their muscle model to analyze the mechanical behavior of the muscle-tendon complex during different contractions [215] and to describe the lengthening and shortening properties of the aponeuroses [35].

However, these macroscopic models do not involve detailed information from smaller scales, which is why micromechanical models were formulated to e.g. describe the influence of muscle fiber distribution on the contraction behavior [21] or depict the activation properties of different fiber types and their influence on contraction and force production [52]. Other models considered the activation process on cellular level [60, 90, 181] by introducing multiphysics muscle models. This allows the connection of the mechanical response of muscles to the electro-physiological mechanisms during muscle fiber activation. In order to cause contraction the tetanic stimulus has to be transferred from the central nervous system to the skeletal muscle fibers, i.e. the complex multiphysical processes take place on multiple scales of the muscle and on multiple parts of the musculoskeletal system.

Röhrle et al. [181] introduced a chemo-electro-mechanical muscle model to combine the extensive electro-physiological cell model for skeletal muscle fibers from [199] with a continuum-based model of muscle mechanics. Shorten et al. [199] described the subcellular processes from electrical excitation to contraction and force generation for different fiber types via a large set of ordinary differential equations. Heidlauf and Röhrle [87, 88] extended the model from [181] by integrating a permanent interaction between the cellular behavior and the continuum-based mechanical model for getting more realistic results during the contraction process. Both, the temporal development of muscle fiber activation and the spatial propagation of the electrical activation impulses are considered in their models which impact the stress development along a muscle fiber. However, the model is based on the approach, that the entire muscle consists of one-dimensional muscle fibers to solve the electro-physiological cell model which are embedded in a three-dimensional structure for the mechanical model. Thus, interactions between muscle fibers and connective tissue cannot be captured.

In order to gain essential insight of muscle structures, a more realistic consideration of the muscle structure on different length scales is necessary. Thus, some muscle models [115, 203, 238] used a more realistic muscle shape by modeling the skeletal muscle as a fiber-matrix composite consisting of three-dimensional muscle fibers and connective tissue. Spyrou et al. [202, 203] used homogenization techniques for the three-dimensional muscle composite to study the active and passive homogenized muscle response at finite strains.

The damage behavior of entire skeletal muscles has not yet been analyzed extensively in mechanical models. Ito et al. [103] considered anisotropic damage in their constitutive muscle model based on the framework of continuum damage mechanics to predict the breaking points at high strains. Computational models mainly studied the thermomechanical properties of artificial muscles, e.g. [111, 163, 196]. Only Bielak et al. [17] included thermomechanical reactions in a continuum model for the gastrocnemius muscle and Fahmy [59] captured the bio-thermomechanical behavior of anisotropic soft tissues in general.

All previously mentioned works focused on the overall behavior of the entire muscle (hierarchical level 5), thus lacking on investigating the remaining four hierarchy levels. Most mechanical models have insufficiently investigated the muscle's microstructure, although knowledge about the intrinsic microstructure of the hierarchically structured muscle is required in order to obtain more information about the mechanical properties of lower level components. Therefore, a few models were developed on specific hierarchical levels and included details about the structure and the material properties on these levels, for instance, [69, 133, 195, 208, 219] generated models on fascicle level (hierarchical level 4), [70, 175, 237] on muscle fiber level (hierarchical level 3) and [33, 154, 173, 205] on myofibril (hierarchical level 2) and sarcomere level (hierarchical level 1).

On hierarchical level 4, Sharafi et al. [195] varied fiber and fascicle shapes, Teklemariam et al. [208] redistributed activated muscle fibers belonging to one motor unit and Marcucci et al. [133] used different muscle fiber types to determine their influence on the mechanical properties on this level. Other works [69, 219] investigated the damage behavior on fascicle level. Gao et

al. [69] studied the lateral force transmission between an injured and a healthy muscle fiber and Virgilio et al. [219] examined disease-related changes in fascicles.

On hierarchical level 3, Rehorn et al. [175] developed a mathematical model of muscle fiber viscoelasticity for different lengthening rates. Zhang and Gao [237] generated a 2D finite element model of a muscle fiber to investigate the mechanisms of lateral force transmission between the muscle fiber and the endomysium. The damage behavior was also studied on muscle fiber level. Here, Gao et al. [70] analyzed the susceptibility to damage during lengthening contraction.

The mathematical models for myofibrils (hierarchical level 2) [205] and for sarcomeres (hierarchical level 1) [33, 154, 173] incorporated the cross-bridge dynamics to provide more detailed insights into muscle mechanics on the lower hierarchical levels. The cross-bridge dynamics describes the cycle of attachment and detachment of the proteins actin and myosin in sarcomeres through cross-bridges. The rotating cross-bridges ensure the movement of the proteins and are therefore directly responsible for the contraction of the entire muscle fiber.

These mentioned microstructure models were able to describe the mechanical behavior on specific hierarchical levels. However, further details about the properties of microstructure components lack, as well as more information about the interaction of the components and their impact on the overall skeletal muscle behavior.

1.2 Research topics of the dissertation

The objective of this dissertation is the generation and investigation of microstructure muscle models utilizing the finite element method in order to obtain a more detailed understanding of lower level muscle component properties.

To this end, Chapter 2 introduces Python codes to create computer models for each of the five hierarchical skeletal muscle levels. A selected number of these models are used as the basis of the investigation in the articles shown in the following chapters and the codes are also available for future works on microstructure level. The skeletal muscle is extensively examined on muscle fiber level (hierarchical level 3) and on fascicle level (hierarchical level 4) in Chapter 3-5, which means an in depth analysis of the fascicles, muscle fibers and the endomysium within this dissertation. On these levels, the influence of complex multiphysical processes in the muscle on the properties of the muscle's components are investigated as well as the damage behavior of these components. Especially the damage behavior is of interest as the most common serious muscle injuries occur on these levels. The individual components that represent the muscle geometry on the hierarchical levels are considered in the models and constitutive material models are formulated separately for each component.

During muscle fiber activation, strongly coupled chemical, electrical as well as mechanical processes result in contraction of the entire muscle fiber. These complex multiphysical processes can be captured in models on hierarchical levels 3 and 4.

In the model developed in Chapter 3, the complex activation process in a muscle fiber is integrated by using the extensive cellular model from [199], as done in [88]. The model of [88]

is then extended to the three-dimensional case in order to capture the interaction between the muscle fiber and the surrounding tissue endomysium during fiber activation. The stress evolution along a muscle fiber during activation is investigated to study the expected inhomogeneous stress distribution along fibers and the resulting impact on the endomysium. The endomysium is expected to compensate for the stress differences along the muscle fiber.

Most mechanical models mentioned in Sect. 1.1 focus in their analysis on a muscle under uniaxial loading, although, real muscle loading is usually more complex. Especially pennate muscles experience multiaxial loading consisting of combined tensile and shear loading which is examined more closely in Chapter 3 of this dissertation. If unipennate muscles are stretched in tendon direction and are thus exposed to multiaxial loading, the pennation angle (i.e. the angle between fibers and the tendon) reduces (see Fig. 3.10). As muscle fibers generate forces in fiber direction, the changed pennation angle influences the lifting force, which is the generated force transferred in tendon direction. Furthermore, the pennation angle affects the lifting height of unipennate muscles. It is well known that unipennate muscles with larger pennation angles can exert higher lifting forces while smaller pennation angles result in higher lifting heights. In this dissertation, fully activated fascicles of unipennate muscles are subjected to real loading and the simulations give new insights into the development of lifting forces and lifting heights for different pennation angles during the loading process. As the multiaxial loading results in nonuniform stresses and strains in the activated muscle fiber and in the endomysium, this study, specifically for unipennate muscles, helps to determine regions at higher risk of damage resulting from those higher stresses and strains.

Furthermore, a micromechanical damage model is developed in Chapter 4 to further investigate the high-risk regions for damage of multiaxially loaded unipennate muscles identified in Chapter 3. So far, the damage behavior of the skeletal muscle, especially on different hierarchical levels, has not been fully studied. It is mandatory to gain a detailed understanding of the damage behavior in order to improve in many fields, e.g. the prevention and appropriate treatment of muscle injuries in sports and the development of equivalent synthetic counterparts in biomimetics. Only a few mechanical models developed so far have investigated the damage behavior of skeletal muscles. However, computational models are essential to study the damage behavior of lower level components as experiments can only provide limited information on microstructure level. Therefore, this dissertation examines damage on level 3 and 4 in the muscle belly by means of a damage model for fascicles (see Chapter 4). The same multiaxial loading of unipennate muscles, as studied in Chapter 3, is applied to capture the higher-risk regions for damage in a muscle fiber. It is expected that the simulations confirm the results from Chapter 3.

Furthermore, the damage evolution in muscle fibers until total fiber rupture is analyzed for pre-damaged fibers by taking into account the influence of components on the lowest hierarchical level, especially of the giant protein titin. Here, an eccentric contraction of fascicles is observed, which generally leads to a high risk of injury. In the last few decades, titin has played a major role in the field of muscle research due to its outstanding properties. Because of titin's strongly nonlinear stress-strain relation, it is expected to strongly affect the damage evolution in highly

stretched fascicles.

Moreover, endomysium's role in pre-damaged fascicles is analyzed, specifically, whether or not endomysium impacts the propagation of muscle fiber damage to neighboring undamaged fibers.

Changes in temperature have a unique impact on the mechanical properties of the skeletal muscle's microstructure. Until now, no mechanical models have studied the temperature dependent muscle behavior on the microstructure, thus, less information about the thermomechanical properties of lower level muscle components exist which makes investigations in this field quite interesting. This is why in Chapter 5 a thermomechanical fascicle model considering a tensed muscle fiber is generated to analyze the impact of heat and cold treatment on the muscle fiber tension. Here, a myofascial trigger point, which is a hyperirritable spot in a tensed muscle fiber, is integrated in the fascicle model. Trigger points in human muscles, which often induce tension headaches, can be treated by thermotherapy or cryotherapy to relieve muscle pain. The thermomechanical fascicle model aims to investigate the mechanisms of heat and cold treatments to reduce muscle tension in trigger points, just as in human muscles, by observing the stress and strain development along the entire tensed muscle fiber during thermal treatment. The results will help to understand why applying heat or cold has a positive impact on trigger points. The thermal expansion coefficient of materials indicates whether heating or cooling causes expansion or contraction in the material resulting either in compressive or tensile stresses. Materials usually show contrary behavior in terms of expansion and contraction if heat or cold is applied. Therefore, it needs to be studied why both treatments apparently reduce the tension in the trigger point of human muscles.

1.3 Conclusions and Outlook

In the dissertation, multiscale continuum models on the skeletal muscle's microstructure were developed to study the multiphysical and damage behavior on muscle fiber and fascicle level (see Chapters 3-5). Compared to existing works in the field of muscle modeling, this dissertation investigated in detail the properties of the muscle's microstructure in the fields of damage and thermomechanics. As the properties of muscles are particularly unique in these fields, the gained knowledge provides helpful insights for a better understanding of the muscle's properties on microstructure level.

Several three-dimensional two-phase fascicle structures were generated, including different sized representative volume elements and entire fascicle models which consist of muscle fibers with circular or polygonal cross-section embedded in the connective tissue endomysium. Some of these structures were generated by the Python codes introduced in Chapter 2. The material behavior of the components muscle fiber and endomysium were captured separately in material models for each component.

Chemo-electro-mechanical model

In Chapter 3, the chemo-electro-mechanical processes during muscle fiber activation were captured in a fascicle RVE and the stress development in the fiber and the endomysium during activation was studied. The results confirmed the expected outcome that endomysium compensates for the stress differences along the muscle fiber during fiber activation. Due to the slightly inhomogeneous stress distribution along the fiber and the endomysium, the stress differences during activation can be neglected for further investigations and, consequently, the stresses along the fiber and the endomysium can be considered as constant.

Additionally, a real loading of unipennate muscles consisting of tensile and shear loading was considered and the influence of the pennation angle of different unipennate muscles on the mechanical behavior was studied. For this purpose, the fascicle model used to study the impact of the activation process was subjected to real loading. The detailed observation of the lifting forces and lifting heights with increasing macroscopic strain enabled conclusions regarding the optimal functionality of unipennate muscles:

Optimal fiber arrangements in fascicles are obtained with either very small or very large pennation angles. Small angle changes at small pennation angles have a significant impact on the lifting height while neglectable impact on the lifting force is observed. In contrast, when analyzing small angle changes at large pennation angles, a significant impact on the lifting force can be seen while the lifting height remains almost constant.

Nonuniform stresses and strains exist in the fiber and the endomysium during real loading of unipennate muscles (as expected in Sect. 1.2) and in case of the muscle fiber, the location of the maximum and minimum stresses changes with increasing macroscopic strain (for more information, see Fig. 3.14 in Chapter 3). The analysis of local stresses and strains showed that regions of thin endomysium as well as the fiber edges, i.e. the sarcolemma membrane, are at high risk of being damaged.

Damage model

In Chapter 4, a continuum mechanical damage model for fascicles was introduced and two differently sized fascicle RVEs were subjected to a realistic loading case of unipennate muscles. The model confirmed the findings in Chapter 3 that the susceptibility to muscle damage is highest at the fiber boundary.

The role of titin and endomysium in pre-damaged muscle fibers was investigated for an eccentric contraction. The expectations from Sect. 1.2 have been proven that the giant molecule titin on the lowest hierarchical level has a huge impact on the further progression of damage in muscle fibers. The significantly increasing stiffness of titin results in a strong protection of damaged fiber regions from large strains and therefore provides important protective properties for pre-damaged muscle fibers. This results in the fact that titin prevents more serious injuries even for strongly pre-damaged muscle fibers and enables similar macroscopic strains until fiber rupture as in undamaged fibers. Furthermore, the developed model captured the impact of

endomysium on damage propagation to neighboring undamaged fibers. Endomysium protects undamaged muscle fibers from the high strains in the pre-damaged ones thus inhibiting damage of neighboring fibers.

Thermomechanical model

In Chapter 5, a continuum thermomechanical model for fascicles was generated to study the influence of thermotherapy and cryotherapy on a tensed muscle fiber. Here, an entire fascicle with circular cross-section was modeled and a trigger point was induced in the central muscle fiber.

The application of heat or cold yielded the result, that short-term heating supports the relief of muscle tension while short-term cooling shows the opposite behavior as it causes increasing compressive stresses and strains. In conclusion for short-term treatment with an assumed constant electromyography (EMG) activity in the trigger point, the results showed a contrary behavior for heating and cooling as expected for standard materials. Specifically for the case of heat treatment, the sign combination of the different thermal expansion coefficients along the tensed muscle fiber (the thermal expansion coefficient of the trigger point has a positive value while the thermal expansion coefficient of the neighboring fiber regions in the same muscle fiber has a negative value) causes maximum relief of muscle tension (for more information, see Fig. 5.8 in Chapter 5).

The additional reduction of EMG activity in the trigger point during long-term thermal treatment results in a stiffness reduction in the trigger point. This softening strongly influences the behavior along the entire tensed fiber which leads to a significant decrease of the stresses and strains during heating as well as during cooling. The entire fiber contributes to reduced muscle tension for both treatments despite the disadvantageous thermal expansion coefficient combination for cooling. For this reason, both, thermotherapy and cryotherapy, can be used to treat trigger points, as already mentioned in Sect. 1.2. As there is no risk in choosing the right thermal treatment nor does the application of these treatments need professional assistance, thermal treatment has a considerable benefit compared to alternative methods.

Outlook

The research presented in this dissertation facilitated predictions about the mechanical properties on the hierarchical levels 3 (muscle fiber) and 4 (fascicle). For future studies, the Python codes introduced in Chapter 2 can be used to create computer models on all hierarchical levels to provide more details about the components and their interaction with each other on different levels.

The introduced damage model in Chapter 4 could be extended to more complex damage models in order to be able to analyze different muscle injuries. According to the results published in Chapter 3 and 4 of this dissertation, the muscle fiber-endomysium interface in the muscle belly is at highest risk of injury, therefore, more detailed investigations about the damage behavior in and closely around these areas should be of future interest. Since connective tissues are also

commonly affected by muscle injuries, damage models should be developed for connective tissues as well to study their damage behavior in upcoming works. Scar tissue forms during the healing of injured connective tissue and as the properties of this tissue differ from the original connective tissue, the implementation of those properties into mechanical models are of future interest as well. These mechanical models can analyze the mechanical behavior of the scar tissue and its impact on the entire muscle, e.g. the susceptibility to injury of the scar tissue or its effects on other muscle components.

In addition to further investigations of the muscle's damage behavior by mechanical models, the thermomechanical model introduced in Chapter 5 of this dissertation should be used to gain insights on the thermal treatment of differently tensed skeletal muscles. The model can readily be applied to more complex examples of tensed muscles, e.g. to muscles with more trigger points.

Moreover, the injury susceptibility of skeletal muscles and the location of crack initiation for different muscle temperatures can be examined. Here, micromechanical models can provide more details about the mechanisms influencing the injury susceptibility for different muscle temperatures, as it is well known that skeletal muscles need to be warmed up to reduce the risk of damage during sports activity. Therefore as a next step, the temperature dependence of the stiffness should be included in the model, as higher temperatures result in softer muscle behavior thus influencing the outcome. Moreover, the outstanding maximum isometric stress-temperature curve of skeletal muscles needs to be considered which is already integrated in the model shown in Chapter 5. As this behavior strongly differs from standard materials, it turns the human muscle into a unique complex system and, therefore, its influence on the mechanical properties should be investigated in more detail during future studies.

2 | Article 1:

Python codes to generate skeletal muscle models on each hierarchical level

2.1 Abstract

Python codes are provided for generating computer models of the skeletal muscle on all five hierarchical levels. All scripts are parametrized to generate a large variation of muscle structures. On hierarchical levels 3 (muscle fiber), 4 (fascicle) and 5 (muscle), we use Voronoi tessellation in combination with the sunflower seed arrangement to obtain fiber-matrix-composite models with similar-sized fibers having polygonal cross-sections. The muscle and its microstructure can be studied at a given length scale or in multiscale analysis. The codes provide the basis for a large variety of possible FEM simulations of different phenomena due to full parametrization and flexibility.

2.2 Code metadata

Current code version	V1
Permanent link to code/repository used for this code version	https://github.com/SoftwareImpacts/SIMPAC-2022-217
Permanent link to reproducible capsule	
Legal code license	MIT License
Code versioning system used	git
Software code languages, tools and services used	Python
Compilation requirements, operating environments and dependencies	Python 3 with the libraries matplotlib, numpy, scipy and shapely; Abaqus FEA to generate the CAD models
If available, link to developer documentation/manual	
Support email for questions	bargmann@uni-wuppertal.de

Table 2.1: Code metadata

2.3 Code description

The skeletal muscle consists of five hierarchical levels [99, 124]: sarcomere (level 1), myofibril (level 2), muscle fiber (level 3), fascicle (level 4) and the muscle (level 5). Our parametrized Python codes allow to generate¹ a large variation of models for each hierarchical level of the skeletal muscle as presented in Fig. 2.1. For the entire muscle, the generated geometry is representative for parallel muscles. The fascicle, muscle fiber and myofibril models can additionally be used to model pennate muscles and the sarcomere is representative for all skeletal muscle shapes. The scripts generate CAD models in Abaqus FEA and can be read into or adapted to directly interface other simulation software.

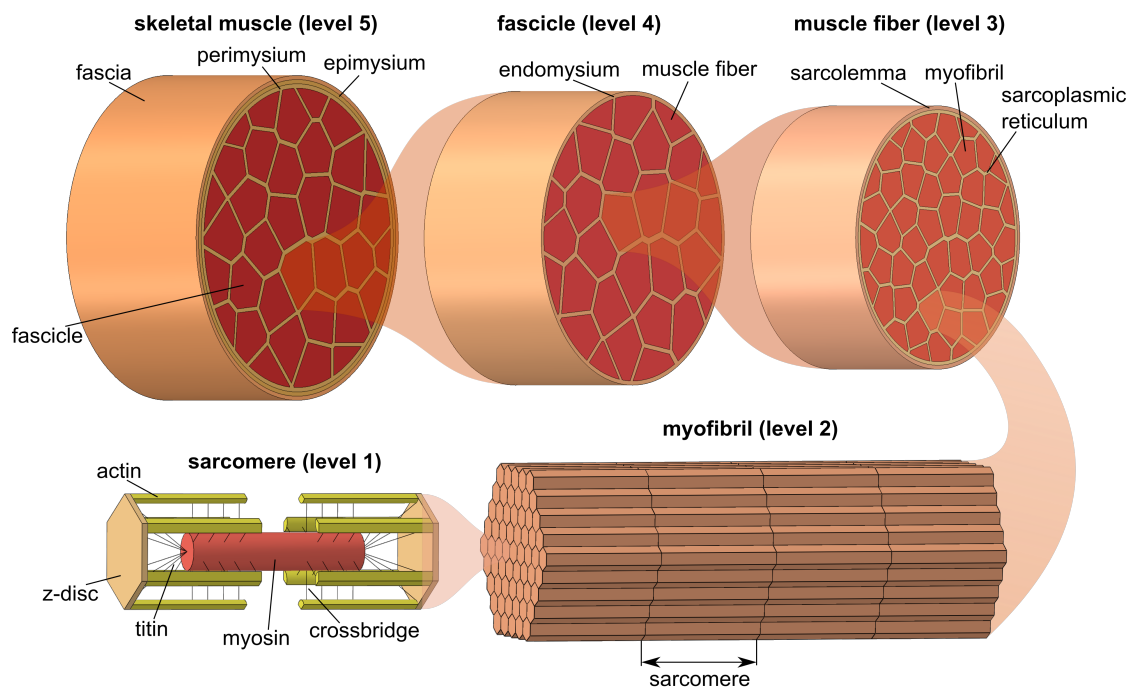


Figure 2.1: Models of the microstructure of skeletal muscles. All five hierarchical levels are shown. Models were generated by the scripts provided in this work. On all levels, the Python codes are able to generate a large variation of the models shown exemplarily.

For each hierarchical level, two python codes are provided. The first one requires only Python to be run and defines the basic geometry of the models. The second script is automatically started after the first code and generates the final models in Abaqus. The scripts enable to create multiple models: The user enters the required number of models and the minimum and maximum values of the parameter to be varied. Then, models are generated in which the parameter is equidistantly distributed in the desired range.

¹see [10] for a review on the generation of representative volume elements

Sarcomere (level 1)

In a myofibril, the region between two z-discs is called a sarcomere. It can be represented by a unit cell (Fig. 2.1) due to its periodic arrangement. The scripts *sarcomere1.py* and *sarcomere2.py* create such a unit cell. Six actin filaments are attached to a thin z-disc with a hexagonal cross-section on both ends of the sarcomere cell. One cylindrical myosin filament is in the center of the model. Crossbridges connect the myosin filament with the actin filaments running perpendicularly. Along the myosin filament, crossbridges always occur in pairs, located opposite to each other. The circular space between two neighboring crossbridge pairs along the myosin filament is 60° [101]. The longitudinal distance between neighboring crossbridges is equidistant and depends on the chosen number of crossbridges as well as the length of the actin-myosin overlap. The latter depends on the lengths of the sarcomere and the myosin and actin filaments – both of which are input parameters and, thus, can be varied in the script.

The z-discs are connected to myosin via six titin filaments. Each titin filament is also connected to one actin filament [67] (see Fig. 2.2). The model is symmetric with respect to the mid-cross-section and the centerline.

Sarcomere cells can be created with a hexagonal cross-section as well as with a circular cross-section (see Fig. 2.2). The circular shape includes entire actin filaments and is used if a complete sarcomere cell is modeled. A hexagonal cross-section allows for periodic arrangement of the unit cell.

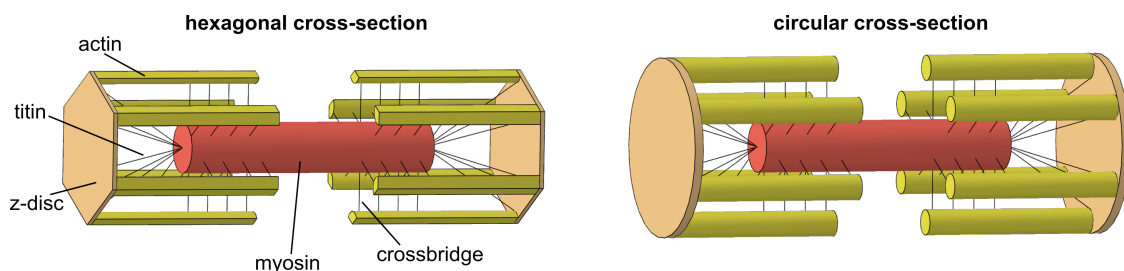


Figure 2.2: Different cross-sections of sarcomere cells can be generated by the scripts. For multiscale modeling purposes, the unit cell with hexagonal cross-section has twelve cut actin filaments and z-discs with half thickness.

The input parameters for the sarcomere model are the length of the sarcomere (“*l_sarcomere*”), the radius (“*r_myosin*”) and the length (“*l_myosin*”) of the myosin filament, the radius (“*r_actin*”) and the length (“*l_actin*”) of the actin filaments, the thickness of the z-discs (“*thickness_z_disc*”) and the length (“*l_crossbridge*”) and the number (“*number_crossbridges*”) of the crossbridges. The requested value for the input parameter “*number_crossbridges*” is reduced automatically if the requirements for crossbridge arrangement cannot be satisfied. The sarcomere length (“*l_sarcomere*”) is the length of the entire model including the z-discs. Additionally, users have to enter “*hex*” (for hexagonal) or “*cir*” (for circular) for the input parameter “*cross_section*”, which defines the shape of the sarcomere cell’s cross-section (see Fig. 2.2).

Myofibril (level 2)

The scripts *myofibril1.py* and *myofibril2.py* generate a myofibril model composed of aligned sarcomeres which consist of equally sized unit cells represented by homogeneous fibers with a hexagonal cross-section (see Fig. 2.3).

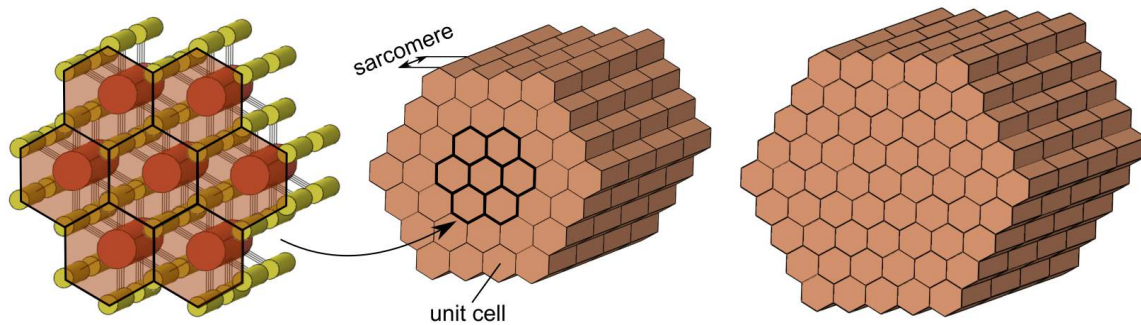


Figure 2.3: The homogeneous unit cells in a myofibril are generated with a hexagonal cross-section. The inner unit cells are completely surrounded circumferentially by further unit cells.

The input parameters of the myofibril model are the length (“*l_sarcomere*”) and the number (“*number_sarcomeres*”) of the sarcomeres, the number of unit cells per sarcomere (“*number_unit_cells_per_sarcomere*”) and the circumradius of the hexagonal cross-section of the unit cells (“*r_unit_cell*”). The requested number for the input parameter “*number_unit_cells_per_sarcomere*” is reduced automatically if it is not sufficient to completely surround inner unit cells.

Muscle fiber (level 3)

The muscle fiber model, which is generated by two scripts *musclefiber1.py* and *musclefiber2.py*, consists of parallel aligned myofibrils surrounded by sarcoplasmic reticulum and the membrane sarcolemma which covers the entire structure. The myofibrils possess a polygonal cross-section and vary in shape. Thus, the sarcoplasmic reticulum between the myofibrils is of nonuniform thickness. Sarcolemma is modeled as a cylindrical hull of constant thickness. By extrusion, a constant muscle fiber cross-section is obtained. The first script *musclefiber1.py* generates the coordinates of the myofibril polygons by Voronoi tessellation and the second script *musclefiber2.py* uses them to create the 3D model of a muscle fiber (see Fig. 2.4).

The input parameters to generate different muscle fibers are the length (“*l_muscle_fiber*”) and the radius (“*r_muscle_fiber*”) of the muscle fiber, the volume fraction (“*vf_myofibril*”) and the number (“*number_myofibrils*”) of myofibrils, the volume fraction of the sarcoplasmic reticulum (“*vf_sarcoplasmic_reticulum*”) and the volume fraction of the sarcolemma (“*vf_sarcolemma*”).

Fascicle (level 4)

The two scripts *fascicle1.py* and *fascicle2.py* generate a fascicle model consisting of parallel aligned muscle fibers embedded in endomysium. The script *fascicle1.py* generates and subse-

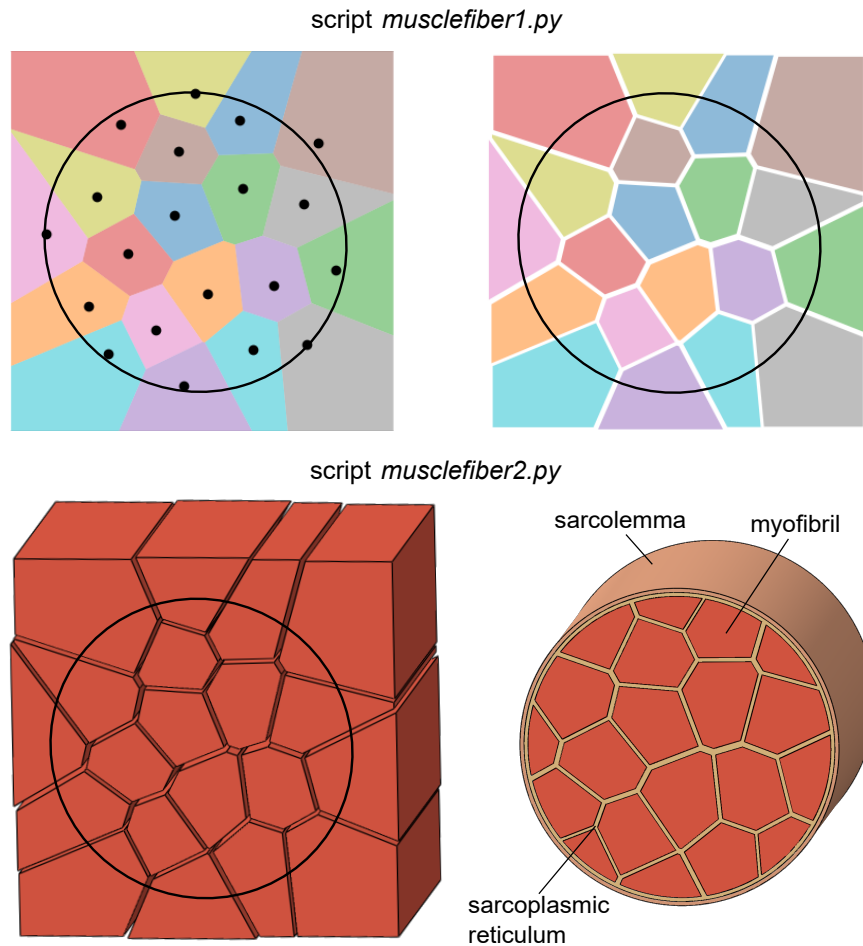


Figure 2.4: Generation of a muscle fiber.

Top left: Script *musclefiber1.py* generates polygons via Voronoi tessellation.

Top right: Subsequently the polygons are shrunk according to the specified myofibril volume fraction. The resulting gaps will later be used to insert sarcoplasmic reticulum between the myofibrils.

Bottom left: Script *musclefiber2.py* first extends the polygons to 3d in Abaqus FEA, i.e. creating myofibril models.

Bottom right: Then, the space (= the sarcoplasmic reticulum) between the myofibrils is filled and a cylinder is cut from the model. As a last step, first a circumferential layer of sarcoplasmic reticulum and, second, a circumferential layer of membrane sarcolemma with constant thickness are added.

quently shrinks polygons by Voronoi tessellation. Those are used in script *fascicle2.py* as cross-sections of the muscle fibers which vary in size and shape. Thus, the endomysium between the fibers is of nonuniform thickness. The cross-section of the fascicle is constant in longitudinal direction. The generation procedure is similar to that for muscle fibers which is illustrated in Fig. 2.4.

The input parameters of the fascicle model are the length (“*l_fascicle*”) and the radius (“*r_fascicle*”) of the fascicle, the muscle fiber volume fraction (“*vf_muscle_fiber*”) and the number of muscle fibers (“*number_muscle_fibers*”).

Muscle (level 5)

The computer model of the entire muscle is constructed in a way similar to the fascicle and the muscle fiber in the scripts *muscle1.py* and *muscle2.py*. Parallel aligned fascicles with polygonal cross-section are embedded in perimysium and covered by two thin-walled structures with constant thickness, the epimysium and the fascia. The fascicle's shape and the thickness of the perimysium vary. Similar to the process illustrated in Fig. 2.4, the script *muscle1.py* utilizes Voronoi tessellation to generate the coordinates of the fascicles' cross-sections and *muscle2.py* uses these coordinates to generate the muscle geometry with constant cross-section in longitudinal direction.

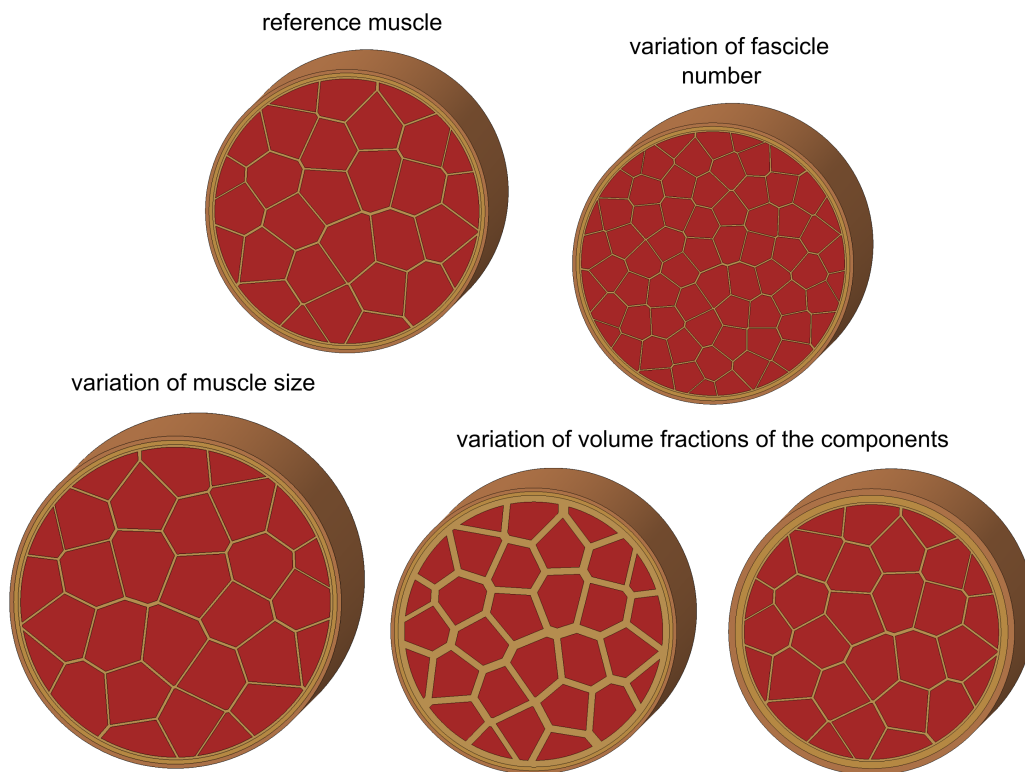


Figure 2.5: The input parameters allow to generate a large number of variations of the skeletal muscle model. The depicted muscle geometries also indicate possible variations on hierarchical levels 3 (muscle fiber) and 4 (fascicle).

The input parameters are the length (“*l_muscle*”) and the radius (“*r_muscle*”) of the muscle, the volume fraction (“*vf_fascicle*”) and the number (“*number_fascicles*”) of fascicles and the volume fractions of the perimysium (“*vf_perimysium*”), the epimysium (“*vf_epimysium*”) and the fascia (“*vf_fascia*”). In Fig. 2.5, various muscle models are depicted to demonstrate the variability of muscle models which can be obtained with the scripts. As the models of levels 3 and 4 are similar to level 5, comparable variations as depicted in Fig. 2.5 are possible on these levels as well.

2.4 Design and methods

For the first script of the hierarchical levels 1-2 (namely, *sarcomere1.py* and *myofibril1.py*), the Python library `numpy` is required. To run the first script of the hierarchical levels 3-5 (namely, *musclefiber1.py*, *fascicle1.py* and *muscle1.py*), the following Python libraries need to be installed: `matplotlib`, `numpy`, `scipy` and `shapely`. These can be downloaded for free. We recommend to work with Python 3 to run the first scripts. For the other scripts, Abaqus FEA and Python are needed without additional Python libraries.

On hierarchical levels 3 (muscle fiber), 4 (fascicle), and 5 (muscle), Voronoi tessellation is used (in *musclefiber1.py*, *fascicle1.py* and *muscle1.py*) to generate polygons formed by radial growth from distributed seed points in the assumed circular cross-sections of the structures. This is done using the sunflower seed arrangement [220] because it allows to create similar-sized polygons (see Fig. 2.4). However, it leads to a rather uniform distribution within the circular area. An additional parameter α yields a more arbitrary distribution of sunflower seeds at the boundary.

Subsequently, all polygons are shrunk according to the specified volume fraction of the polygons. The resulting space between the polygons will later become the connective tissue. The scaling of the slightly differently sized and shaped polygons leads to non-uniform wall thicknesses of the connective tissue, which corresponds to natural tissue variability. The new coordinates of the polygons are saved in a text file and are used as input data in the second script (*musclefiber2.py*, *fascicle2.py* and *muscle2.py*) to create the computer models in Abaqus FEA.

In the first scripts of hierarchical level 1 and 2 (*sarcomere1.py* and *myofibril1.py*), only the input values for all models are saved in text files for the second scripts (*sarcomere2.py* and *myofibril2.py*).

All first codes check the input parameters and indicate incorrect input via an error message. The second scripts of all hierarchical levels can be adapted for usage in any finite element analysis software.

Detailed comments and explanations about the structure generation for each hierarchical level are provided in all scripts.

2.5 Impact

The python codes can be used by researchers in the field of biomechanics, medicine, biology, computational modeling and homogenization, see e.g. [17, 21, 29, 87, 118, 133, 152, 195, 202, 227]. Time-consuming model generation is avoided by providing muscle geometries which can be used readily to perform numerical simulations. The parametrization of the Python codes allows a fast and variable generation of many different skeletal muscle models of various species and, thus, provides the basis for a large variety of FEM simulations. The codes generate muscle structures on each hierarchical level, thus, they can be used independently to study the muscle at a given length scale or together to perform multiscale simulations. The geometries gener-

ated are directly usable in Abaqus FEA and the Python codes for each hierarchical level can straightforwardly be adapted for other finite element analysis software.

Example: Modeling Muscle Damage

Different material models can be used for the models on each hierarchical level generated by the Python codes to model different physical processes on the microstructure, e.g. the chemo-electromechanical behavior during muscle fiber activation [118] or the damage behavior of muscle fibers [119].

Muscular injuries, for instance, occur on different hierarchical levels. Muscle soreness results from damaged z-discs on the lowest hierarchical level (sarcomere), while a completely torn muscle occurs on the highest level (muscle). Using the present generation codes on each hierarchical level, muscle injuries can be modeled on different levels and their influence on the mechanical behavior of the entire skeletal muscle can be investigated.

Multiscale modeling enables consideration of the mechanical properties of lower level components. Via homogenization, the effective properties of damaged lower level models can be determined and used in the modeling of higher hierarchical levels. Thus, information about muscular injuries with different degrees of damage can be obtained, e.g. the effects of muscle soreness (damage on level 1) and torn muscle fibers (injury on levels 3 and 4) on overall muscle behavior or functionality (level 5) can be studied.

3 | Article 2:

Skeletal muscle: Modeling the mechanical behavior by taking the hierarchical microstructure into account

3.1 Abstract

Skeletal muscles ensure the mobility of mammals and are complex natural fiber-matrix-composites with a hierarchical microstructure. In this work, we analyze the muscle's mechanical behavior on the level of fascicles and muscle fibers. We introduce continuum mechanics hyperelastic material models for the connective tissue endomysium and the embedded muscle fibers. The coupled electrical, chemical and mechanical processes taking place in activated contracting muscle fibers are captured including the temporal change of the activation level and the spatial propagation of the activation potential in fibers. In our model, we investigate the material behavior of fascicle, fiber and endomysium in the fiber direction and examine interactions between muscle fiber and endomysium by considering the temporal and spatial change of muscle fiber activation. In addition, a loading case of normal and shear forces is applied to analyze the fiber lifting force and the lifting height of unipennate muscles with different pennation angles. Moreover, the development of local stresses and strains in fibers and endomysium for different strains are studied. The simulation results allow to identify regions in high risk of damage. Optimal arrangements of unipennate muscle microstructure are found for either very small or very large pennation angles.

3.2 Introduction

The interaction of the different hierarchy levels empowers hierarchical materials (i.e., materials with a nested structure on different length scales) to combine a variety of exceptional properties [62, 107, 192, 226, 231]. To this day, natural hierarchical materials outperform their synthetic counterparts. Skeletal muscles stand out due to a very high elasticity as well as a high tensile strength. In addition, they possess a high damage tolerance caused by their high toughness,

which allows them to withstand cracks of millimeter length while almost maintaining their strength [207].

Understanding the mechanics of skeletal muscles is not only of interest in the prevention of sports injuries and rehabilitation, but also in the field of biomimetics. The unique properties of the hierarchically structured skeletal muscle led to researching synthetic counterparts with similar characteristics in different scientific disciplines. For example, light, flexible and powerful synthetic muscles can replace heavy motors in humanoid robots and, therefore, represent a crucial element in soft robots [30, 212]. In medicine, the production of prostheses with material properties similar to skeletal muscle would constitute a major improvement for humans with amputations [218, 225].

The complex structure of skeletal muscles consists of connective tissue, blood vessels, nerves and contractile material and is divided into five hierarchical levels [99, 124, 155, 190]. The entire skeletal muscle (level 5) contains fascicles embedded in the connective tissue perimysium and covered by the connective tissues epimysium and fascia. The fascicles (level 4) are made of muscle fibers surrounded by the connective tissue endomysium. Muscle fibers (level 3) are encompassed by the cell membrane sarcolemma. The myofibrils (level 2) in the muscle fibers consist of aligned functional units called sarcomere. In the sarcomere (level 1), electrical impulses activate small protein filaments and initialize the contraction of the muscle [99].

Skeletal muscle functionality can be divided into active and passive behavior [108, 133, 204, 229], with the sarcomere being the active component. Electrical impulses from the brain stimulate the muscle fiber, trigger the shortening of the sarcomeres and, therefore, lead to active forces in the muscle. If the muscle is actively stretched, the muscle additionally exerts passive forces which are mainly generated by the connective tissues connecting the muscle fibers. Connective tissues allow for sliding processes in the muscle and contribute to a homogeneous force distribution [23]. In injured and diseased states, the adapt by changing the muscle's function [75].

In the past, most mechanical models studied the muscle microstructure in rudimentary form only. The first mechanical model was developed by Hill [93] presenting a one-dimensional, three-parameter model for describing the existing muscle force. Hill's model and extended discrete model formulations [83, 217] were not able to capture the functional and structural properties in detail, such as complex fiber architectures, motor unit fiber distributions or interaction of muscle with the surrounding tissue. Three-dimensional finite element models of skeletal muscles based on continuum mechanics, e.g. [20, 152], yield a better understanding of muscle force distributions. These macroscopic models lacked information about finer scales, e.g. electrophysiological processes on cellular level. Existing electromechanical and chemomechanical models [60, 90, 181, 204] connected the mechanical response of muscles to electro-physiological processes taking place in muscle fibers. These studies considered information from smaller scales, but did not explicitly consider the muscle's hierarchical structure as a composite and instead focused on the overall behavior of the entire muscle (level 5). The influence of the shape of microstructure components has been investigated on different hierarchical levels. Some authors

[115, 202, 203, 238] consider the entire muscle geometry and investigate its mechanical behavior by taking lower level properties into account. Marcucci et al. [133] studied the influence of different muscle fiber types (fast and slow twitch muscle fibers) on the force-velocity properties of the entire bundle. Sharafi et al. [195] analyzed fascicle structure variation (fiber and fascicle shapes) and its influence on the macroscopic muscle behavior, e.g. on the along-fiber shear modulus. Virgilio et al. [219] investigated the influence of disease-related changes on the mechanical properties by variation of fascicle geometries.

In this work, we propose a 3D electro-mechanical, multiscale continuum model for fascicles (hierarchy level 4) to examine and predict their characteristics and those of their components, muscle fiber (hierarchy level 3) and endomysium. We use a unit cell similar to [202] and develop a two-phase finite element model for fascicles in which its individual components muscle fiber and endomysium are modelled separately, as also done by [195]. For the muscle fibers, the electro-mechanically coupled tissue behavior is modelled in the framework of nonlinear continuum mechanics. With this two-phase electro-mechanical, multiscale model, we determine local stresses and strains within the fascicle cross-section and along fiber direction in each component, i.e., muscle fiber and endomysium. We consider the realistic loading case of an extensor digitorum longus (EDL) muscle and study the temporal and spatial variation of the activation degree of the muscle fibers. Regarding the real loading of EDL muscles, we study the influence of different pennation angles on the lifting forces of muscle fibers and the resulting lifting heights. In contrast to Kuthe et al. [116], we investigate how the pennation angle affects the active properties of the fibers rather than the passive properties of the entire skeletal muscle.

Using existing experimental data of EDL muscle behavior and the mechanical properties of lower levels, our physics-based model takes into account the electrical, chemical and mechanical processes in muscle fibers (level 3) during fiber activation. The chemo-electro-mechanical coupling is modelled based on the one-dimensional model by Heidlauf et al. [88] which we extend to the three-dimensional case. This extension makes it possible to consider the muscle fiber's interaction with the surrounding connective tissue endomysium. Therefore, a more realistic description of the entire fascicle including load transfer mechanisms is established.

3.3 Micromechanical behavior of skeletal muscles

In this section, the micromechanical behavior of the skeletal muscle is briefly reviewed. For more detailed information, the reader is referred to e.g. [61, 91, 94, 188].

3.3.1 Mechanical behavior on levels 1 (sarcomere) and 2 (myofibril)

Skeletal muscles exhibit a characteristic force-length relationship between the exerted active force during an electrical activation process and the sarcomere length. Muscles generate maximal forces around the sarcomere's resting length ($\approx 2.0 \mu\text{m}$) [78]: An activation of sarcomeres shorter or longer than this length leads to a reduced active force (Fig. 3.1).

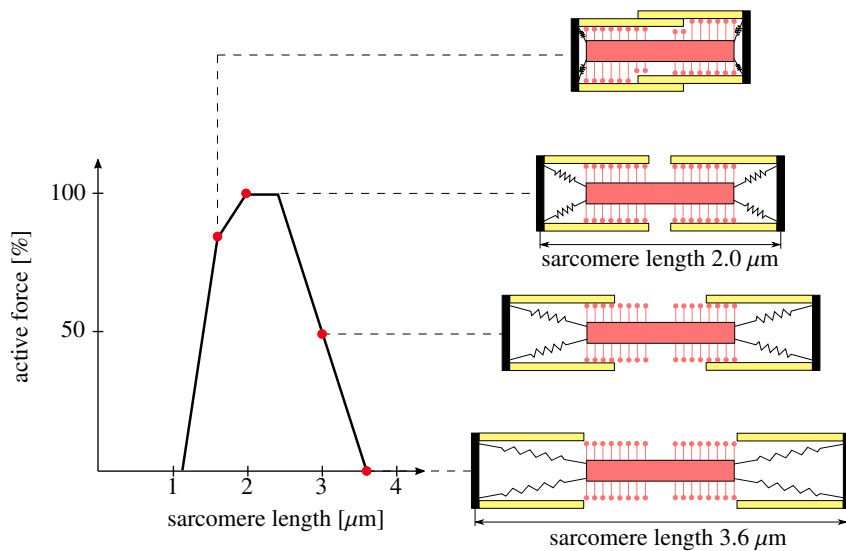


Figure 3.1: Force-length relation: The force generation of a sarcomere strongly depends on its length. The number of myosin heads adhering to actin determines the amount of active force in a sarcomere. Connections by crossbridges only exist if the muscle is electrically activated, otherwise the active force is zero. The more crossbridges connect myosin to actin, the higher the force during electrical activation. In the range of the resting length ($\approx 2.0 \mu\text{m}$), the number of crossbridges is maximal. At lower and higher sarcomere lengths, fewer connections can be formed via crossbridges, thus the force decreases. If there is no crossbridge connection between myosin and actin, the active force is zero.

Electrical impulses from the brain stimulate the muscle fiber and trigger its shortening. The contraction of the fiber is due to the length change of many sarcomeres, resulting from the protein filaments myosin and actin sliding past each other [102]. As multiple sarcomeres act in row, length changes of the individual sarcomeres in the micrometer range lead to shortening of the muscle fiber of several centimeters.

If the muscle is electrically activated, crossbridges connect the myosin to the actin and, thus, generate active forces. Ca. 600 myosin heads per filament attach, rotate around the actin and detach about five times per second [106]. At any given moment, some myosin heads produce force and rotate while the other myosin heads are currently not attached to actin [106]. The number of crossbridge connections is maximal around the resting length ($\approx 2.0 \mu\text{m}$) of a sarcomere. Thus, if the muscle is activated at the resting length of a sarcomere, almost the highest active force is generated although the muscle is undeformed (Fig. 3.1).

The active forces in sarcomeres lead to so-called active stresses. In addition to the active stress, the sarcomere experiences passive tensile stresses. The giant molecule titin acts as a nonlinear spring during a stretching process [81] and, therefore, contributes to the passive forces. In eccentric contraction, i.e., activated muscle fibers are stretched, titin generates additional passive forces, called force enhancement. Two mechanisms can increase titin's stiffness resulting in force enhancement: 1) changing the material property due to the rise of intracellular calcium [117], or 2) reducing titin's free molecular spring length through attachments to the actin filaments (titin-actin interaction) [161]. Moreover, titin acts like a viscoelastic material due

to stress relaxation after stretching and force hysteresis during a stretch-release cycle [140]. This viscoelastic behavior is assumed to result in the viscoelastic response found for an entire myofibril [11, 140].

3.3.2 Mechanical behavior on level 3 (muscle fiber)

The activation mechanism which causes the contraction of the muscle fibers consists of electrical, chemical and mechanical processes which are strongly coupled. During activation, a motor neuron innervates several muscle fibers. A system of motor neuron and associated muscle fibers is called motor unit. Muscle fibers belonging to one motor unit can be distributed throughout the muscle and are activated simultaneously. These fibers are coupled mechanically to all other fibers in the muscle, but are electrically insulated from neighboring fibers.

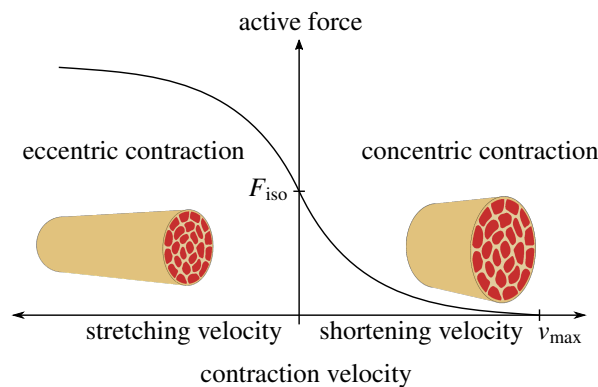


Figure 3.2: Force-velocity relation of skeletal muscle fibers (level 3). In an eccentric contraction, the maximum force is exerted at a high stretching velocity. On the contrary, if the shortening velocity is maximal, the force in muscle fibers is close to zero. In the case that the contraction velocity is zero, the activated muscle fiber is kept at a constant length (isometric contraction).

Muscle fibers behave viscoelastically [51, 175] which can be described by a force-velocity relation as shown in Fig. 3.2, illustrating the dependence of the muscle fiber active force on the velocity of the contraction. The greater the stretching rate of the skeletal muscle fiber, the higher the force [8]. On the contrary, for maximum shortening velocity, the muscle fiber force is approximately zero [93]. This behavior is also observed for the entire muscle [8, 93], but even in these cases it is attributed to the muscle fibers [51, 82].

As mentioned above, there exist active and passive stresses in sarcomeres of stretched and activated muscle fibers. The passive properties of fibers are affected by the lengthening velocity [175]. If the lengthening velocity increases, the passive stress in the muscle fiber increases as well and follows a similar relationship as the active forces shown in Fig. 3.2. This viscoelastic passive behavior during tensile loading is due to the properties of titin rather than those of the crossbridges [11]. The passive stress-strain curve of muscle fibers is linear in the non-activated state, see Fig. 3.3a [224].

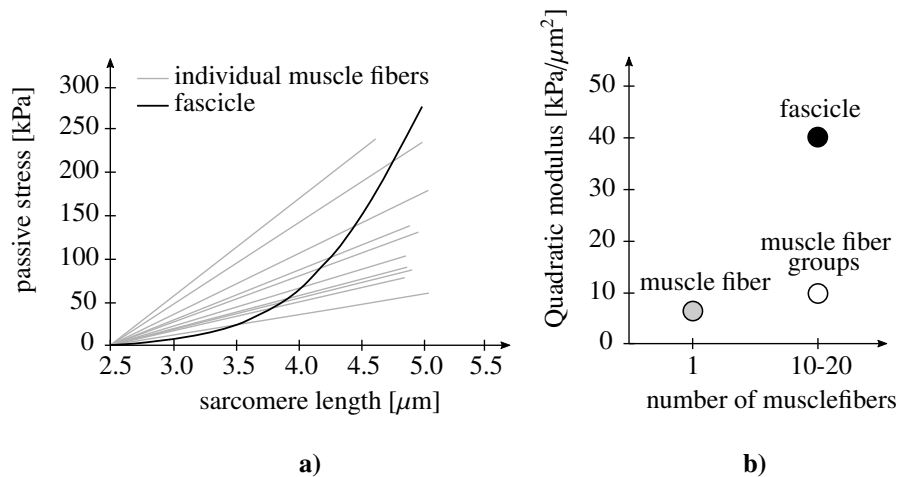


Figure 3.3: Passive mechanical properties of muscle fibers and fascicles in a non-activated state. a) Individual muscle fibers show linear passive stress–sarcomere length relationship. Fascicles, i.e. bundles of muscle fibers and connective tissue, exhibit nonlinear behavior. b) The quadratic modulus describes the curvature of the passive stress–sarcomere length curve for individual muscle fibers, muscle fiber groups and fascicles. It therefore characterizes the nonlinearity of these curves. Muscle fiber groups consist of several muscle fibers without connective tissue. Figure created based on data taken from [138], experiments performed on the 5th toe of the EDL muscle in mice.

3.3.3 Mechanical behavior on level 4 (fascicle)

Fascicles exhibit a strong nonlinear passive stress–sarcomere length behavior. This nonlinearity depends on the additional connective tissue endomysium [138], in particular on the existing collagen fibrils in endomysium changing their orientation if a muscle is stretched [166]. During the stretching process, circumferentially oriented collagen fibers are reoriented in loading direction which results in increased stiffness.

The longitudinal tensile stiffness of endomysium near the resting length of a sarcomere is quite low [166]. As a consequence, endomysium is not capable of transmitting tensile forces of muscle fibers at the sarcomere’s resting length. However, it transmits the contractile force between adjacent muscle fibers by trans-laminar shear through the thickness of the connective tissue [213, 214].

3.3.4 Mechanical behavior on level 5 (entire muscle)

Skeletal muscles (level 5) exhibit a high tensile strength in the fiber direction and sustain strains of more than 150 % without damage [176]. The mechanical behavior of skeletal muscles is velocity-dependent which is commonly explained by the viscoelastic behavior of the muscle fibers (Fig. 3.2).

The stress-strain behavior of the skeletal muscle is illustrated in Fig. 3.4 (solid curve). It results from the superposition of the passive (dashed curve) and the active stress-strain responses (dotted curve). For concentric contraction, the active stress is dominant. The highly nonlinear

passive stress-strain relation (dashed curve) becomes relevant in eccentric contraction.

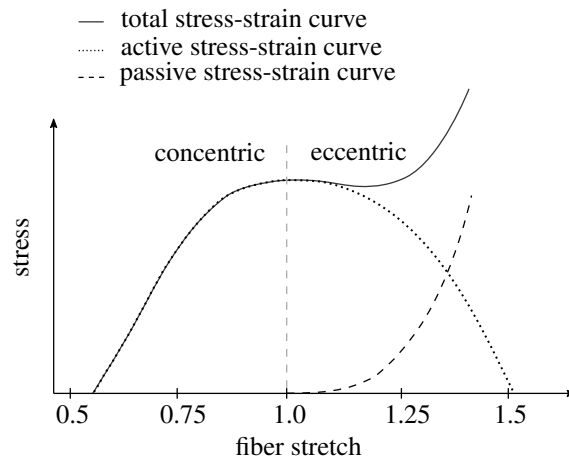


Figure 3.4: Stress-strain behavior of skeletal muscles. For concentric contraction (fiber stretch < 1.0), the active stress-strain curve dominates the total stress-strain relation. For an eccentric contraction (fiber stretch > 1.0), the superposition of the active and passive behavior determines the total stress-strain curve.

The mechanical properties of perimysium and epimysium have hardly been studied and their influence on muscle behavior is still poorly understood.

Perimysium is much thicker than endomysium and has a well-ordered structure [153] consisting of flat perimysial layers with two or more cross plies of wavy collagen fibers. At resting length the tensile stiffness of perimysium is low, but for large muscle stretches, the stiffness strongly increases [123]. The abruptly increasing stiffness at large sarcomere lengths prevents over-stretching of the muscles [165]. Perimysium behaves similar to endomysium because its originally wavy collagen fibers are stretched and aligned in muscle fiber direction at high extensions which results in increasing tensile stiffness. Due to its low stiffness over a large range of strains, perimysium can only bear large forces at high tensile deformations far beyond the range of working lengths in skeletal muscles [187].

Perimysium is viscoelastic [167]. The reorientation of the collagen fibers does not seem to be responsible for this, but rather the relaxation processes within the collagen fibers or at the interface between fibers and matrix.

Epimysium is the outermost layer of the skeletal muscle and surrounds the entire muscle for protection. Regarding the tensile properties, epimysium shows a similar nonlinear stress-strain behavior to endomysium and perimysium [68] due to the orientation of collagen fibers in loading direction [165, 166]. Experiments on the tibialis anterior muscle of rats show that the tensile stiffness of epimysium increases with age [68]. Furthermore, the mechanical properties of epimysium can be exploited in suturing of injured muscles and help the repaired tissue to bear higher forces [114].

3.4 Micromechanical model

Most existing models (e.g. [93, 152, 181]) focus on the overall behavior of skeletal muscle (level 5). In this work, we analyze the mechanical behavior at lower levels, in particular levels 3 and 4.

Due to large strains in fascicles, the continuum mechanical model is formulated based on the finite strain theory. The quasi-static balance of linear momentum

$$\mathbf{0} = \text{Div} \mathbf{S}, \quad (3.1)$$

is used because the forces generated in fascicles are much higher than inertia and body forces. $\mathbf{S} = \mathbf{F}^{-1} \cdot \mathbf{P}$ denotes the second Piola-Kirchhoff stress tensor, where \mathbf{F} is the deformation gradient and \mathbf{P} the first Piola-Kirchhoff stress tensor.

The fascicles (level 4) are modeled as a fiber-matrix composite. The muscle fibers are aligned parallel and surrounded by the connective tissue endomysium. Contrary to single-scale approaches [87, 227, 239], we capture the material properties for the components individually and introduce two material models which take into account the different mechanical behavior of muscle fibers and endomysium.

3.4.1 Muscle fiber (level 3)

The strain energy density function for muscle fibers Ψ_{fiber} is decomposed into a passive and an active part

$$\Psi_{\text{fiber}} = \Psi_{\text{fiber}_{\text{pas}}} + \Psi_{\text{fiber}_{\text{act}}}. \quad (3.2)$$

Similarly to a mechanical spring, muscle fibers provide passive resistance once the fiber is stretched (Fig. 3.3a). This is characterized by the passive part of the strain energy density function $\Psi_{\text{fiber}_{\text{pas}}}$. The active part $\Psi_{\text{fiber}_{\text{act}}}$ describes the ability of muscle fibers to generate force in fiber direction (Fig. 3.1) through electrical activation.

The split of the strain energy density function into a passive and an active part leads to a split of the second Piola-Kirchhoff stress tensor

$$\mathbf{S}_{\text{fiber}} = 2 \frac{\partial \Psi_{\text{fiber}_{\text{pas}}}}{\partial \mathbf{C}} + 2 \frac{\partial \Psi_{\text{fiber}_{\text{act}}}}{\partial \mathbf{C}} = \mathbf{S}_{\text{fiber}_{\text{pas}}} + \mathbf{S}_{\text{fiber}_{\text{act}}}, \quad (3.3)$$

where \mathbf{C} is the right Cauchy-Green tensor and $\mathbf{S}_{\text{fiber}_{\text{pas}}}$ and $\mathbf{S}_{\text{fiber}_{\text{act}}}$ are the passive and active components of the second Piola-Kirchhoff stress tensor, respectively.

3.4.1.1 Passive behavior

We use a decoupled representation of the passive strain energy density function $\Psi_{\text{fiber}_{\text{pas}}}$ and define a distortional $\hat{\Psi}_{\text{fiber}_{\text{pas}}}$ and a volumetric energy component $\Psi_{\text{vol}, \text{fiber}_{\text{pas}}}$. The influence of fiber anisotropy is negligible for our load cases and, therefore, for simplicity, an isotropic material

law is used. The distortional strain energy density function is represented by

$$\hat{\Psi}_{\text{fiber pas}} = \frac{1}{2} \mu_{\text{fiber}} [\text{tr} \hat{\mathbf{C}} - 3], \quad (3.4)$$

with the shear modulus μ_{fiber} and trace of the distortional part of the right Cauchy-Green tensor $\hat{\mathbf{C}} = J^{-2/3} \mathbf{C}$. The volumetric part of the strain energy density function $\Psi_{\text{vol, fiber pas}}$ reads

$$\Psi_{\text{vol, fiber pas}} = \frac{1}{2} \kappa_{\text{fiber}} [J - 1]^2, \quad (3.5)$$

where the Jacobian determinant $J = \det \mathbf{F}$ is the determinant of the deformation gradient \mathbf{F} and κ_{fiber} is the bulk modulus.

Thus, by making use of Eq. (3.3), the passive second Piola-Kirchhoff stress tensor $\mathbf{S}_{\text{fiber pas}}$ is

$$\mathbf{S}_{\text{fiber pas}} = \mu_{\text{fiber}} J^{-2/3} \left[\mathbf{I} - \frac{1}{3} \text{tr}(\mathbf{C}) \mathbf{C}^{-1} \right] + \kappa_{\text{fiber}} [J - 1] J \mathbf{C}^{-1}, \quad (3.6)$$

with the second order identity tensor \mathbf{I} .

3.4.1.2 Active behavior

The active behavior is modeled based on an active stress function

$$\frac{\partial \Psi_{\text{fiber act}}}{\partial \lambda_{\text{fiber}}} = P_{\text{act}} = \bar{\gamma}(t, f_s, \dot{l}_s) f(\lambda_{\text{fiber}}) P_{\text{max}}, \quad (3.7)$$

as introduced in [87], consisting of a normalized force-length relation f , the maximum isometric active stress in the muscle fibers P_{max} and a chemoelectrical function $\bar{\gamma}$ describing the activation of the muscle fiber during electrical stimulation (see also Sect. 3.4.1.2.2). Further, t denotes the time, f_s the stimulation frequency used to activate the muscle fiber and \dot{l}_s the contraction velocity of the sarcomere. In the Appendix, the inclusion of the stretch rate in the chemoelectrical function is shown (see Eqs. B.3a and B.3b) and the force-velocity relation obtained for different fiber lengths is plotted in Fig. B.3. \dot{l}_s can be determined from the change of fiber stretch $\lambda_{\text{fiber}} = \sqrt{\text{tr}(\mathbf{C} \cdot [\mathbf{a}_0 \otimes \mathbf{a}_0])}$ over time, where the unit vector \mathbf{a}_0 is the fiber direction in the reference configuration.

The active stress function P_{act} (Eq. (3.7)) enters the active component of the second Piola-Kirchhoff stress tensor [87]

$$\mathbf{S}_{\text{fiber act}} = \bar{\gamma}(t, f_s, \dot{l}_s) f(\lambda_{\text{fiber}}) \frac{1}{\lambda_{\text{fiber}}} P_{\text{max}} \mathbf{a}_0 \otimes \mathbf{a}_0. \quad (3.8)$$

3.4.1.2.1 Sarcomere force-length-relationship

A mean sarcomere length-force relationship obtained for rat extensor digitorum longus and gastrocnemius medialis muscle fiber bundles [240] is used for the force-length relation f :

$$f(\lambda_{\text{fiber}}) = \max\left(0.0015 \left[\frac{\lambda_{\text{fiber}} l_{s0}}{l_{\text{norm}}}\right]^4 + 0.018 \left[\frac{\lambda_{\text{fiber}} l_{s0}}{l_{\text{norm}}}\right]^3 - 0.935 \left[\frac{\lambda_{\text{fiber}} l_{s0}}{l_{\text{norm}}}\right]^2 + 4.078 \frac{\lambda_{\text{fiber}} l_{s0}}{l_{\text{norm}}} - 3.715; 0\right) \quad (3.9)$$

with $l_{\text{norm}} = 1.0 \mu\text{m}$ used to normalize the function. l_{s0} is the resting length of sarcomeres. The current sarcomere length l_s is calculated via $l_s = \lambda_{\text{fiber}} l_{s0}$.

3.4.1.2.2 Chemoelectrical processes on cellular level

The contraction mechanism in skeletal muscles involves strongly coupled electrical, chemical and mechanical processes. The central nervous system emits electrical impulses to motor neurons which transmit them centrally to the muscle fibers. The electrical impulses propagate along the muscle fibers.

The activation of muscle fibers is described by the chemoelectrical function $\bar{\gamma}(t, f_s, \dot{l}_s)$ taking values between 0 and 1. The one-dimensional but highly detailed model by Heidlauf et al. [88] describes the processes by about 60 differential equations. We extend Heidlauf's approach to a three-dimensional setting. Details on the 3d extension of the chemoelectrical function $\bar{\gamma}(t, f_s, \dot{l}_s)$ are found in the Appendix.

3.4.2 Connective tissue endomysium

The strongly nonlinear passive stress-strain behavior of the connective tissue endomysium (see Fig. 3.3) can be described by the isotropic hyperelastic first order Ogden model. For our load cases we can neglect the influence of the anisotropy of endomysium due to the collagen fibers. Thus, for simplicity, isotropic material behavior is assumed. As a result no precise information can be obtained regarding the mechanical properties transverse to the muscle fiber or the collagen fiber direction.

The strain energy density function Ψ_{endo} is additively split into a distortional part $\hat{\Psi}_{\text{endo}}$ and a volumetric part U_{endo} :

$$\Psi_{\text{endo}} = \hat{\Psi}_{\text{endo}} + U_{\text{endo}} \quad (3.10)$$

$$= \frac{2\mu_{\text{endo}}}{\alpha_1^2} \left[\hat{\lambda}_1^{\alpha_1} + \hat{\lambda}_2^{\alpha_1} + \hat{\lambda}_3^{\alpha_1} - 3 \right] + \frac{1}{2} \kappa_{\text{endo}} [J - 1]^2 \quad (3.11)$$

with the shear modulus μ_{endo} , the bulk modulus κ_{endo} and the constant α_1 . $\hat{\lambda}_i = J^{-1/3} \lambda_i$ are the distortional parts of the principal stretches λ_i .

From the strain energy density function Ψ_{endo} , the second Piola-Kirchhoff stress tensor is calculated:

$$\mathbf{S}_{\text{endo}} = 2 \frac{\partial \Psi_{\text{endo}}}{\partial \mathbf{C}} \quad (3.12)$$

$$= \frac{2\mu_{\text{endo}} J^{-1/3\alpha_1}}{\alpha_1} \sum_{i=1}^3 \lambda_i^{\alpha_1} \left[\lambda_i^{-2} \mathbf{e}_i \otimes \mathbf{e}_i - \frac{1}{3} \mathbf{C}^{-1} \right] + \kappa_{\text{endo}} [J - 1] J \mathbf{C}^{-1}. \quad (3.13)$$

In this work we neglect the passive stresses of endomysium and muscle fiber during compression. In [22], small passive stresses in compression tests are identified, but only for the entire fascicle. A clear identification of the passive stresses in the components is missing.

3.4.3 Material Data

Muscle fiber

The shear modulus μ_{fiber} and the bulk modulus κ_{fiber} of the muscle fiber are determined based on the experimentally determined Young's modulus $E_{\text{fiber}} = 0.0465 \text{ N/mm}^2$ for the EDL muscle fibers of mice [110] and a Poisson's ratio $\nu_{\text{fiber}} = 0.4999$ assuming muscle fibers to be nearly incompressible. Thus, we obtain $\mu_{\text{fiber}} = 0.016 \text{ N/mm}^2$ and $\kappa_{\text{fiber}} = 77.5 \text{ N/mm}^2$. The resting length of sarcomeres is set to $l_{s_0} = 2.0 \text{ }\mu\text{m}$.

We calculate the maximum isometric active stress in muscle fibers by dividing the experimentally determined median of the maximum muscle fiber forces by the median of the cross sectional area of the tested muscle fibers. For the latter two properties, several values are found in the literature. However, some of these were measured on mutant mice. We use data for wild-type mice [189] to obtain $P_{\text{max}} = 0.107 \text{ N/mm}^2$.

Connective tissue endomysium

The Young's modulus of endomysium $E_{\text{endo}} = 0.2415 \text{ N/mm}^2$ is determined by

$$E_{\text{endo}} = \frac{E_{\text{fascicle}} - E_{\text{fiber}}[1 - \varphi_{\text{endo}}]}{\varphi_{\text{endo}}} \quad (3.14)$$

with the volume fraction of endomysium $\varphi_{\text{endo}} = 0.1$ (see Sect. 3.5) and a Young's modulus of fascicle $E_{\text{fascicle}} = 0.066 \text{ N/mm}^2$ [85]. Assuming nearly incompressible behavior of endomysium with a Poisson's ratio of $\nu_{\text{endo}} = 0.4999$, the shear modulus $\mu_{\text{endo}} = 0.08 \text{ N/mm}^2$ and the bulk modulus $\kappa_{\text{endo}} = 402.5 \text{ N/mm}^2$ are obtained. The constant of the Ogden model $\alpha_1 = 7.95$ was determined based on a parameter fitting simulation with validation against experimental data [138], see also Fig. 3.7.

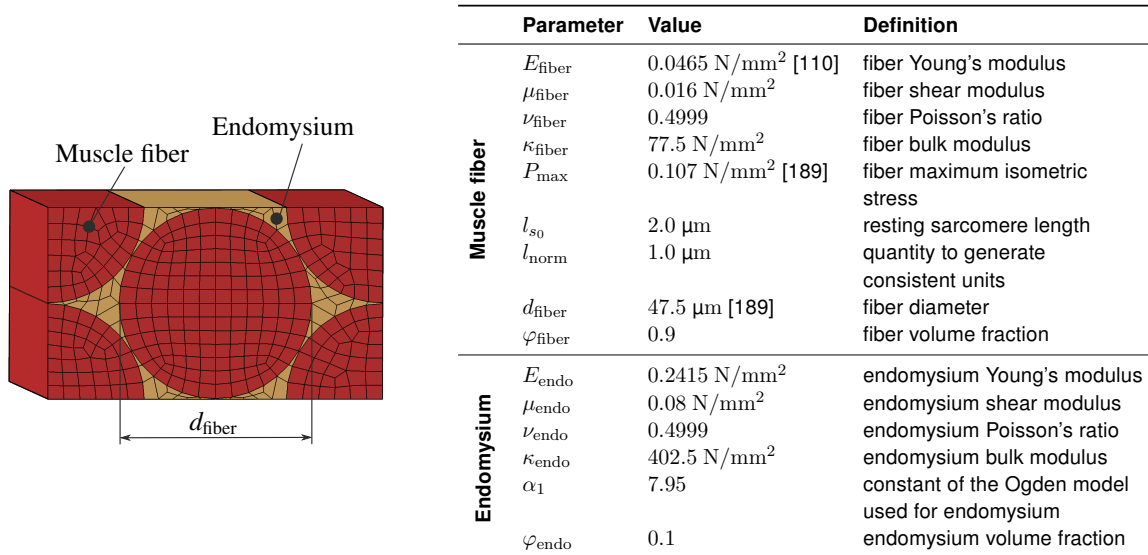


Figure 3.5: Material and geometrical data of the fascicle RVE. Left: Finite element model. Linear fully integrated hexahedral elements are used. The cross-section consists of 366 elements. The length of the RVE and the number of elements along the fiber direction were adjusted in simulations based on the problem studied to reduce computational cost. Right: Table of the material and geometry parameters used.

3.5 3D Computational Model of Fascicle

We generate a three-dimensional microstructure of a fascicle (hierarchy level 4) as a composite of idealized cylindrical parallel aligned muscle fibers and the surrounding connective tissue endomysium. To reduce the computational cost and to be able to conduct homogenization we assume periodically arranged muscle fibers and treat the volume element shown in Fig. 3.5 as a representative volume element (RVE) [10]. Compared to the RVE structure with hexagonal muscle fibers used in [202], the circular fibers avoid artificial stress peaks that may arise at corners and edges. Furthermore, our RVE includes variable endomysium thicknesses between the fibers which agrees with the natural variability of the tissue.

In general, any type of skeletal muscle from various species could be modelled with the proposed model. As the EDL of mice and rats has been studied in various experiments, see e.g. [110, 138, 179, 189], we model the EDL muscle of mice in the numerical simulation. The fiber diameter is $d_{\text{fiber}} = 47.5 \mu\text{m}$ taken from the median of the measured diameters of EDL muscle fibers of wild-type mice [189] and the volume fraction of muscle fibers is 90 %². All material and geometrical data used in our model is summarized in the table of Fig. 3.5.

The length of the RVE depends on the simulation. If the results are constant along the fiber direction due to constant electrical activation, a small RVE depth is selected to reduce the computational time. If the electrical activation varies temporally and spatially in fiber direction, a long RVE is used. The two components, muscle fiber and endomysium, are perfectly bonded by

²Only little data is available for volume fractions, none with respect to the chosen muscle at levels 3 and 4. In general, fiber volume fractions of 95 % \pm 8.8 % have been determined for the entire muscle [129].

sharing nodes at the interface. Consistent with the reduced examination of the fascicle geometry by using representative volume elements, periodic boundary conditions are applied.

3.6 Results and Discussion

We investigate the mechanical properties at different hierarchical levels of the EDL muscle (Fig. 3.6). Using a multiscale approach, level 4 (fascicle) as well as the behavior of its components, i.e., the muscle fiber (level 3) and the connective tissue endomysium are studied in different loading and activation scenarios.

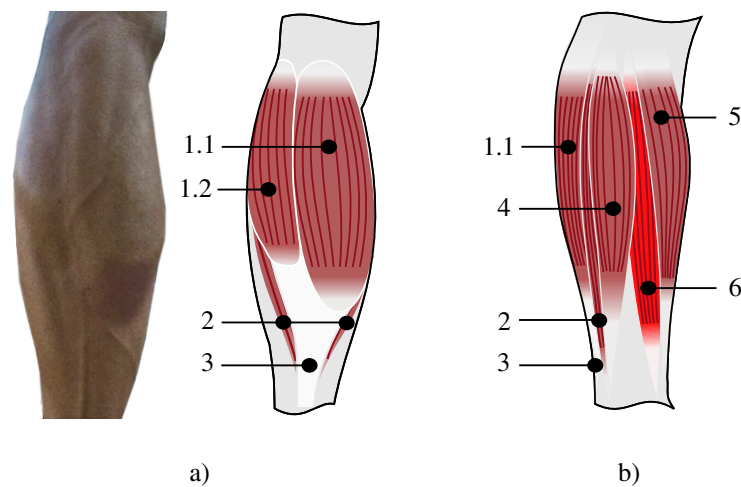


Figure 3.6: Representations of the human lower leg musculature. a) Frontal view of the human calf musculature and illustration of the individual muscles. b) Illustration of the side view of the lower leg musculature with highlighted extensor digitorum longus muscle, which is modeled in this contribution. 1.1: Musculus gastrocnemius Caput laterale, 1.2: Musculus gastrocnemius Caput mediale, 2: Musculus soleus, 3: Tendo calcaneus, 4: Musculus fibularis longus, 5: Musculus tibialis, 6: Musculus extensor digitorum longus.

Fascicles loaded in fiber direction are modelled to determine the force and stress development in the structure for fully activated muscle fibers, in which we consider the degree of activation to be constant along the fiber. The temporal evolution of the degree of activation and the spatial propagation of the activation potential in muscle fibers are modelled to examine local stresses along the fiber direction.

Further, we investigate the mechanical properties in a real loading case for an EDL fascicle where the fascicle is exposed to tensile and shear forces. In this case, the alignment of the muscle fibers (i.e., the pennation angle) plays an important role in the resulting lifting forces and lifting heights. Different pennation angles are considered and the effects on lifting forces and lifting heights are examined and compared. Finally, local stresses and strains in the muscle fiber and endomysium for different fiber strains are discussed.

3.6.1 Mechanical behavior of fascicles, muscle fibers and endomysium: Loading in fiber direction

3.6.1.1 Passive and active stress-strain responses of fascicles (level 4), muscle fibers (level 3) and the connective tissue endomysium

First, we examine the passive behavior of the fascicle as well as that of muscle fibers and endomysium. For this purpose, we set $\bar{\gamma} = 0$ for the activation parameter to artificially eliminate the active stresses in muscle fibers.

A uniaxial tensile test up to 100 % strain is performed in fiber direction. The passive stress-strain curve of the fascicle resulting from a parameter fitting simulation is in good agreement with the experimental results [138] (see Fig. 3.7).

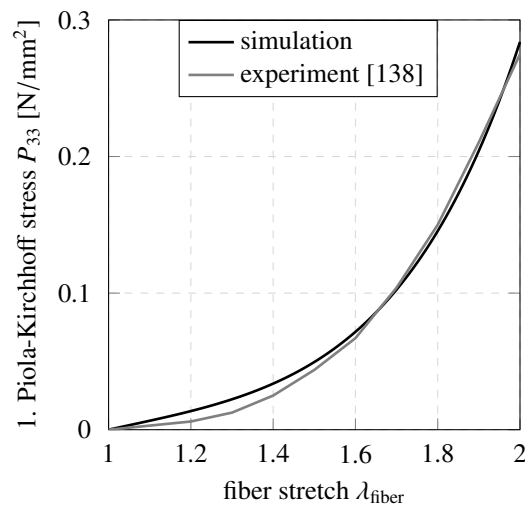


Figure 3.7: Passive behavior of fascicle stretched in fiber direction; 1. Piola-Kirchhoff stress vs. strain. The passive stress is zero at the resting length of the sarcomere and increases with increasing strain. The simulations are in good agreement with experimental results [138].

For fully electrically activated muscle fibers (i.e., $\bar{\gamma} = 1.0$ in Eq. (3.8)), the stress–fiber stretch response for uniaxial tension as well as compression is depicted for the fascicle (level 4), the muscle fiber (level 3) and the connective tissue endomysium in Fig. 3.8a³. The fascicle stresses are the averaged stresses of the RVE resulting from the fiber and endomysium stresses. All sarcomeres have an initial length corresponding to the resting length $l_{s0} = 2.0 \mu\text{m}$. The stresses in compressed fascicles ($\lambda_{\text{fiber}} < 1.0$) are solely generated within the activated muscle fibers because passive forces in the compressed endomysium and the compressed muscle fiber are neglected. Thus, stresses in endomysium occur only during tension ($\lambda_{\text{fiber}} > 1.0$), with a mild increase for small tensile strains and a drastic increase for strains larger than 50 %. At 30 % tensile strain, a switch in the load transfer behavior within the fascicle is clearly visible. The

³In the case of fully activated muscle fibers, the generated stress is maximal. Different stages of activation (i.e., $0 < \bar{\gamma} \leq 1$) are presented in the Appendix (Fig. B.1).

fiber carries the load for $0.635 \leq \lambda_{\text{fiber}} < 1.3$ and, thus, mainly in the physiological range of motion of EDL muscles which ends at approximately $\lambda_{\text{fiber}} = 1.35$ [5]. After the intersection point $\lambda_{\text{fiber}} \approx 1.3$, the passive stresses in endomysium dominate the fascicle's stress response.

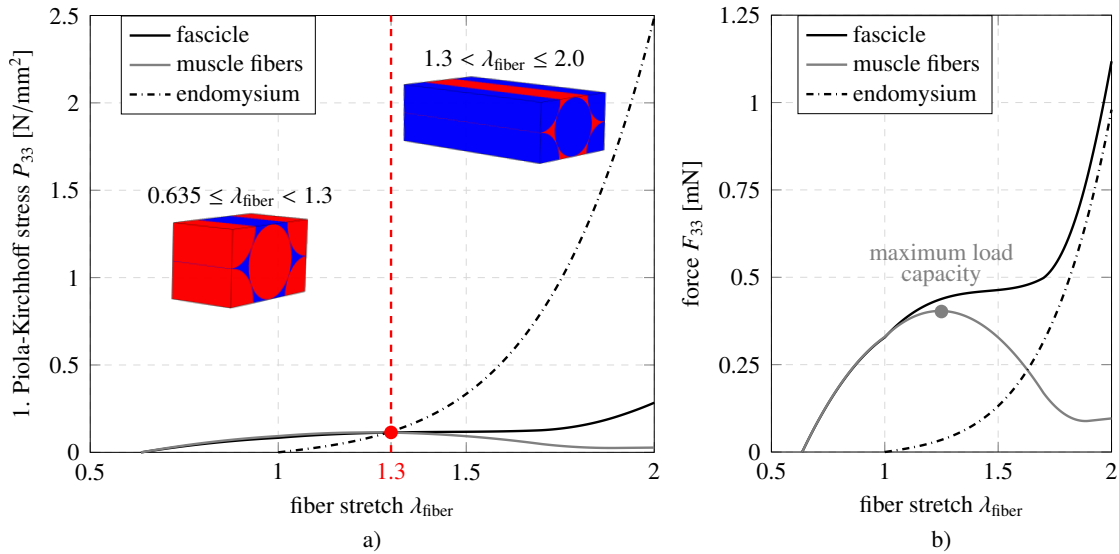


Figure 3.8: a) Stress–fiber stretch relationship for muscle fibers (level 3), endomysium and fascicles (level 4) in a fully electrically activated state ($\bar{\gamma} = 1$) demonstrating the strongly increasing stresses in endomysium during stretching. For $\lambda_{\text{fiber}} < 1.3$, the stresses in muscle fibers are higher compared to the ones in endomysium. At $\lambda_{\text{fiber}} \approx 1.3$, the 1. Piola-Kirchhoff stress–fiber stretch curves of muscle fibers and endomysium intersect. When stretched further, the passive stresses in endomysium dominate the fascicle's response. The inset graphics show that the phase carrying the maximum stress changes at this point (red: maximum stress, blue: minimum stress). b) The corresponding force–fiber stretch relationships. The maximum load capacity of the muscle fiber occurs at a fiber stretch of about $\lambda_{\text{fiber}} \approx 1.25$. At this stretch level, the force in the fascicle is higher than in the fiber due to the contribution of the endomysium.

The strongly nonlinear behavior of endomysium and the decreasing stress–fiber stretch curve of muscle fibers for higher strains show that for large strains endomysium provides the most important contribution to strain resistance (Fig. 3.8). The endomysium carries the majority of the load, resulting in stress concentrations that are almost 10 times higher than the averaged stress in the fascicle. Due to the passive forces in fibers during stretching, the overall stress is non-zero at fiber lengths where they can no longer be activated, i.e., for sarcomere lengths $l_s \geq 3.6 \mu\text{m}$ (compare Fig. 3.1). This is visible in the slight increase of the muscle fiber stress for fiber stretches $\lambda_{\text{fiber}} > 1.78$.

In Fig. 3.8b, the variation of force with fiber stretch is plotted for muscle fibers (level 3) and endomysium, as well as for the fascicle (level 4). The fascicle force here is the force within the RVE only and, thus, a fraction of the force generated in an entire fascicle. Fig. 3.8b gives insight into the interaction of muscle fiber and connective tissue in generating the fascicle force. The maximum force generated by the muscle fibers, i.e., the maximum load capacity, in the RVE is $F_{33} \approx 0.4 \text{ mN}$ and is mainly determined by the active force. Each muscle fiber in the fascicle generates about $F_{33} \approx 0.2 \text{ mN}$, which agrees well with the muscle fiber force measured in the EDL of mice, which ranges from 0.14 mN to 0.25 mN [179]. At this stretch level, the passive

force in endomysium already contributes markedly to the fascicle force.

The stress-strain curve for fascicles obtained here is qualitatively similar to the stress-strain behavior of an entire muscle with the same fiber volume fraction in [202]. On the fascicle level, however, larger strains are required before exponential increase in stresses occurs. This difference is due to the stronger nonlinearity of the connective tissue in the entire muscle, which is composed of endomysium, epimysium and perimysium. In contrast, on the fascicle level considered here, only endomysium is present.

3.6.1.2 Local stresses in fibers and endomysium due to temporal change of activation degree and propagation of the activation impulse along the muscle fiber

In reality, complete activation ($\bar{\gamma} = 1$) is not achieved at the beginning of the innervation of the muscle fibers, but shortly afterwards. Thus, both the evolution of the degree of activation over time and the propagation of the activation impulse along the muscle fiber affect the fascicle's mechanical behavior. The contractile response due to electrochemical processes is studied by varying $\bar{\gamma}$ with time and position along the fiber (see Appendix for the set of equations). The electrical impulses, so called action potentials, are applied in the middle of the muscle fiber with a frequency of 100 Hz and propagate to the ends of the fiber. Due to the high emission rate of 100 Hz, the twitches overlap and the muscle fiber force increases continuously. This phenomenon is called tetanic contraction [41].

We assume all muscle fibers to be innervated by the same motor neuron so that all fibers are activated simultaneously. Our model captures both, fast and slow twitch muscle fibers. As the EDL muscle consists almost exclusively of fast twitch fibers, these are modelled here (see Appendix for details).

To consider the activation process, a passive pre-stretch is exerted before an isometric contraction⁴ is applied. This corresponds to the daily life situation of keeping a slightly pressed gas pedal in a car at a fixed position. In this scenario, the EDL is tensed at a constant length in a stretched position.

In the following simulations, the fascicle is pre-stretched to $\lambda = 1.25$ so that the fibers can generate the maximum force (compare Fig. 3.8b). Afterwards it is kept at this length by fixing the surfaces in z -direction (periodic boundary conditions are maintained in x - and y -direction) and, subsequently, the muscle fibers are electrically activated.

Figure 3.9a shows the stress evolution over an activation cycle. The stresses propagate due to the wave-like propagation of the membrane potential V_m . As the electrical impulse is initiated in the middle of the muscle fiber, the stresses initially increase strongly in the middle and propagate outwards. The frequency of the applied electrical impulses is 100 Hz, so that new impulses are generated every 10 ms. The mechanical reaction to the electrical impulse is delayed by about 2 ms (Fig. B.2). Further information on the development of the membrane potential V_m due to

⁴In isometric contraction, the activated muscle is held at a constant length.

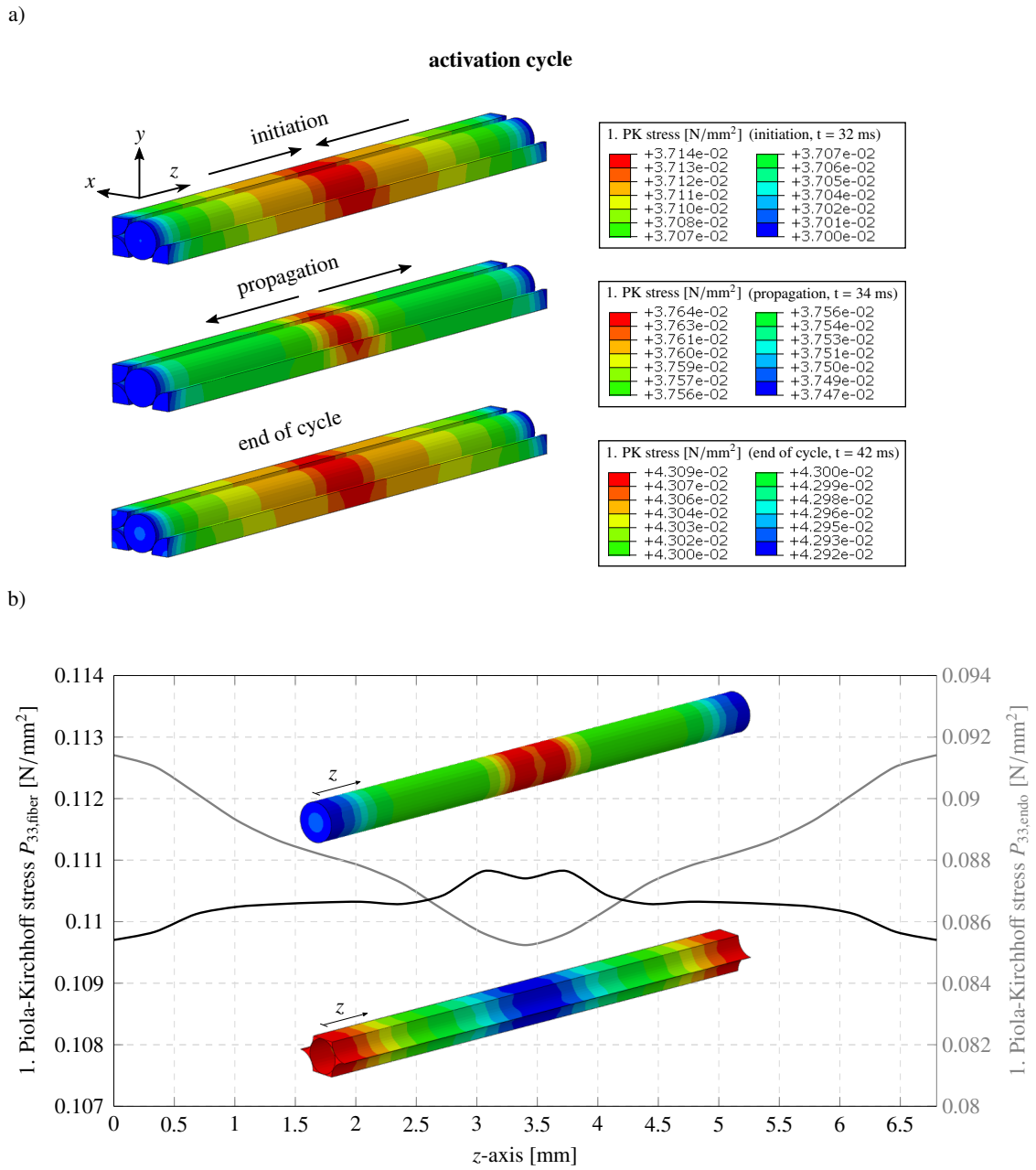


Figure 3.9: The influence of chemoelectrical processes in electrically activated fascicles and the associated temporal and spatial changes in the activation level of muscle fibers on the stress development in both components. a) Stress distributions for one cycle of electrically activated muscle fibers in the fascicle. The action potential initiated in the middle of the muscle fiber propagates along the muscle fiber which is reflected in the propagation of stresses. b) 1. Piola-Kirchhoff stress in the muscle fiber and the connective tissue endomysium at activation time $t = 250$ ms. Tetanic stimulation for a EDL fascicle pre-stretched with $\lambda_{\text{fiber}} = 1.25$ from the resting length of mouse EDL muscle fibers of 0.544 cm [26] to a length of 0.68 cm. Stresses for muscle fiber and endomysium are evaluated in fiber direction and exhibit inverse behavior.

the electrical impulses and the resulting delayed increase of the activation parameter $\bar{\gamma}$ which describes the coupling of the electrochemical processes and the mechanical processes are given in the Appendix.

To compare the influence of the electrical stimulation on the stress development in the muscle fiber and the connective tissue endomysium, their 1. Piola-Kirchhoff stresses are evaluated at activation time $t = 250$ ms (Fig. 3.9b) when the activation of fast twitch muscle fibers reaches its maximum (i.e., $\bar{\gamma} = 1$, Fig. B.2b). Initially, the stresses in the muscle fiber and the connective tissue endomysium are constant along z -direction due to passive pre-stretching. The activation of the muscle fiber results in a stress increase in the entire fiber that is maximal in the middle of the fiber and minimal at the ends of the fiber (Fig. 3.9b).

The stresses in the endomysium follow an inverse trend compared to those in the muscle fiber. The increased stresses in the middle of the fiber relieve the endomysium, so that the passive stresses in the endomysium decrease in the middle. Similarly, the reduced stresses in muscle fibers towards their ends cause the passive stresses in the endomysium to increase.

As seen in Fig. 3.9b, the local variation of stresses along the fiber direction is small in both components in the fully activated case. Therefore, we neglect these differences along the fiber in the following.

3.6.2 Mechanical behavior of fascicles and its components in unipennate muscles under real loading conditions

3.6.2.1 Influence of the pennation angle on fiber lifting forces and lifting heights

Muscles vary with respect to the external shape as well as the internal structure. In unipennate muscles such as the extensor digitorum longus, all muscle fibers are aligned parallel, at a certain (non-zero) angle to the tendon/line of action of the muscle.

In the following, we study the active force development in unipennate muscles and compare it to parallel muscles, which have muscle fibers oriented parallel to the tendon on the fascicle level. In Fig. 3.10, the EDL is depicted in the initial and a stretched position. The stretched position demonstrates that the fascicle is loaded by normal and shear forces and the muscle fibers reorient themselves more in tendon direction during stretching. Thus, the pennation angle α (i.e., the angle between fibers and the tendon) changes. Consequently, the unit vector \mathbf{a}_0 in Eq. (3.8) which is aligned in fiber direction has to be updated during the simulations.

First, we plot the force–fiber stretch curves of a parallel muscle and a unipennate EDL muscle with an initial pennation angle of about 10° [223]. We compare the fiber lifting force of both muscle types, which is the active force exerted by one fully activated muscle fiber and transferred in tendon direction. To determine the active lifting force, we run simulations for non-activated muscle fibers (only passive properties) and for fully activated fibers (passive and active properties). The active forces are the difference between these results.

Unipennate muscles have a larger physiological cross-section (i.e., the cross-section perpen-

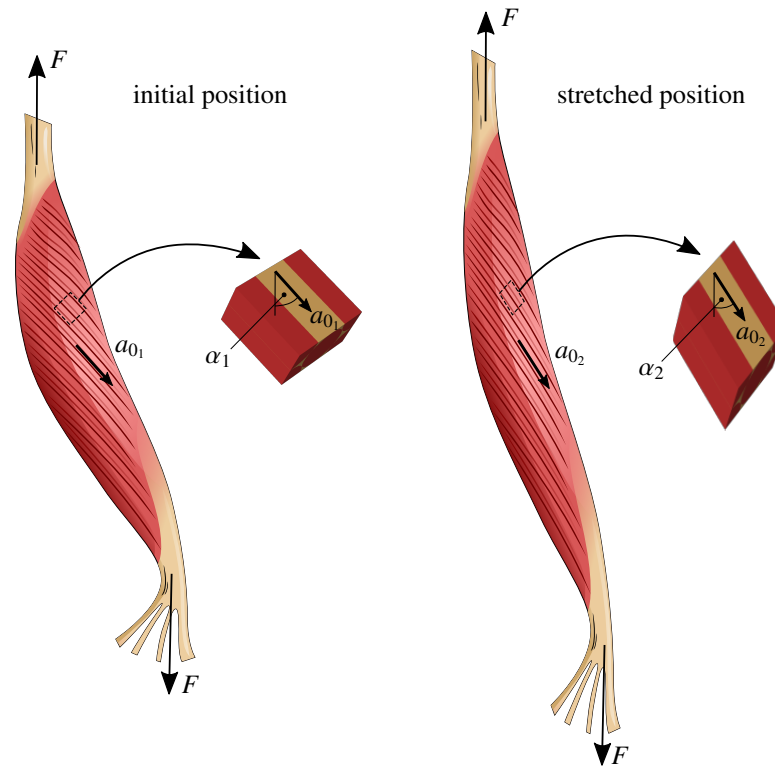


Figure 3.10: Extensor digitorum longus muscle: initial and stretched position. Stretching the muscle in tendon direction results in normal and shear forces in fascicles. Therefore, the muscle fiber direction changes during stretching such that the pennation angle reduces.

dicular to the aligned fibers) than parallel muscles. With the same fiber volume fraction in both muscle types, the absolute amount of fibers in the physiological cross-section is larger than in the anatomical cross-section, which is measured perpendicular to the longitudinal axis of the muscle. Therefore, the muscle can exert more force in direction of the fibers. However, due to the fact that the fibers in the unipennate muscle are not aligned in the direction of the tendon, the fiber force cannot be completely transferred to the tendon.

The interaction of these two effects results in an overall increase in lifting force in unipennate muscles with increasing fiber stretch as can be seen in Fig. 3.11 in which a realistic EDL fascicle is compared to a fictional EDL fascicle with muscle fibers which are aligned parallel to the tendon (parallel muscle). The fictional EDL fascicle has a smaller physiological cross-section which is equal to the anatomical cross-section in this case. The two curves confirm that unipennate muscles exert higher lifting forces than parallel muscles. The comparison of the cross-sections shows a constant increase in force over the entire stretching range for the physiological cross-section (inset graph in Fig. 3.11), see also Lieber et al. [127]. Further, it is evident that the advantage in lifting force 0° fibers have over 10° fibers becomes smaller with increased stretching (see inset graph in Fig. 3.11) because the pennation angle is reduced during stretching. In total, for small strains, the two effects balance each other out, however, with increasing strain,

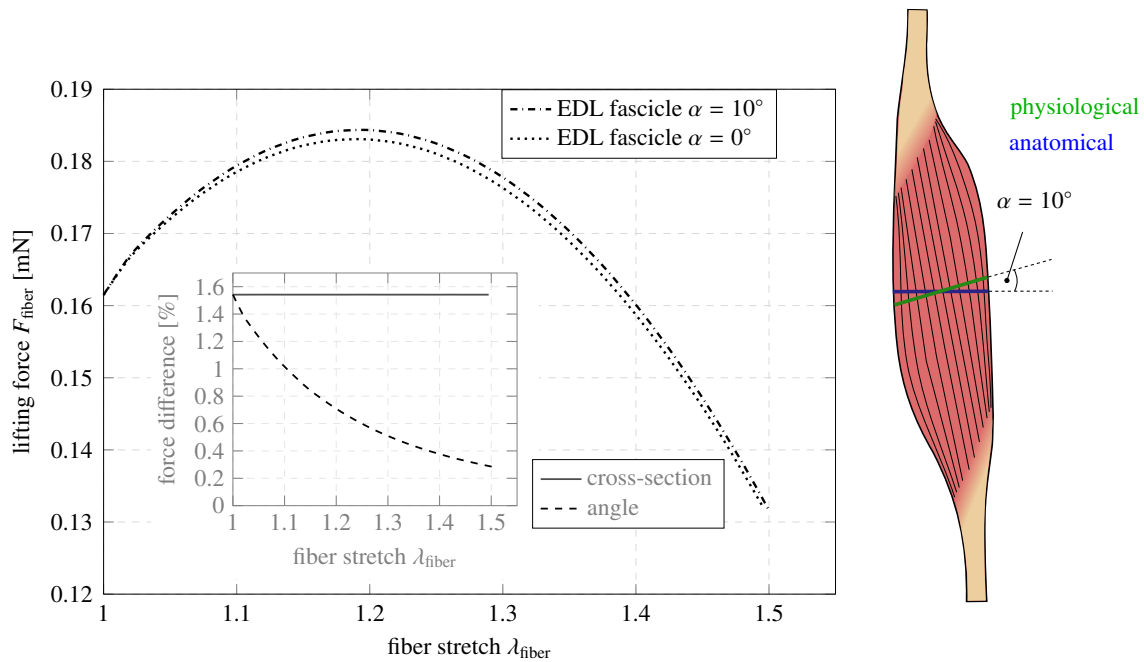


Figure 3.11: Fiber lifting force–fiber stretch curve for a real EDL fascicle with a pennation angle of $\alpha = 10^\circ$ compared to a fictional EDL fascicle with a pennation angle of $\alpha = 0^\circ$. Unipennate muscles exert higher lifting forces than parallel muscles. The larger physiological cross-section of the unipennate muscle results in an increase in lifting force that for low degrees of fiber stretch counterbalances the reduction of lifting force due to the pennation angle α as seen in the inset graph. With increased stretching, the fibers reorient themselves in the tendon direction resulting in an overall increase in lifting force compared to the parallel muscle. On the right-hand side, the physiological and anatomical cross-sections for EDL muscles are shown. The pennation angle of $\alpha = 10^\circ$ results in an enlarged physiological cross-section compared to the anatomical cross-section.

the influence of the larger physiological cross-section on the lifting force becomes dominant. Unipennate muscles can therefore exert higher lifting forces over the entire stretch range of the muscle fibers.

In Fig. 3.12, different pennation angles in unipennate muscles are compared. For upper and lower limb muscles, the pennation angle ranges from 0° to about 30° [66, 125, 128]. Therefore, we investigate unipennate muscles with $\alpha = 10^\circ$, $\alpha = 20^\circ$ and $\alpha = 30^\circ$. We use the same fascicle RVE with a pennation angle of 10° as before and adjust the physiological cross-section for unipennate muscles with $\alpha = 20^\circ$ and $\alpha = 30^\circ$.

In Figs. 3.12a and b, the lifting force of the different unipennate muscles is plotted over the corresponding fiber stretch and muscle strain: With increasing initial pennation angle, the lifting forces increase even more over the total range of fiber stretch.

The muscle strains in b) are the strains in tendon direction. For a muscle with a pennation angle of 10° , a muscle length of 1.2 cm for an EDL muscle of young mice can be determined from [26]. Here, the same muscle length is assumed for all three considered muscles and the fiber length in muscles with larger pennation angles is determined from geometrical considerations (compare Fig. 3.13).

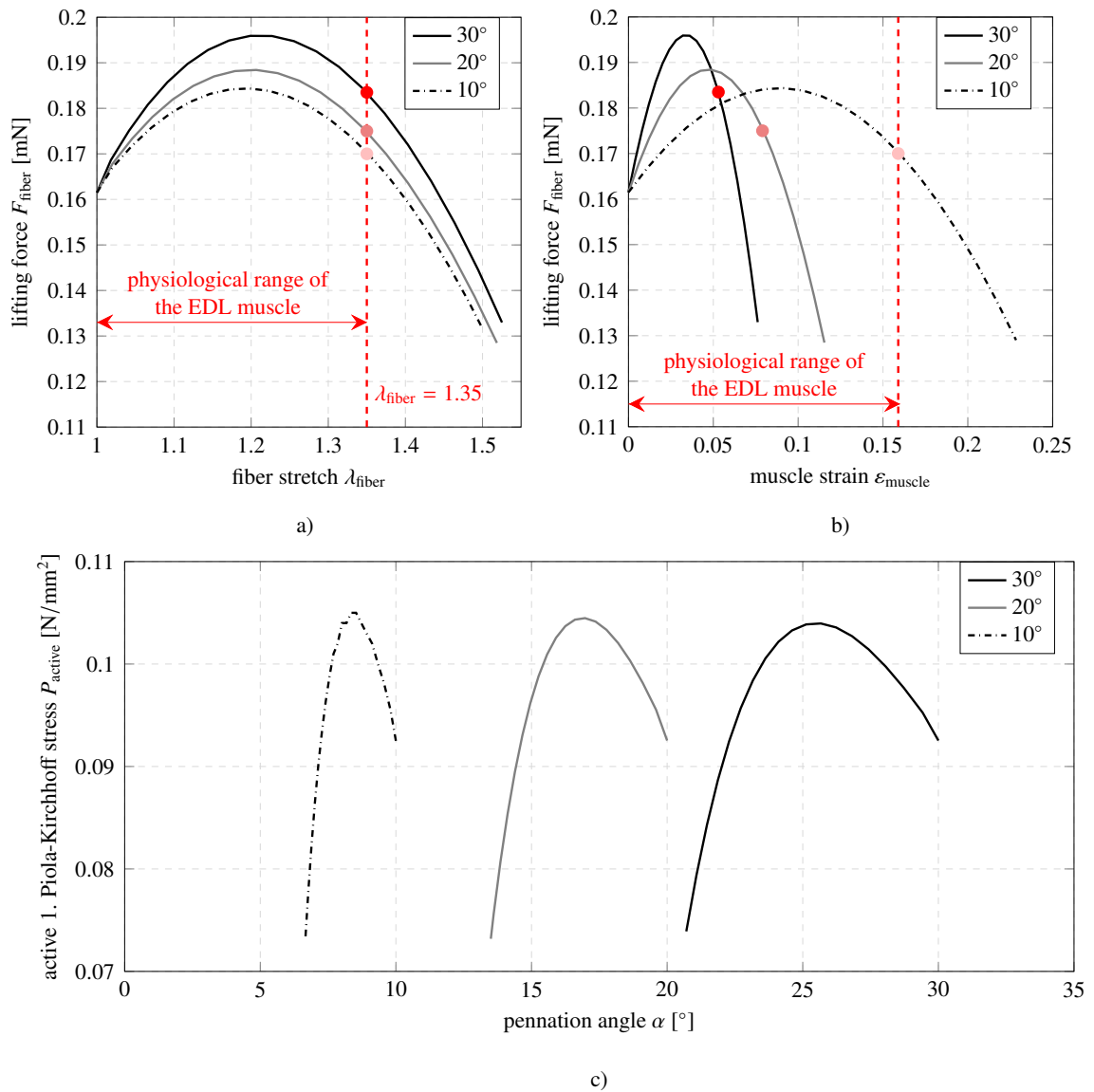


Figure 3.12: Influence of pennation angle α on lifting forces, stresses and strains in muscles. a) Fiber lifting force–fiber stretch curves. With increasing initial pennation angle, the lifting force of muscle fibers increases over the whole fiber stretch range. The physiological range that represents the stretch range of EDL muscle fibers ($\alpha = 10^\circ$) extends to $\lambda_{\text{fiber}} = 1.35$. b) Fiber lifting force plotted over the total EDL muscle strain. An increasing initial pennation angle leads to a strong reduction of EDL muscle strain. A fiber stretch of $\lambda_{\text{fiber}} = 1.35$ translates to a physiological stretch limit for EDL muscles of about $\varepsilon_{\text{muscle}} = 0.16$. In unipennate muscles with larger pennation angles, the achieved muscle strains for a fiber stretch of $\lambda_{\text{fiber}} = 1.35$ (marked with colored dots) are significantly lower. c) Active 1. Piola-Kirchhoff stress in a muscle fiber vs. updated pennation angle during simulation; fiber stretch $\lambda_{\text{fiber}} \approx 1.5$. The active stresses in muscle fibers remain the same for different unipennate muscles because the higher lifting forces in unipennate muscles with larger pennation angles result from larger physiological cross-sections. Furthermore, in these muscles the pennation angle is reduced more for the same fiber stretch due to increased shear forces.

The graphs in Fig. 3.12b indicate that muscle strain decreases strongly with increased initial pennation angle for the same fiber stretch. The physiological range of the total EDL muscle strain shown results from the muscle fiber stretch of $\lambda_{\text{fiber}} = 1.35$ (see a)). The muscle strains for $\alpha = 20^\circ$ and $\alpha = 30^\circ$ unipennate muscles are drastically reduced for a fiber stretch of $\lambda_{\text{fiber}} = 1.35$.

The active 1. Piola-Kirchhoff stress in fibers is plotted in Fig. 3.12c over the pennation angle for the three muscles with the same fiber stretch. The parabolic curves widen as the initial pennation angle of the muscles increases.

The general increase in lifting forces at larger pennation angles (see Figs. 3.12a and b) is due to the larger physiological cross-sections. The reorientation of muscle fibers in tendon direction is faster for larger pennation angles (Fig. 3.12c) due to higher shear forces which results in an increase in lifting forces with increasing fiber stretch. However, the active stresses in muscle fibers remain the same for different unipennate muscles as the active forces result from their physiological cross-sections (see c)).

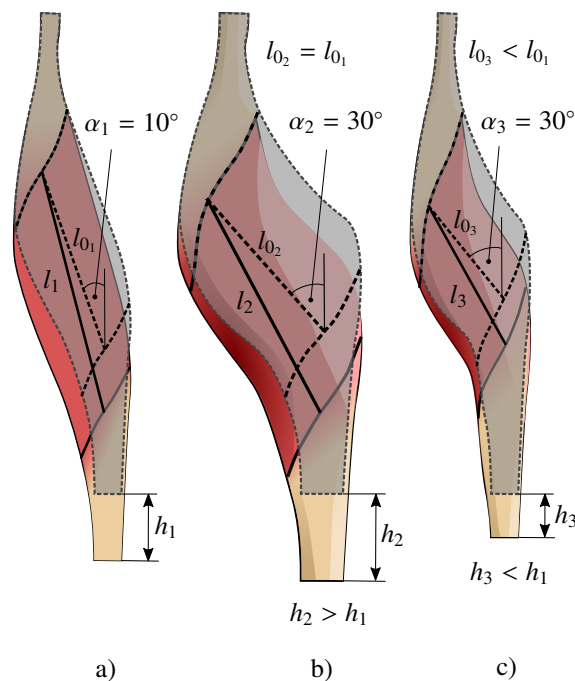


Figure 3.13: Lifting height for unipennate muscles with different initial muscle fiber lengths and pennation angles. The muscles are stretched in tendon direction. The pennation angle reduces and the initial muscle fiber lengths l_{01} , l_{02} and l_{03} increase to l_1 , l_2 and l_3 . The muscle fiber stretch is the same in all three muscles. a) A real EDL muscle with a pennation angle of 10° is stretched, resulting in lifting height h_1 . b) Stretching a fictional EDL muscle with a larger pennation angle of 30° and the same initial muscle fiber length results in increased lifting height h_2 . c) Fictional EDL muscle with the same muscle width as a) and the same pennation angle as b). The initial muscle fiber length is reduced. Although the pennation angle is larger than in a), the total lifting height h_3 is smaller because of the shorter muscle fibers.

Fig. 3.13 illustrates three unipennate muscles with shapes similar to the EDL muscle. Each muscle is shown in initial and stretched position in which all muscle fibers have the same fiber

stretch. In a real EDL muscle (a)), the given muscle fiber stretch results in a lifting height h_1 . The lifting height increases for unipennate muscles with larger pennation angle if the initial muscle fiber length is the same (Fig. 3.13b). In c), a fictional EDL muscle with the same muscle width as in a) but with shorter muscle fibers is shown. Despite the increased pennation angle, the lifting height h_3 is lower than h_1 . Therefore, muscle strains are significantly reduced for larger pennation angles in muscles of the same size as seen in Fig. 3.12b.

The physiological stretch limit of EDL muscles reaches approximately $\varepsilon_{\text{muscle}} = 0.16$ (Fig. 3.12b). Doubling the pennation angle from 10° to 20° leads to a small increase of 2.2 % in the maximum force, however, the lifting height for the same fiber stretch of $\lambda_{\text{fiber}} = 1.35$ is reduced by about 50 %. Compared to a muscle strain of 16.0 % for a 10° unipennate EDL muscle, a strain of only 7.9 % is reached with a pennation angle of 20° . If the initial pennation angle is increased further (e.g. to 30°), the impact is not as substantial. Despite the stronger increase in lifting force, the lifting height is reduced to a lesser extent. To achieve the same lifting height in unipennate muscles with larger pennation angles, the fiber stretch has to be much higher. Consequently, the active force becomes small or no more active force can be exerted (compare to Fig. 3.1).

Our FEM simulations confirm that unipennate muscles can exert higher lifting forces [79] at the cost of reduced lifting height [158, 209, 210, 232]. Pennate muscles with larger pennation angles are used as power muscles in the body, while pennate muscles with lower pennation angles or parallel muscles are located in body regions where large movements or fast movements are required [40].

Our results reveal that optimal functionality is provided by either very small pennation angles or very large pennation angles: If deformation is the main factor, the pennation angle must be small, as the lifting height strongly increases for small angle changes (Fig. 3.12b), but the lifting forces are reduced only slightly (Fig. 3.12a). For large lifting forces, however, pennation angles must be large, as the increase in force is significant (Fig. 3.12a) for even small angle changes while the lifting height is reduced to a lesser extent (Fig. 3.12b).

3.6.2.2 Local stresses and strains in fibers and endomysium for different fiber stretches

In this section, we analyze the local stresses and strains in the muscle fiber and the endomysium of the tensile- and shear-loaded EDL fascicle (pennation angle $\alpha = 10^\circ$). All muscle fibers are stimulated simultaneously and we assume fully activated fibers with $\bar{\gamma} = 1.0$ through the entire muscle fiber length. The results are summarized in Fig. 3.14.

The strain distributions in the fiber and the endomysium at the end of the deformation ($\lambda_{\text{fiber}} = 1.5$) (Fig. 3.14a) are depicted here as representative for the entire deformation process. For the muscle fiber, maximum strain values are located at the interfaces to the thinnest endomysium points and minimum strain values are close to where the endomysium is the thickest. The same applies to the endomysium: Maximum strains are found in the thin parts of the endomysium and minimum strains in the thick parts. For a better representation of the deformation along the fiber,

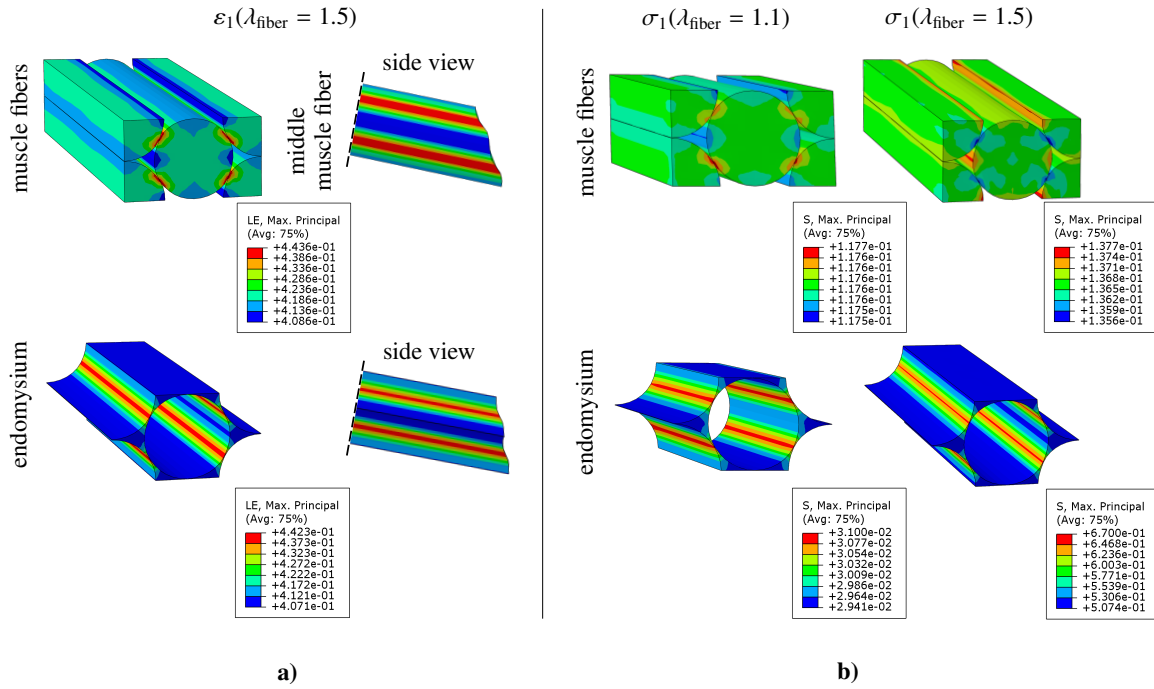


Figure 3.14: Local maximum principal stresses σ_1 and logarithmic strains ε_1 in muscle fiber and endomysium under a realistic loading case consisting of normal and shear forces. In the muscle fibers, the maximum and minimum stresses and strains arise at the interfaces. a) Local maximum principal logarithmic strains in fibers and endomysium; $\lambda_{\text{fiber}} = 1.5$. Over the complete strain range, the strains are maximal in the area of thin connective tissue and minimal in the area of thicker connective tissue. Additionally, the side views of the strain for the middle muscle fiber of the fascicle RVE and the endomysium at $\lambda_{\text{fiber}} = 1.5$ are shown which demonstrate the high shear strains existing in the areas of the maximum strains. b) Maximum principal stresses for both components at fiber stretches $\lambda_{\text{fiber}} = 1.1$ and $\lambda_{\text{fiber}} = 1.5$. For low strains, the stresses at the muscle fiber are maximal in regions where the endomysium is thinnest. In contrast, the stresses are minimal in regions where the endomysium is thickest. At large strains, this pattern is reversed. In the endomysium, the stresses and strains are maximal at the thinnest points over the entire strain range and minimal at the thickest points.

the side view is also shown for both components.

In Fig. 3.14b, the maximum principal stresses are depicted for the beginning of the deformation ($\lambda_{\text{fiber}} = 1.1$) and the end of the deformation ($\lambda_{\text{fiber}} = 1.5$). For the muscle fiber, the stresses are maximal in the area of the thinnest points and minimal at the thickest points of the endomysium for $\lambda_{\text{fiber}} = 1.1$. During the simulation, the points of maximum and minimum stresses at the muscle fiber switch positions, so in the end, maximum stress values are found at the interfaces to regions of thick connective tissue and minimum stresses at the interfaces to thin endomysium. The stress distribution in endomysium is similar to the strain distribution and maximum and minimum stresses are located at the same positions as for strains. The distribution remains the same for the entire deformation process.

In Fig. 3.14a, the side view shows the differently shaped ends of muscle fiber and endomysium, which is expected due to the shear force on the composite material. The maximum principal logarithmic strains are largest at the thinnest points of the endomysium, because the shear

strain is maximal at these points. The increased shear strains influence the muscle fiber edge, such that at the same areas the shear strains on the muscle fiber are maximal over the entire stretching process. Conversely, for the thickest parts of the endomysium, the shear strains are minimal and, thus, they are also minimal in the same area on the muscle fiber.

In Fig. 3.14b, the maximum stresses in the endomysium result from the maximum shear strains that occur at the same positions. In the same way, lower stress values are obtained due to lower shear strains. As the strain distribution in the endomysium remains the same for the entire deformation, the stress distribution does not change either. Up to about $\lambda_{\text{fiber}} = 1.3$, the stresses in the muscle fiber are higher than in the endomysium (see Fig. 3.8a). As the shear strains are maximal/minimal at the interface to the thin/thick connective tissue areas, the stresses are also maximal/minimal there. From $\lambda_{\text{fiber}} = 1.3$ there is a transition of maximum stresses from fiber to endomysium evident in Fig. 3.14b. This is also illustrated in Fig. 3.8. The stresses rapidly increase in the endomysium, most strongly in the thinnest regions. The muscle fiber is relieved at that point such that the stresses in the fiber follow an inverse trend: The previous maximum stresses in the fiber become the minimum stresses and vice versa.

The stress distribution in the muscle fiber shows that the sarcolemma, the cell membrane of the muscle fiber, is exposed to the highest stresses. The high shear stresses occurring at the sarcolemma due to the high shear strains are assumed to be responsible for the injury of the membrane [70]. Furthermore, the stress distribution in the endomysium shows that the thinnest areas are exposed to the maximum stresses due to the existing shear strains, thus, these areas are at high risk of being damaged.

3.7 Conclusion

In this work, we developed a continuum mechanical model for the chemo-electro-mechanical behavior of skeletal muscle fascicles. The model describes the fascicle as a two-phase composite consisting of muscle fibers and endomysium. The individual properties of each phase are modelled as well as their interaction.

We considered a real loading case of EDL fascicles and studied the influence of pennation, as well as the influence of the pennation angle of different unipennate muscles on the mechanical behavior. Our simulations are in good agreement with experimental results. We predict the increasing lifting force [79] of pennated muscles and the simultaneous reduction of the potential stretch range of the entire muscle [232], showing that muscle fibers with large pennation angles can only exert lifting forces in very small muscle strain ranges.

Additionally, our simulation results highlight that optimal arrangements of the microstructure are obtained with either very small or very large pennation angles. On the one hand, small angle changes at very small pennation angles can result in a significant increase in lifting height with a small reduction in lifting force. On the other hand, small angle changes at very large pennation angles can lead to a high increase in lifting force and a small reduction in lifting height.

The local strains and stresses for a real loading case of the EDL fascicle show that regions of

thin endomysium are at risk of damage, as they are exposed to large shear strains and therefore to the highest stresses. In the muscle fiber, the maximum strains and stresses are located at the edges resulting in risk of sarcolemma membrane damage during muscle contractions [156]. For a more detailed study of the high-risk locations for muscle damage, interface characteristics between muscle fiber and endomysium have to be considered. Generally, the model focuses on describing the behavior of fascicles in fiber direction, so precise information perpendicular to the fiber direction cannot be obtained.

Our model predicts that maximum strains occur in the same regions in muscle fibers and endomysium. However, this does not imply that the stresses are also maximal in these regions. Only at the beginning of the deformation process, the highest stresses are located at the same points as the highest strains in the fiber. Strains higher than the physiological range of motion result in a full reversal of the behavior, because the strongly increasing stresses in the endomysium relieve the fiber at these points.

4 | Article 3:

Computational modeling of damage in the hierarchical microstructure of skeletal muscles

4.1 Abstract

One of the skeletal muscle's exceptional properties is its high damage tolerance in terms of its high toughness, which allows the muscle to withstand cracks of millimeter length while maintaining most of its strength [207]. In skeletal muscles, damage occurs on different hierarchical levels of the microstructure. We analyze the damage behavior on hierarchy levels 3 (muscle fiber) and 4 (fascicle) on which the most common serious muscle injuries occur. Our model captures damage initiation and rupture of activated muscle fibers resulting from eccentric contractions. We consider the interaction between muscle fibers and endomysium and investigate the influence of the components titin and endomysium on the mechanical behavior in pre-damaged fascicles. Endomysium generally transmits contractile forces. Our results show that high strains in pre-damaged fiber regions are not transferred by the endomysium and, thus, adjacent undamaged fibers are well protected. Moreover, the results show titin's extraordinary stabilization properties of pre-damaged muscle fibers, so that macroscopic strains of fascicles are hardly reduced in case of strongly pre-damaged fibers and intact titin.

4.2 Introduction

Humans hardly suffer from any other sports injury as often as a muscle injury. In 23 soccer teams observed over a period of seven consecutive seasons, 35 % of all injuries affected the muscles [53]. Prevention and appropriate treatment of muscle injuries, thus, are important topics in sports research. This requires a detailed understanding of the mechanical properties of skeletal muscle, specifically in terms of damage initiation and total rupture of muscle fibers, fascicles or the entire muscle. Studying the damage behavior of muscles is not only a major topic in sports but also in biomimetics to produce equivalent synthetic counterparts of skeletal muscles [30, 212, 218, 225].

The most frequently occurring muscle injuries are indirect injuries which occur without any external force, i.e. they are the result of the muscle contraction itself. Direct muscle injuries, e.g. bruises, are caused by impacts or hits and account for less than 15 % of all muscle injuries [216].

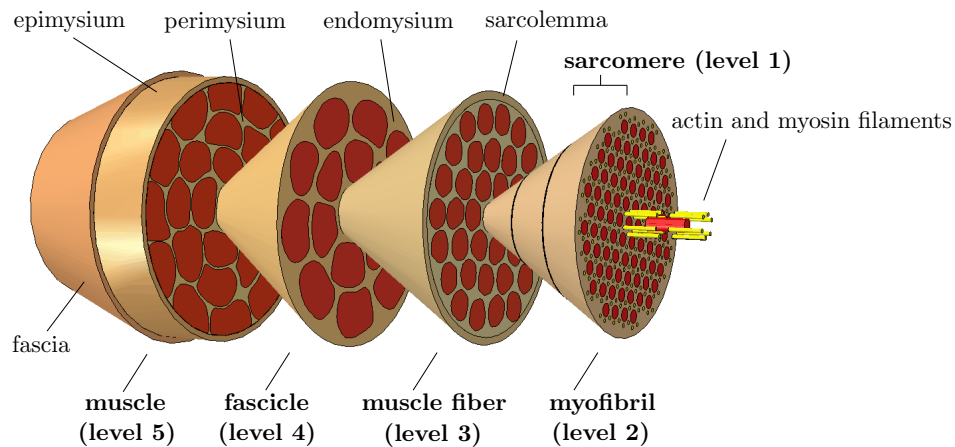


Figure 4.1: Hierarchical structure of skeletal muscle. Skeletal muscles (level 5) consist of 10-40 fascicles (level 4) surrounded by the connective tissues perimysium, epimysium and fascia. Each fascicle contains 10 until several hundred muscle fibers (level 3) which are embedded in the connective tissue endomysium. Myofibrils (level 2) have a diameter of ca. 1 μm and are covered by the cell membrane sarcolemma, forming the muscle fiber. Each myofibril consists of 1000 - 2 000 000 sarcomeres (level 1) which have a length of ca. 2.5 μm . The sarcomeres themselves consist of multiple protein filaments arranged in a highly organized array. The protein filaments are responsible for muscle movement.

We distinguish between the terms “damage” and “injury”: “Damage” to muscles refers to disruption of myofibrils [64, 136], whereas “injury” starts with a rupture of a whole muscle fiber [136, 146]. While muscle soreness is micro damage on the lowest hierarchical level (sarcomere), see Fig. 4.1, torn muscle fibers occur on the third (muscle fiber) and the fourth hierarchical level (fascicle) as they can involve rupture of multiple fibers. A torn fascicle (Fig. 4.2, MRI scan of the injured adductor longus muscle) occurs on hierarchy level 4 (fascicle) and a complete torn muscle on level 5 (muscle). The term muscle strain includes any type of damage and injury due to overstretching and can lead to both minor damage on the lowest level of the hierarchy and major injuries and ruptures at higher levels of the hierarchy.

Indirect muscle injuries are typically caused by eccentric overload, e.g. due to kicking, sprinting or a forceful slippage [3, 105, 150], while isometric or concentric muscle contractions seldom lead to muscle damages [4, 135, 145].

Experiments can only partly investigate the damage behavior of skeletal muscles on different hierarchy levels. On hierarchy level 3 (muscle fiber), the passive and active behaviors until rupture were investigated for non-activated muscle fibers [193, 230] as well as for activated fibers [36, 211]. Experiments also exist at higher levels [72, 116, 159, 186], however, they only provide limited insight into the interaction between components and the influence of individual components on the total damage behavior. Therefore, simulations are essential for a detailed understanding of the individual components and their interaction.

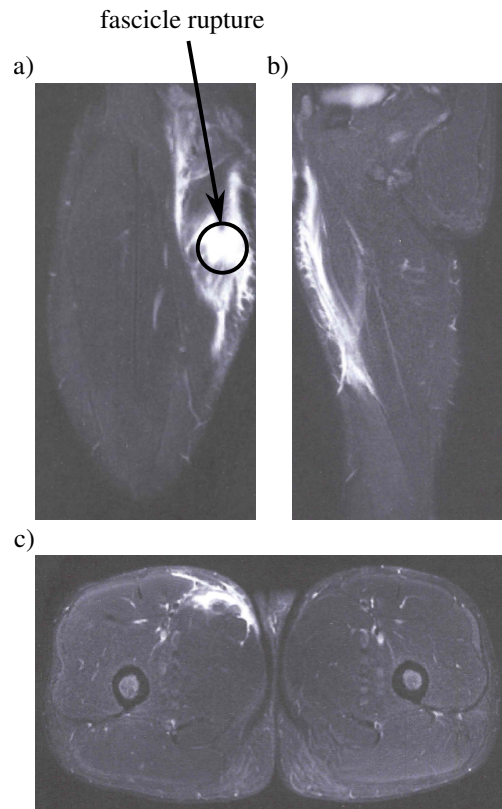


Figure 4.2: a) Front view, b) side view and c) bottom view of an MRI scan of an adductor longus fascicle rupture with accompanying edema and hemorrhage.

In the past, mechanical models investigated damage mechanics and injury susceptibility of the skeletal muscle on different hierarchical levels. For the entire skeletal muscle (hierarchy level 5), Ito et al. [103] formulated a constitutive model that considers anisotropic damage by using a second order damage tensor to represent the mechanical behavior at high strains and to predict the breaking points. Gao et al. [70] analyzed muscle damage during lengthening contraction on the third hierarchy level (muscle fiber), showing that muscles without dystrophin are more susceptible to damage. Some micromechanical finite element models [194, 219] examined damage and injury susceptibility on hierarchical level 4 (fascicle). Virgilio et al. [219] considered the effects of muscular dystrophy and shape variations of passive loaded fascicles on their mechanical properties and susceptibility to membrane damage. Sharafi et al. [194] studied the structure and the mechanics of the myotendinous junction on microscopic level by investigating its effect on local fiber strains to predict the likelihood of injury. Gao et al. [69] used a two-dimensional shear lag model on the fascicle level and analyzed the lateral force transmission between an injured and a healthy muscle fiber which protects the injured one from further damage. These mechanical models on hierarchical level 4 ignore damage evolution in fascicles which would provide information on the prevention of damage propagation in hierarchically structured skeletal muscles.

To this end, we introduce a 3D micromechanical continuum model for hierarchy level 4 (fas-

cicle) capable of modeling damage initiation and evolution until total muscle fiber rupture. We focus on indirect muscular injuries, specifically muscle strain, in the muscle belly and visualize the problem of eccentric motion in a simulation model. Our two-phase 3D fascicle RVE consisting of muscle fibers and endomysium allows to study the mechanical behavior of both components in a pre-damaged case more precisely than it is done in the 2D model in [69]. Since properties of lower hierarchical levels are taken into account, we can investigate the influence of the giant molecule titin in the muscle fiber on pre-damaged fascicles. For our model, we use the geometrical and material data of the extensor digitorum longus muscle (EDL), as this muscle is susceptible to muscle strain in its physiological range of motion [84].

4.3 Micromechanical damage model

The fascicles are modeled as a fiber-matrix composite with parallel oriented muscle fibers embedded in the connective tissue endomysium which captures the material properties of the components muscle fiber and endomysium separately. The elastic material models for the muscle fiber and the endomysium are introduced in our previous work [118]. These are extended here (see Sect. 4.3.1.1.3) to include titin's force enhancement in the elastic fiber material model as we focus on eccentric contractions.

The irreversible deformation of sarcomeres and the formation of microcracks are described by a Johnson-Cook model and a continuum mechanical damage model describes the collective failure of myofibrils until complete fiber rupture.

Several studies found that the strain is the major contributing factor to the failure of the muscle fiber [64, 73, 126]. In addition, it has been demonstrated that higher stresses at the same strains, e.g. when comparing passive loads, isometric and eccentric contractions of muscle fibers, result in greater damage [130]. Thus, in our model, damage evolution until total failure of fibers depends on stress and strain: The stress defines the initiation of microcracks (see Sect. 4.3.1.2); the strain determines the beginning of collective failure of myofibrils until complete fiber rupture (see Sect. 4.3.1.3).

Our model captures damaged muscle fibers, as they are disrupted first, whereas endomysium is damaged at higher strains [84], mainly in the case of an increased number of torn muscle fibers [56, 184]. Delamination between muscle fiber and endomysium normally occurs after tearing of the muscle fiber [230] and, thus, ensues from the rupture. Therefore, delamination as well as damage in endomysium is not considered.

4.3.1 Muscle fiber (level 3)

4.3.1.1 Muscle fiber: elastic behavior

Total stresses in muscle fibers can be split into a passive and an active part because the fiber exerts passive forces during stretching and generates active forces if the fiber is electrically acti-

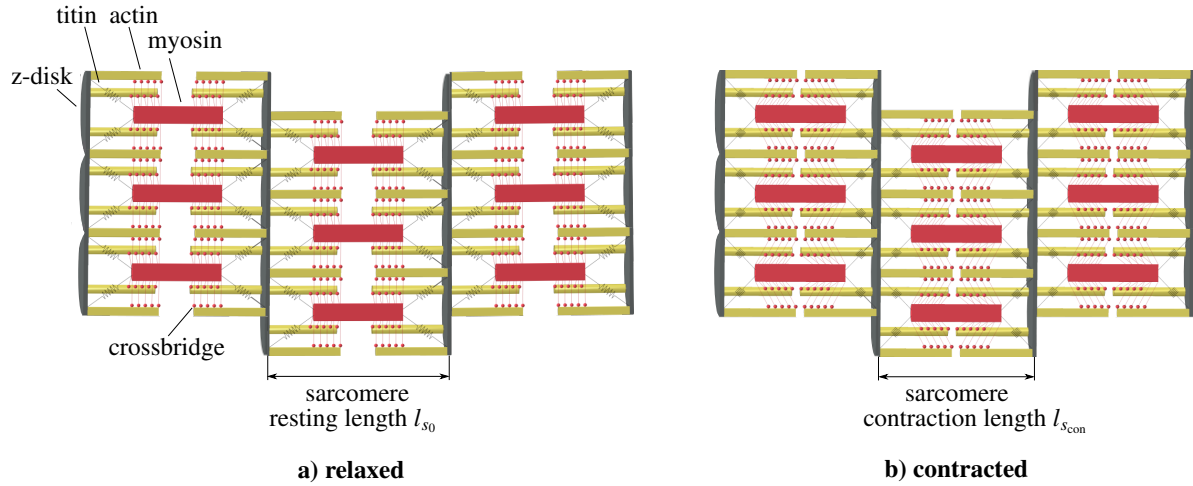


Figure 4.3: Detail of an array of sarcomeres in muscle fibers. The sarcomere is the smallest functional unit of the skeletal muscle and causes the active contraction. a) Relaxed state of the sarcomeres. Each sarcomere consists of a myosin protein that is surrounded by six actin proteins on each side (only four visible in sectional view). Actin and myosin are connected by the heads of the myosin molecules, forming cross-bridges. The actin filaments are connected with the z-disk which itself is connected to the myosin by the giant molecule titin. The distance between the z-disks determines the length of a sarcomere. b) Electrical activation of a muscle fiber causes a rotation of the crossbridges which pulls the actin filaments into the center when the muscle shortens [100].

vated. The active forces in muscle fibers are generated by small, aligned functional units, called sarcomeres, which shorten in a concentric contraction (see Fig. 4.3). In the case of an eccentric contraction, which means that the fiber is activated and then stretched, titin generates additional forces in the stretched sarcomeres. This so called force enhancement by titin increases the stresses. Therefore, we introduce an additional stress $\sigma_{\text{fiber_titin}}$ in the elastic material model of Lamsfuss and Bargmann [118]. Consequently, the total Cauchy stress in a single muscle fiber is described as

$$\sigma_{\text{fiber}} = \sigma_{\text{fiber_pas}} + \sigma_{\text{fiber_act}} + \sigma_{\text{fiber_titin}}. \quad (4.1)$$

$\sigma_{\text{fiber_pas}}$ and $\sigma_{\text{fiber_act}}$ are the passive and active components of the Cauchy stress tensor and $\sigma_{\text{fiber_titin}}$ denotes the additional stress in eccentric contractions due to titin. In an isometric contraction or if the muscle fiber is only passively stretched, the titin stress $\sigma_{\text{fiber_titin}}$ vanishes.

4.3.1.1.1 Passive elastic behavior

The passive Cauchy stress of muscle fibers reads

$$\sigma_{\text{fiber_pas}} = \frac{2}{J} \mathbf{F} \cdot \frac{\partial \Psi_{\text{fiber_pas}}}{\partial \mathbf{C}} \cdot \mathbf{F}^T, \quad (4.2)$$

where \mathbf{C} is the right Cauchy-Green tensor, \mathbf{F} the deformation gradient and \mathbf{F}^T the transpose of \mathbf{F} . $J = \det \mathbf{F}$ is the determinant of the deformation gradient, the Jacobian determinant. An

isotropic⁵ Neo-Hookean passive strain energy density function $\Psi_{\text{fiber pas}}$ is used for muscle fibers in two-phase muscle models, see also [19, 203]. The passive strain energy density function $\Psi_{\text{fiber pas}}$ is split into a distortional strain energy density function $\hat{\Psi}_{\text{fiber pas}}$ and a volumetric strain energy density function $\Psi_{\text{vol, fiber pas}}$

$$\begin{aligned}\Psi_{\text{fiber pas}} &= \hat{\Psi}_{\text{fiber pas}} + \Psi_{\text{vol, fiber pas}} \\ &= \frac{1}{2}\mu_{\text{fiber}}[\text{tr}\hat{\mathbf{C}} - 3] + \frac{1}{2}\kappa_{\text{fiber}}[J - 1]^2,\end{aligned}\quad (4.3)$$

with the shear modulus μ_{fiber} , the distortional part of the right Cauchy-Green tensor $\hat{\mathbf{C}} = J^{-2/3}\mathbf{C}$ and the bulk modulus κ_{fiber} . Thus, the Cauchy stress tensor $\sigma_{\text{fiber pas}}$ (Eq. (4.2)) becomes

$$\sigma_{\text{fiber pas}} = \frac{\mu_{\text{fiber}}}{J} \left[\hat{\mathbf{B}} - \frac{1}{3}\text{tr}(\hat{\mathbf{B}})\mathbf{I} \right] + \kappa_{\text{fiber}}[J - 1]\mathbf{I}, \quad (4.4)$$

where \mathbf{I} denotes the second order identity tensor, $\hat{\mathbf{B}}$ the distortional part of the left Cauchy-Green tensor \mathbf{B} with $\hat{\mathbf{B}} = J^{-2/3}\mathbf{B}$ and $\text{tr}(\hat{\mathbf{B}})$ the trace of $\hat{\mathbf{B}}$.

4.3.1.1.2 Active elastic behavior

The active stress function P_{act} [87]

$$\frac{\partial \Psi_{\text{fiber act}}}{\partial \lambda_{\text{fiber}}} = P_{\text{act}} = \bar{\gamma} f(\lambda_{\text{fiber}}) P_{\text{max}}, \quad (4.5)$$

consists of the activation parameter $\bar{\gamma}$, the maximum isometric active stress P_{max} and the normalized force-length relation f , which depends on the fiber stretch λ_{fiber} . This function determines the active component of the second Piola-Kirchhoff stress tensor [87]

$$\mathbf{S}_{\text{fiber act}} = \bar{\gamma} f(\lambda_{\text{fiber}}) \frac{1}{\lambda_{\text{fiber}}} P_{\text{max}} \mathbf{a}_0 \otimes \mathbf{a}_0 \quad (4.6)$$

with the unit vector \mathbf{a}_0 aligned in fiber direction in the reference configuration. Eq. (4.6) describes the active behavior of electrically activated muscle fibers with the active stress acting along the fiber direction. The fiber stretch λ_{fiber} is calculated by $\lambda_{\text{fiber}} = \sqrt{\text{tr}(\mathbf{C} \cdot [\mathbf{a}_0 \otimes \mathbf{a}_0])}$.

The activation parameter $\bar{\gamma} \in [0, 1]$ indicates the degree of activation of the fiber. We assume that the degree of activation along the fiber is approximately equal so that a constant activation parameter $\bar{\gamma}$ is used along the muscle fiber. The normalized force-length relation $f(\lambda_{\text{fiber}})$ describes the force generation of a sarcomere which strongly depends on its length and is for-

⁵We consider the material to be isotropic because the fiber anisotropy hardly influences the behavior in the load cases considered in this work.

ulated as a function of the fiber stretch λ_{fiber} , following [240],

$$f(\lambda_{\text{fiber}}) = \max\left(0.0015 \left[\frac{\lambda_{\text{fiber}} l_{s_0}}{l_{\text{norm}}}\right]^4 + 0.018 \left[\frac{\lambda_{\text{fiber}} l_{s_0}}{l_{\text{norm}}}\right]^3 - 0.935 \left[\frac{\lambda_{\text{fiber}} l_{s_0}}{l_{\text{norm}}}\right]^2 + 4.078 \frac{\lambda_{\text{fiber}} l_{s_0}}{l_{\text{norm}}} - 3.715; 0\right). \quad (4.7)$$

l_{s_0} denotes the resting sarcomere length and $l_{\text{norm}} = 1.0 \mu\text{m}$ normalizes the function. The product of the sarcomere resting length l_{s_0} and the fiber stretch λ_{fiber} yields the current sarcomere length l_s .

The active component of the Cauchy stress reads

$$\begin{aligned} \boldsymbol{\sigma}_{\text{fiber act}} &= \frac{1}{J} \mathbf{F} \cdot \mathbf{S}_{\text{fiber act}} \cdot \mathbf{F}^T \\ &= \frac{P_{\text{max}}}{J \lambda_{\text{fiber}}} \bar{\gamma} f(\lambda_{\text{fiber}}) \mathbf{a} \otimes \mathbf{a}. \end{aligned} \quad (4.8)$$

The current fiber direction $\mathbf{a} = \mathbf{F} \cdot \mathbf{a}_0$ in the deformed state is updated during the simulation, if the pennation angle changes.

4.3.1.1.3 Titin's force enhancement

Two factors influence titin's force enhancement in eccentric contractions: (i) the rise of intracellular calcium that increases the stiffness with sarcomere length [117] and (ii) the reduction of titin's free molecular spring length by attaching to the actin filaments (titin-actin interaction) [161]. The resulting additional stresses by titin in eccentric contractions can be described by the following stress equation [34] acting in the current fiber direction

$$\begin{aligned} \boldsymbol{\sigma}_{\text{fiber titin}} &= [h_1 [(\lambda_{\text{fiber}} - 1) + \varepsilon_{\text{shift}}]^3 + h_2 [(\lambda_{\text{fiber}} - 1) + \varepsilon_{\text{shift}}]^2 \\ &\quad + h_3 [(\lambda_{\text{fiber}} - 1) + \varepsilon_{\text{shift}}]] P_{\text{max}} \mathbf{a} \otimes \mathbf{a} \end{aligned} \quad (4.9)$$

with the constants $h_1 = 3.2$, $h_2 = 4.6$, $h_3 = -0.5$ and $\varepsilon_{\text{shift}} = 0.11$.

Both, calcium-sensitive tension and titin-actin interaction, are taken into account. Eq. (4.9) only describes the additional stresses of titin during active stretching and not the entire passive stresses. Therefore, the constants are adjusted based on a parameter fitting simulation with validation against experimental data for the fiber force–fiber stretch behavior in eccentric contractions [211]. The high influence of titin for eccentric contractions resulting in increasing fiber stresses is visible in Fig. 4.4.

Eq. (4.9) describes titin's additional stresses for the case that the eccentric contraction starts at the point of maximum active force in the force-length relation, which can be generated close to the sarcomere's resting length. However, no significant differences exist in the development of the titin stresses around the resting length [86, 147, 180]. Therefore, we set the resting sarcomere length $l_{s_0} = 2.0 \mu\text{m}$ as the initial length for an eccentric contraction.

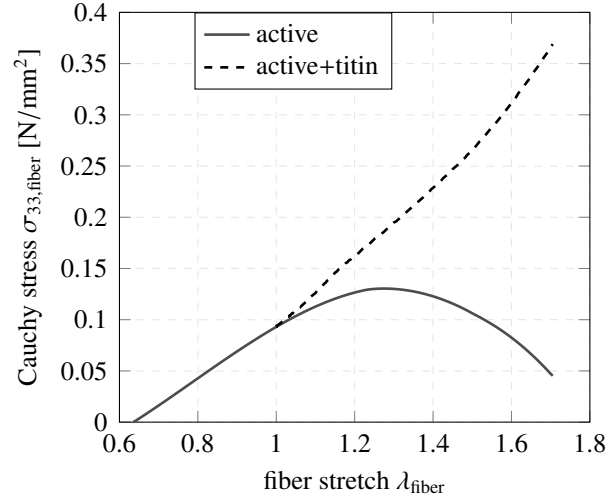


Figure 4.4: The active stress $\sigma_{33, \text{fiberact}}$ (Eq. (4.8)) and the sum of the active and titin stress $\sigma_{33, \text{fiberact}} + \sigma_{33, \text{fibertitin}}$ (Eq. (4.8) + Eq. (4.9)) are shown in fiber direction. Titin's strongly nonlinear stress-strain curve ensures an increase in the stress-strain curve when an activated fiber is lengthened.

4.3.1.2 Plastic behavior

If the muscle fiber is stretched beyond its yield point the slack sarcomere length is increased and the stiffness is reduced due to structural changes [142, 222]. Furthermore, high deformations result in initial damage, e.g. during eccentric contractions, which can occur at the fiber membrane [4, 49, 142] (e.g. sarcolemma disruption), within the fiber at myofibril level [65, 145] (e.g. misalignment of myofibrils), or at sarcomere level [63, 65] (e.g. z-disk dissolution). Irreversible deformation and microcracks in the muscle fiber are described by the Johnson-Cook model⁶.

The Johnson-Cook flow stress behavior of materials reads

$$\sigma_{eq} = [A + B\varepsilon_{eq,p}^n] [1 + C \ln(\dot{\varepsilon}_p^*)] [1 - T^{*m}], \quad (4.10)$$

with the equivalent von Mises flow stress σ_{eq} , the equivalent plastic strain $\varepsilon_{eq,p}$, the dimensionless plastic strain rate $\dot{\varepsilon}_p^*$ and the homologous temperature T^{*m} . A denotes the fiber yield stress, B the strain hardening constant, n the strain hardening coefficient, C the strain rate strengthening coefficient and m the thermal softening coefficient.

The equivalent von Mises flow stress reduces to

$$\sigma_{eq} = A + B\varepsilon_{eq,p}^n \quad (4.11)$$

for deformations at room temperature and at a strain velocity close to zero, which we assume henceforth.

⁶The Johnson-Cook model is widely used to model plastic deformation of metallic materials, however, applications also exist in the field of biomechanics [1, 16, 71, 178].

4.3.1.3 Damage model

At higher strains, myofibrillar failure occurs, causing myofibrils to fail in small bundles [142], which results in the immediate failure of the entire muscle fiber. Similar to [31] for biological soft tissues, we apply an anisotropic damage model. Here, it is assumed that the damage function $g_{D,\text{fiber}}$ is independent of the damage variable, so that the distortional part of the total Cauchy stress tensor $\hat{\sigma}_{D,\text{fiber}}$ for damaged fibers is expressed as

$$\hat{\sigma}_{D,\text{fiber}} = g_{D,\text{fiber}}(\lambda_{\text{fiber}})\hat{\sigma}_{\text{fiber}} \quad (4.12)$$

with the total distortional Cauchy stress $\hat{\sigma}_{\text{fiber}}$ [200]. The damage function $g_{D,\text{fiber}}$ depends on the fiber stretch λ_{fiber}

$$g_{D,\text{fiber}}(\lambda_{\text{fiber}}) = \begin{cases} 1 & \text{for } \lambda_{\text{fiber}} < \lambda_{\text{fiber},\text{min}} \\ \frac{1 - e^{\beta[\lambda_{\text{fiber}} - \lambda_{\text{fiber},\text{max}}]}}{1 - e^{\beta[\lambda_{\text{fiber},\text{min}} - \lambda_{\text{fiber},\text{max}}]}} & \text{for } \lambda_{\text{fiber}} \geq \lambda_{\text{fiber},\text{min}} \\ & \text{and } \lambda_{\text{fiber}} \leq \lambda_{\text{fiber},\text{max}} \\ 0 & \text{for } \lambda_{\text{fiber}} > \lambda_{\text{fiber},\text{max}} \end{cases} \quad (4.13)$$

where β is the exponential damage parameter. For stretches $\lambda_{\text{fiber}} < \lambda_{\text{fiber},\text{min}}$, the Johnson-Cook model captures the existing microcracks and, therefore, the value of the function is $g_{D,\text{fiber}} = 1$. If the stretch exceeds $\lambda_{\text{fiber},\text{min}}$, myofibrils fail, usually in small bundles. The resulting sharp drop in the stress-strain curve is described by the function $g_{D,\text{fiber}}$. Exceeding the stretch $\lambda_{\text{fiber},\text{max}}$ results in failure of the entire muscle fiber and, thus, $g_{D,\text{fiber}}$ is equal to zero.

4.3.2 Connective tissue endomysium

The isotropic hyperelastic first order Ogden model is used to depict the highly nonlinear passive stress-strain behavior of the connective tissue endomysium, compare also [118]. Isotropic material behavior is assumed as the influence of the anisotropy of endomysium due to the collagen fibers can be neglected for the considered load cases. The strain energy density function Ψ_{endo} is expressed in terms of the principal stretches and is split into a distortional $\hat{\Psi}_{\text{endo}}$ and a volumetric strain energy density function U_{endo}

$$\begin{aligned} \Psi_{\text{endo}} &= \hat{\Psi}_{\text{endo}} + U_{\text{endo}} \\ &= \frac{2\mu_{\text{endo}}}{\alpha_1^2} \left[\hat{\lambda}_1^{\alpha_1} + \hat{\lambda}_2^{\alpha_1} + \hat{\lambda}_3^{\alpha_1} - 3 \right] + \frac{1}{2}\kappa_{\text{endo}} [J - 1]^2. \end{aligned} \quad (4.14)$$

α_1 is a dimensionless constant, μ_{endo} the shear modulus, κ_{endo} the bulk modulus and $\hat{\lambda}_i = J^{-1/3}\lambda_i$ are the distortional parts of the principal stretches λ_i .

The second Piola-Kirchhoff stress tensor \mathbf{S}_{endo} is calculated via

$$\mathbf{S}_{\text{endo}} = 2 \frac{\partial \Psi_{\text{endo}}}{\partial \mathbf{C}} \quad (4.15)$$

$$= \frac{2\mu_{\text{endo}} J^{-\frac{1}{3}\alpha_1}}{\alpha_1} \sum_{i=1}^3 \lambda_i^{\alpha_1} \left[\lambda_i^{-2} \mathbf{e}_i \otimes \mathbf{e}_i - \frac{1}{3} \mathbf{C}^{-1} \right] + \kappa_{\text{endo}} [J - 1] J \mathbf{C}^{-1}. \quad (4.16)$$

Thus, the Cauchy stress can be determined:

$$\boldsymbol{\sigma}_{\text{endo}} = \frac{1}{J} \mathbf{F} \cdot \mathbf{S}_{\text{endo}} \cdot \mathbf{F}^T \quad (4.17)$$

$$= \frac{2\mu_{\text{endo}} J^{-\frac{1}{3}\alpha_1 - 1}}{\alpha_1} \sum_{i=1}^3 \lambda_i^{\alpha_1} \left[\lambda_i^{-2} \mathbf{F} \cdot [\mathbf{e}_i \otimes \mathbf{e}_i] \cdot \mathbf{F}^T - \frac{1}{3} \mathbf{I} \right] + \kappa_{\text{endo}} [J - 1] \mathbf{I}. \quad (4.18)$$

4.4 3D computational models of fascicles

The representative volume element (RVE) [10] of the fascicle consists of round and parallel aligned muscle fibers which are periodically arranged and embedded in the matrix endomysium. The muscle fibers and endomysium are perfectly bonded by sharing nodes at the interface. Periodic boundary conditions are applied.

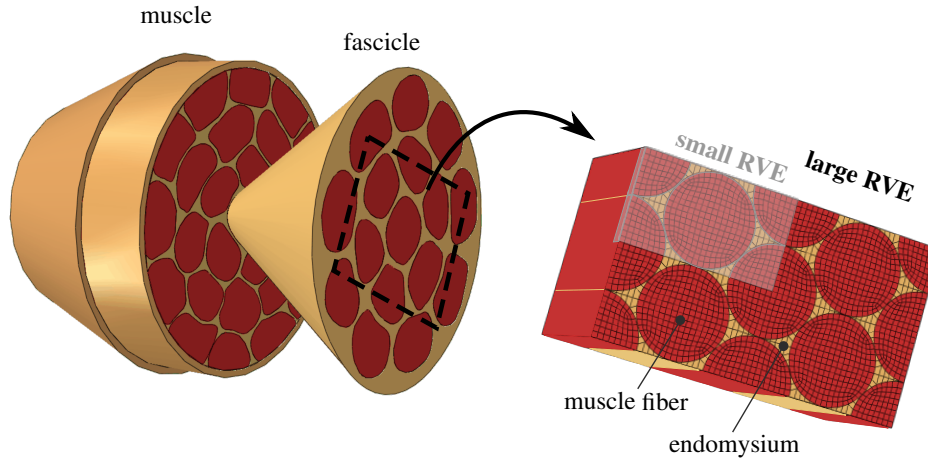


Figure 4.5: The fascicle is modeled using two differently sized 3D representative volume elements. The elements are periodic, so the large RVE is a multiple of the smaller one. Both RVEs are discretized with linear fully integrated hexahedral elements. For the small RVE, one element in fiber direction is used, which reduces the computational cost. In total, the small RVE is discretized in 552 elements. The larger RVE consists of 33120 elements and allows to consider small defects along the fiber as it is fully discretized along that direction.

We model two fascicle RVEs (Fig. 4.5) for the EDL muscle of mice with a fiber volume fraction

of 90%⁷ and a fiber diameter of $d_{\text{fiber}} = 47.5 \mu\text{m}$ which corresponds to the median of the measured EDL fiber diameters of wild-type mice [189]. As the degree of activation is constant along the fiber direction, both RVE depths do not correspond to the real muscle fiber length, which reduces the computational cost. The smaller RVE consists of fewer fibers and is used to obtain general information about the damage behavior in fascicles (see Sect. 4.5.1). The larger RVE is used to analyze the influence of pre-damaged fibers in fascicles (see Sect. 4.5.2).

The material and geometrical data is summarized in the appendix. To verify the general validity of the model, the results of additional simulations with varying fiber-endomysium-Young's modulus ratios, different fiber shapes and higher fiber volume fractions are presented in the supplementary material. These results show no differences to the curves presented in the following section.

4.5 Results: Computational modeling of damage in fascicles

This work studies the mechanical behavior of titin and endomysium in the case of pre-damaged muscle fibers in the muscle belly on the fascicle level. Stretching due to eccentric contraction is modeled until complete muscle fiber rupture. This load case grants novel insights into the development of indirect muscle injuries. We consider low strain rates and, thus, do not take viscoelastic effects into account.

A realistic loading case is modeled for EDL fascicles, which includes combined tensile and shear loading. First (see Sect. 4.5.1), we examine the damage behavior of previously intact muscle fibers embedded by endomysium at fascicle level. Then (see Sect. 4.5.2), at the same level, we consider various pre-damaged fibers with different amounts of damage and study the influence of titin and endomysium on the damage process in the entire fascicle, i.e., in the pre-damaged fiber and the adjacent, initially undamaged fibers.

Fig. C.1 in the appendix verifies the accuracy and implementation of the model as our simulation results perfectly match the experiments for actively stretched (eccentric contraction) muscle fibers.

4.5.1 Damage behavior and injury of previously fully intact muscle fibers on the fascicle level

In the unipennate EDL muscle, the pennation angle of the fibers is 10° [223]. Lengthening the muscle in tendon direction, therefore, results in tensile and shear stresses. This realistic loading of EDL fascicles is simulated for previously fully intact muscle fibers⁸. In Fig. 4.6, the forces in tendon direction until total fiber rupture are plotted against the muscle fiber stretch for passively

⁷The entire muscle has a fiber volume fraction of $95\% \pm 8.8\%$ [129].

⁸The pennation angle changes for this loading case. Thus, α has to be updated during the simulation.

and actively stretched fascicles. Here, the fascicle force is the force within the small RVE (Fig. 4.5) and, thus, only a fraction of the force generated in an entire fascicle.

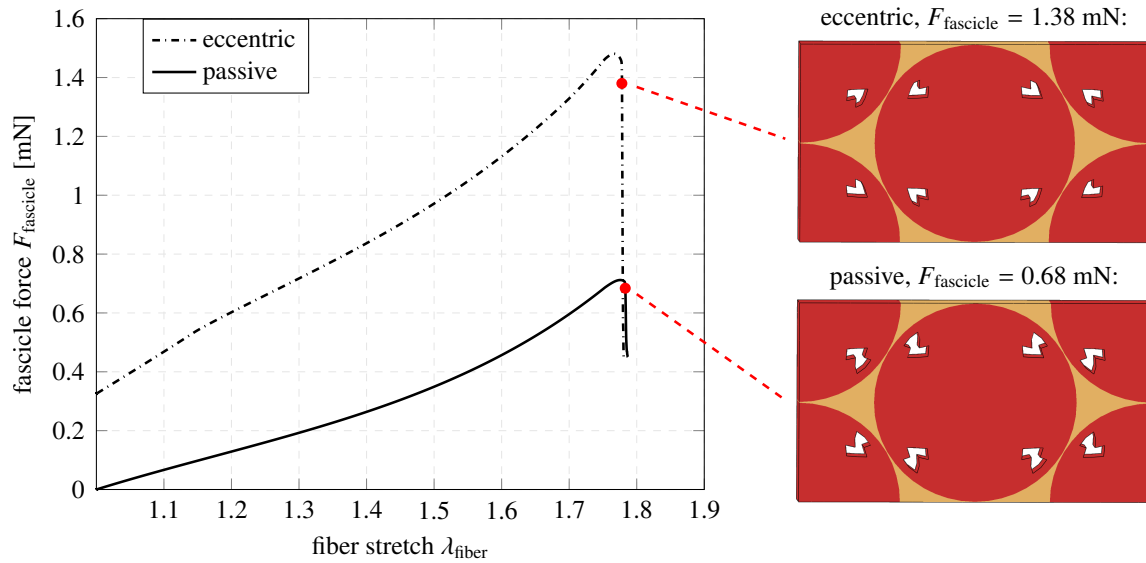


Figure 4.6: Fascicle force–fiber stretch relationships are depicted until total fiber rupture for the passively and actively stretched (eccentric contraction) small fascicle RVE. In both cases, the fascicle forces increase nonlinearly due to the strongly raising passive forces in the endomysium. This is in contrast to the approximately linear force–fiber stretch behavior of isolated muscle fibers. Due to titin’s force enhancement, the RVE force in eccentric contraction is much higher than in a passively stretched fascicle. Right: Damage most likely occurs near the boundary of the fiber.

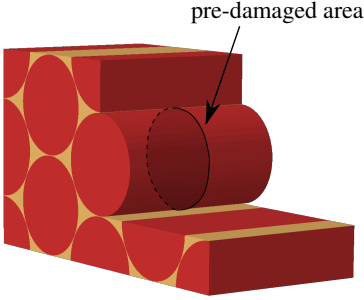
The force–stretch curves of passively and actively stretched muscle fibers are approximately linear ([138] for passively stretched and [86, 180] and the appendix for actively stretched). In fascicles, the curves are nonlinear due to the properties of endomysium (Fig. 4.6). Over the complete strain range, the force–stretch curve in eccentric contraction increases stronger than for passive loading. This is due to titin’s force enhancement (examined and discussed in the appendix in more detail) which stables contractions on the descending limb of the force–length relation (Fig. 4.4). The force in actively stretched fascicles reaches more than twice the force in passively stretched fascicles before fiber rupture.

As described in Sect. 4.3.1.3, the fiber strain is responsible for the entire fiber rupture. In the simulations, fascicles tear at strains of 75 % (see Fig. 4.6) - corresponding well to the rupture strain in fiber direction of $66.4 \pm 27.6\%$ in the experiments of tensile loaded human quadriceps femoris muscles [186]. Tearing of muscle fibers for $\lambda_{\text{fiber}} > 1.75$ results in a reduction of fiber forces and, thus, in decreased fascicle forces. Since endomysium is not damaged and is able to carry the load, the simulated force is non-zero after total fiber rupture.

4.5.2 Damage behavior and injury with pre-damaged muscle fibers on the fascicle level

We investigate pre-damaged muscle fibers and their influence on neighboring fibers and the macroscopic strain of the entire fascicle. A large fascicle RVE (Fig. 4.5) is used to study the interaction with multiple neighboring fibers in the model. As in Sect. 4.5.1, the same realistic loading case of EDL fascicles is modeled and an actively stretched fascicle is examined.

The fiber in the RVE's center is pre-damaged (Fig. 4.7). This is modeled by reducing the passive fiber Young's modulus in the cross-section. For the active behavior and titin's force enhancement, the total active stress (Eq. (4.8)) and titin's additional stress (Eq. (4.9)) are reduced by the amount of pre-damage.



active fiber yield stress A_{act} depending on pre-damage:

amount of pre-damage	10 %	20 %	30 %	40 %	50 %
intact titin	$0.1555 \frac{N}{mm^2}$	$0.1407 \frac{N}{mm^2}$	$0.1264 \frac{N}{mm^2}$	$0.1115 \frac{N}{mm^2}$	$0.0968 \frac{N}{mm^2}$
damaged titin	$0.1529 \frac{N}{mm^2}$	$0.1356 \frac{N}{mm^2}$	$0.1188 \frac{N}{mm^2}$	$0.1017 \frac{N}{mm^2}$	$0.0846 \frac{N}{mm^2}$
amount of pre-damage	60 %	70 %	80 %	90 %	
intact titin	$0.0824 \frac{N}{mm^2}$	$0.068 \frac{N}{mm^2}$	$0.0533 \frac{N}{mm^2}$	$0.039 \frac{N}{mm^2}$	
damaged titin	$0.0679 \frac{N}{mm^2}$	$0.0509 \frac{N}{mm^2}$	$0.0339 \frac{N}{mm^2}$	$0.017 \frac{N}{mm^2}$	

Figure 4.7: Left: pre-damaged central muscle fiber. Right: The active fiber yield stress for an eccentric contraction is calculated for nine different degrees of pre-damage. Furthermore, we differentiate between equally pre-damaged titin ("damaged titin") and undamaged titin ("intact titin").

Two different kinds of pre-damaged fibers are investigated: one with and one without pre-damaged titin. For every case of pre-damage, the active fiber yield stress A_{act} is determined (Fig. 4.7). The yield stress corresponds to the stress at a fiber stretch of $\lambda_{fiber} = 1.1457$ which is the stretch at which damage is initiated under eccentric contraction [84]. The Johnson-Cook strain hardening constant $B = 0.385$ and coefficient $n = 0.739$ are the same for each pre-damaged muscle fiber.

4.5.2.1 Titin's mechanical behavior

The macroscopic fiber stretch λ_{fiber} of the fascicle RVE and the maximum principal logarithmic strain ε_1 in the pre-damaged fiber area depend on the degree of pre-damage (Fig. 4.8). We investigate titin's influence in pre-damaged fibers by the cases where titin is equally pre-damaged or completely intact.

For an undamaged fascicle, a macroscopic fiber stretch of $\lambda_{fiber} = 1.75$ is reached before fiber rupture (Fig. 4.6). For a pre-damaged fascicle with pre-damaged titin, the macroscopic fiber stretch of the fascicle reached until fiber rupture of the pre-damaged area is reduced strongly

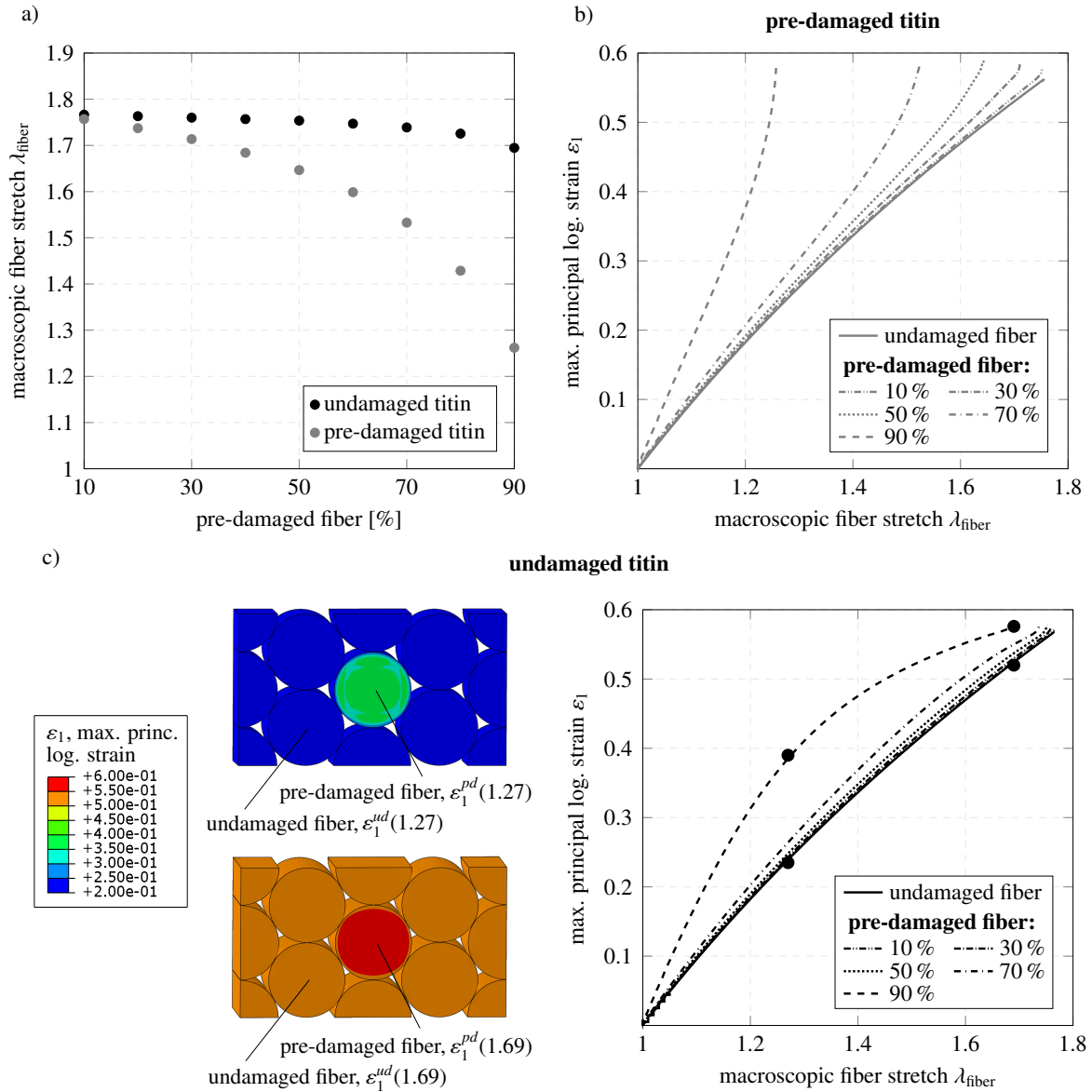


Figure 4.8: Influence of titin on the damage behavior in pre-damaged fascicles: the central muscle fiber of the large fascicle RVE is pre-damaged in one cross-section. a) The macroscopic fiber stretch of the fascicle reached before fiber rupture rapidly decreases for higher pre-damage if titin is equally pre-damaged. If titin is intact, the macroscopic fiber stretch remains nearly the same as in an undamaged fascicle ($\lambda_{\text{fiber}} = 1.75$, Fig. 4.6), even for a very high degree of pre-damage. b) For pre-damaged titin, the local strain in the pre-damaged fiber cross-section increases more strongly with higher pre-damage. c) For intact titin, the stronger increase of local strain in the pre-damaged fiber area with larger pre-damage is slowed down above a certain strain. This strain approaches the local strain in the neighboring undamaged fiber. On the left, the strain distributions in the RVE with 90% pre-damage are shown for two macroscopic fiber stretches. The RVEs visualize that local strains in the pre-damaged fiber (ε_1^{pd}) approach those in the undamaged fiber (ε_1^{ud}) for higher macroscopic fiber stretches. While at a stretch of $\lambda_{\text{fiber}} = 1.27$ the maximum principal strains in the pre-damaged fiber are 1.66 times larger than in the undamaged fiber, it is only a factor of 1.11 at a macroscopic stretch of $\lambda_{\text{fiber}} = 1.69$.

with increasing pre-damage, so that only a macroscopic fiber stretch of $\lambda_{\text{fiber}} \approx 1.26$ is obtained for 90 % pre-damage (Fig. 4.8a). In the case of a pre-damaged fascicle with undamaged titin, the macroscopic fiber stretch is hardly reduced, so that a total fiber stretch of $\lambda_{\text{fiber}} \approx 1.7$ is still achieved for 90 % pre-damage. In Fig. 4.8b and c, the maximum principal logarithmic strain ε_1 in the pre-damaged fiber cross-section and in a neighboring undamaged fiber is plotted over the macroscopic fiber stretch λ_{fiber} of the fascicle. The curve of the undamaged muscle fiber in b) and c) is represented by the one for 10 % pre-damage, as it coincides with the curves for higher pre-damage and only differs in the achieved macroscopic fiber stretch. In the pre-damaged part, the strains increase more strongly with higher pre-damage. For additionally pre-damaged titin (Fig. 4.8b), the macroscopic fiber stretch before fiber rupture is markedly reduced with increasing pre-damage, i.e., the fiber ruptures much faster. However, if titin is intact, the initially strongly increasing curves for higher pre-damage flatten above a certain strain. Independent of the amount of pre-damage, they converge to the behavior of the undamaged neighboring fiber (Fig. 4.8c). Therefore, the macroscopic fiber stretch of the fascicle is hardly reduced (Fig. 4.8a). On the left side of c), the strains in case of 90 % pre-damage are shown at two different macroscopic fiber stretches. The RVEs visualize that the strain level in the pre-damaged fiber approaches the strain level in the undamaged fiber for increasing macroscopic fiber stretches. As a result, large macroscopic strains can also be achieved with substantial fiber pre-damage.

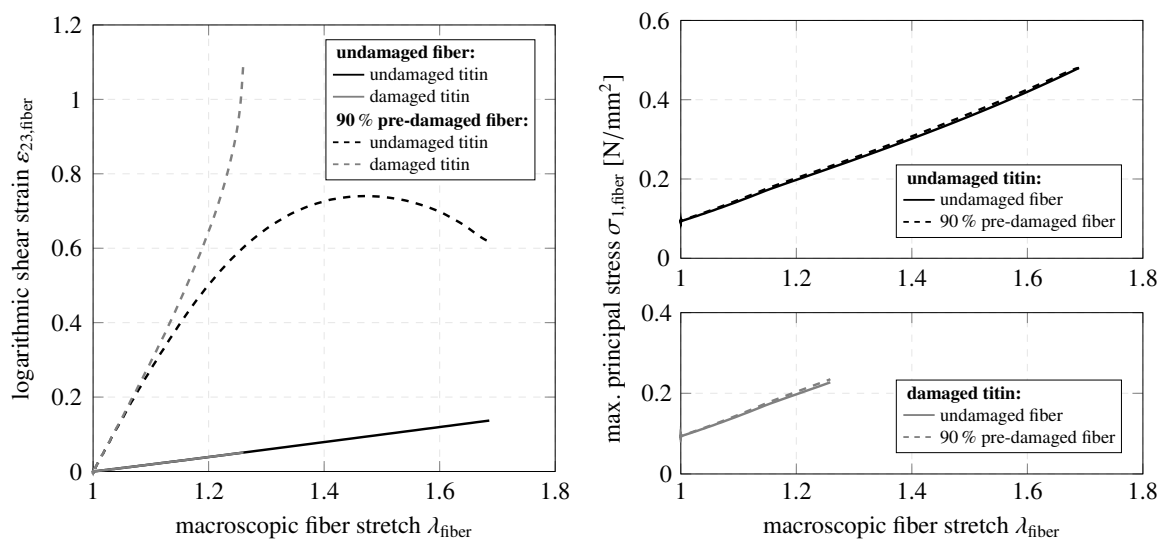


Figure 4.9: Titin's influence on the damage behavior in fascicles. Left: Shear strains at the point of maximum principal strains for the pre-damaged fiber cross-section and the undamaged adjacent fiber. Shear strains in the undamaged muscle fiber are quite low compared to the ones in the pre-damaged fiber area. In the pre-damaged area, the shear strains increase sharply, however, if titin is intact, the slope is reduced for higher macroscopic stretches so that the shear strain decreases even for $\lambda_{\text{fiber}} > 1.45$. Right: Despite the high degree of pre-damage, the stresses in the pre-damaged fiber area and in the adjacent undamaged fiber are nearly the same, both with pre-damaged titin and with intact titin.

The distribution of normal and shear strains is further elucidated in the appendix in Fig. C.3 where it is evident that the shear strains are the cause for the large maximum principal strains

in the pre-damaged fiber and, thus, the earlier fiber rupture. In Fig. 4.9, the logarithmic shear strains for 90 % pre-damage are plotted at the point of maximum principal strains in the pre-damaged and undamaged fiber for equally pre-damaged and intact titin.

In the undamaged fiber, the shear strains are quite small. If titin is intact, the shear strain increases linearly until fiber rupture. If titin is pre-damaged, too, the curve progression is the same, however, the macroscopic fiber stretch reached before fiber rupture is with $\lambda_{\text{fiber}} \approx 1.26$ much lower.

In the pre-damaged fiber cross-section, the shear strains increase sharply and nonlinearly with the fiber stretch. If the titin is pre-damaged, the curve increases exponentially until fiber rupture. If titin is intact, however, the curve of the shear strain flattens and even drops for higher macroscopic fiber stretches. This decrease in shear strain is the reason for the flattening of the maximum principal strains seen in Fig. 4.8c (more detailed information is provided in the appendix). The maximum principal strains in pre-damaged and undamaged fiber approach similar levels. Therefore, the pre-damaged fascicle reaches almost the same macroscopic strain as in the completely undamaged case ($\lambda_{\text{fiber}} \approx 1.75$, Fig. 4.6).

In Fig. 4.9b, the maximum principal stresses in the 90 % pre-damaged fiber part and the adjacent undamaged fiber are plotted over the macroscopic fiber stretch for equally pre-damaged and undamaged titin. Independent of titin, the stresses in the pre-damaged and undamaged fiber are approximately equal over the complete strain range.

4.5.2.2 Endomysium's mechanical behavior

To investigate the significant difference in the strain development between pre-damaged and undamaged fibers (Sect. 4.5.2.1), the strains in endomysium are examined more closely.

Fig. 4.10 shows the maximum principal logarithmic strains in the endomysium in the region of the 90 % pre-damaged muscle fiber with equally pre-damaged titin. The strains in the area connected to the pre-damaged region are compared to the strains connected to the adjacent previously undamaged fiber. Both curves increase linearly, however, even stronger next to the pre-damaged fiber than next to the undamaged fiber. Therefore, the strain reduction increases with the macroscopic fiber stretch. Despite its extremely thin thickness, the endomysium strongly reduces the strains from the pre-damaged fiber to the adjacent undamaged fiber. This results in the large difference of the maximum principal strains between the damaged and undamaged fiber and in the coincidence of the strain curves of the undamaged fibers, independent of the amount of pre-damage (Fig. 4.8b and c).

The rupture of the entire central muscle fiber at $\lambda_{\text{fiber}} = 1.26$ leads to a strong shear strain increase at the interface and, thus, both strain curves increase sharply. The crack propagates after fiber rupture which is shown in the two half RVEs in Fig. 4.10.

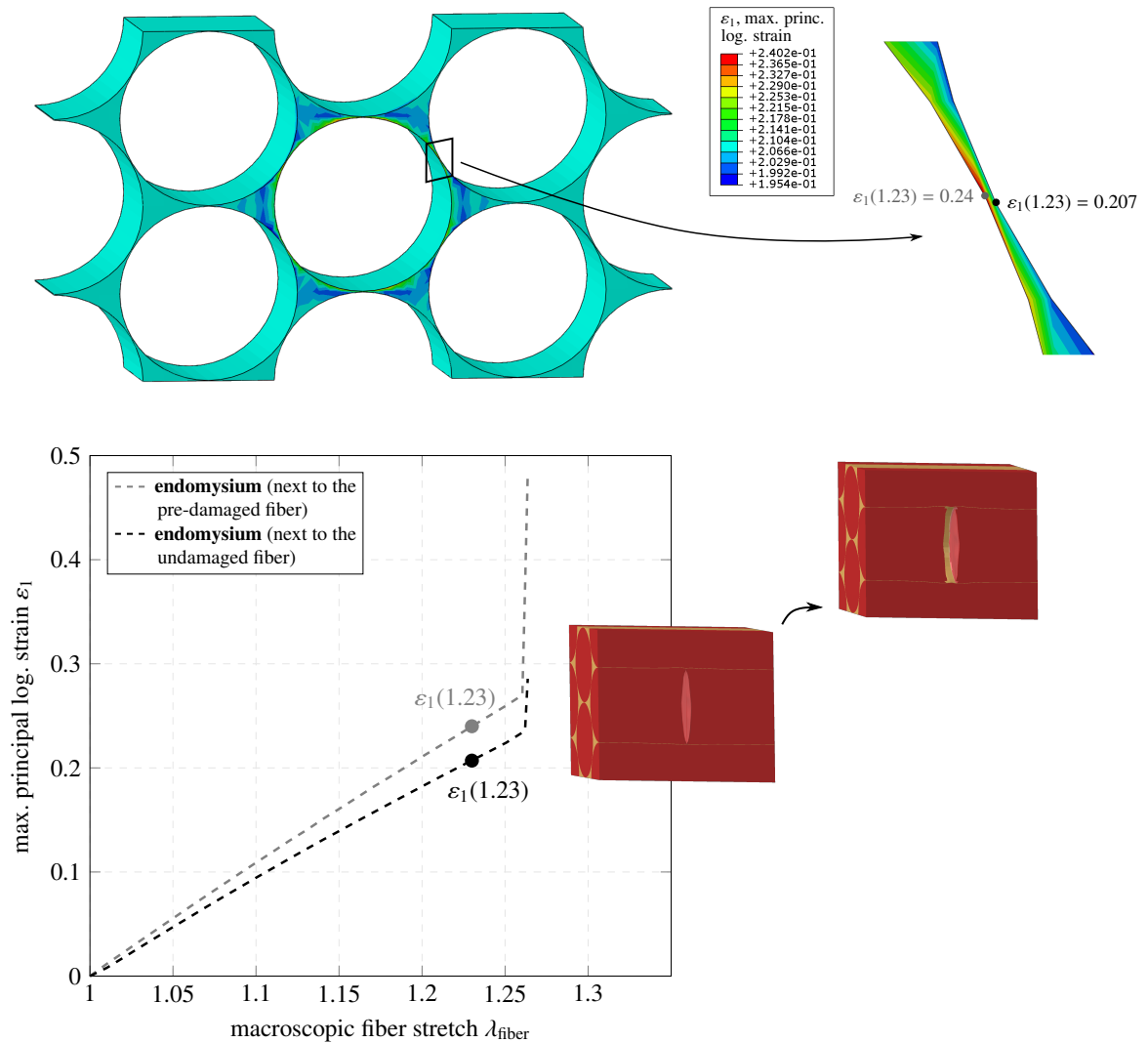


Figure 4.10: Endomysium's protection properties for adjacent undamaged muscle fibers in the case of a 90 % pre-damaged muscle fiber (titin is equally pre-damaged): The maximum principal logarithmic strains in the endomysium are examined where endomysium is thinnest next to the pre-damaged cross-section of the central muscle fiber. In the maximum principal log. strain–fiber stretch plot, the strain next to the pre-damaged fiber increases more strongly than the strain next to the undamaged fiber. The resulting strain difference is very large despite the thin endomysium. For a macroscopic fiber stretch of $\lambda_{\text{fiber}} = 1.23$, a detail of endomysium in the area of the 90 % pre-damaged muscle fiber shows a decrease of strain from $\varepsilon_1 = 0.24$ to $\varepsilon_1 = 0.207$, equivalent to a reduction of almost 14 %. After fiber rupture ($\lambda_{\text{fiber}} > 1.26$), both strain curves increase strongly due to the high shear strains at the interface. The two half fascicle RVEs present the crack propagation in the central muscle fiber after fiber rupture.

4.6 Discussion

We studied the initiation of cracks in muscle fibers of an unipennate muscle, in particular the EDL muscle. For an undamaged fascicle, the muscle fiber boundaries, i.e. the sarcolemma, are at risk to fail first (Fig. 4.6). In these areas, the shear strains are largest which is the case in pennate muscles subjected to multiaxial loading. In tensile loaded parallel muscles, no shear occurs, and, thus, the sarcolemma is at lower risk to fail as the strain is distributed over the entire fiber.

One of titin's important tasks is force regulation, which increases stability of sarcomeres on the descending limb and, therefore, protects against overstretching and the resulting damage [2, 80, 81, 92, 131]. We investigated titin's behavior in a pre-damaged muscle fiber and gained new insights into its protective properties. Even with extensive pre-damage, titin provides additional stiffness that allows the muscle to withstand macroscopic strains that are almost as large as those in the undamaged muscle fiber.

As titin's stiffness increases exponentially with strain, the stresses in the entire muscle fiber increase exponentially (Fig. C.2 in the Appendix). Thus, titin stabilizes sarcomeres on the descending limb of the force-length curve (see also Fig. 4.4). Titin's high material stiffness allows to compensate high pre-damage and to maintain equal maximum principal stresses in the pre-damaged and adjacent undamaged fiber at the cost of locally extremely large shear strains in the pre-damaged fiber (Fig. 4.9). At the point of maximum shear strain for the case of 90% pre-damage (and intact titin), the shear strain in the pre-damaged fiber is almost 8 times higher than in an undamaged fiber. If the titin remains intact, its stiffness increase results in a global stiffening of the muscle fiber. This increases the resistance against further shearing and causes a transition to more tensile loading that, at high macroscopic fiber stretches, results in shear strain reduction. Thus, even strongly pre-damaged fibers only break slightly earlier than initially undamaged ones (Fig. 4.8). If titin is equally pre-damaged, this stiffening cannot be provided and the pre-damaged fibers fail at significantly lower macroscopic strains.

Recent studies indicate that the connective tissue endomysium transmits the contractile fiber force to adjacent fibers via trans-laminar shear rather than via in-plane tension [166, 214]. It has been found that this stress transfer and endomysium's stabilizing behavior protect injured areas and contribute to their repair [132, 206].

Our results show that endomysium also protects undamaged muscle fibers from the large strains in adjacent pre-damaged fibers. Endomysium prevents damage to travel into the undamaged muscle fibers by accommodating and relieving the high strains. The strains are drastically reduced over the endomysium, even if its thickness is very small (Fig. 4.10). Furthermore, we showed that the amount of pre-damage in a muscle fiber does not affect the deformation behavior of the adjacent, undamaged fibers. Thus, findings of [132, 206] that endomysium protects damaged fiber areas, can be extended to that it also protects adjacent undamaged fibers from pre-damaged ones.

4.7 Conclusion

We developed a continuum mechanical model for the damage behavior of fascicles, which incorporates damage initiation as well as its evolution until total muscle fiber rupture. The fascicle itself is modeled using an RVE of EDL fascicle of mice that is subjected to a realistic loading case consisting of normal and shear forces. We analyzed the location of crack initiation in fascicles and confirmed the findings of [118] that the boundary of the muscle fiber in unipennate muscles, i.e. the sarcolemma, is at high risk for crack initiation. Furthermore, our results give new insights into the mechanical behavior of lower level components, especially of the giant molecule titin and the connective tissue endomysium, in damaged skeletal muscles. Here, we considered injuries in the muscle belly and not at the musculotendinous junction.

Our simulations show that titin serves an important protective function in pre-damaged muscle fibers and stabilizes even strongly pre-damaged fibers. Thus, titin not only provides stability on the descending limb of the generated active stress in undamaged sarcomeres, it also protects damaged fiber regions from large strains. The additional stiffening provided by titin reduces the shear strains in the muscle fiber which would lead to early rupture and facilitates macroscopic strains of a similar magnitude as in an undamaged fascicle. Thus, even strongly pre-damaged fibers are protected from more serious injuries. If titin is also damaged, muscle fibers are at higher risk of tearing earlier, even at only minor degrees of pre-damage.

Furthermore, the results indicate that endomysium not only protects pre-damaged fibers as mentioned in [132, 206], but additionally protects adjacent undamaged fibers from the high strains in the pre-damaged ones. Endomysium almost fully prevents the transfer of these strains which avoids damage propagation to neighboring fibers and stabilizes the skeletal muscle.

5 | Article 4:

Mechanisms of thermal treatments in trigger points of the skeletal muscle: computational microstructural modeling

5.1 Abstract

Thermal treatment of trigger points in muscle fibers is easily applied without professional assistance and, thus, popular. In this work, we study the influence of thermotherapy and cryotherapy on trigger points in a fascicle by means of a microstructural model. Details about the mechanisms of different thermal treatments to relieve muscle tension in tensed muscle fibers are provided. We consider short-term as well as long-term temperature treatment. For the former, the electromyography activity in the trigger point is assumed to remain constant. This results in reduced muscle tension after heating, as the compressive strains and compressive passive stresses in the trigger point are reduced, however, cooling causes the opposite behavior and enhances muscle tension. The different thermal expansion coefficients along the tensed muscle fiber provide maximum relaxation during heating, as the fiber regions next to the trigger point contribute to relaxation. Long-term treatment reduces the electromyography activity in the trigger point as in in vivo muscles and electromyography activity reduction strongly effects the behavior along the entire tensed fiber, thus, relief of muscle tension in trigger points is not only obtained during heating but also during cooling.

5.2 Introduction

Muscle tension can be caused by a variety of circumstances: not only due to sports, but also due to e.g. computer work or daily stress. The most frequently mentioned physical complaints of adults are headaches [235] and about 40 % of the victims suffer from tension headaches [112]. Tension headaches are often induced by muscle tension, especially by myofascial trigger points [201]. Trigger points are tender spots in taut bands of a tensed muscle and cause local and referred pain [25]. They consist of about 100 permanently contracted (i.e. shortened) sarcomeres

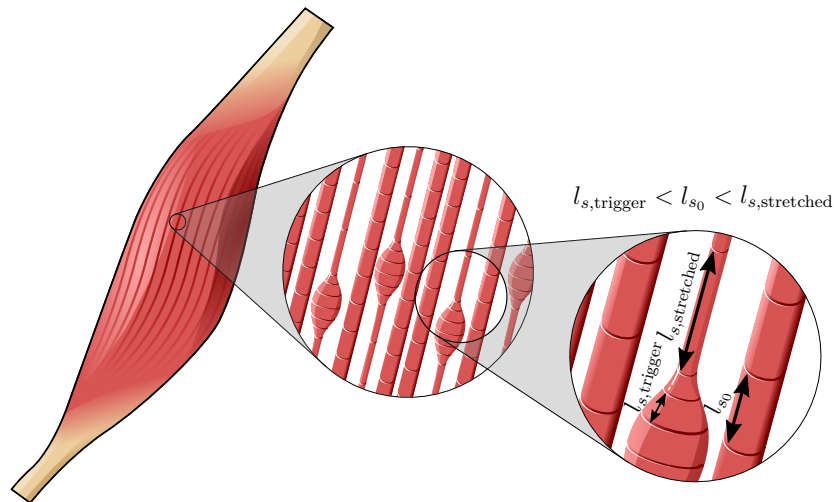


Figure 5.1: Muscle trigger points: Sarcomeres of muscle fibers can be permanently contracted even when they are no longer activated. These regions occur as thicker knots along the fibers and are called trigger points. These result in shorter sarcomeres in the trigger points (length $l_{s,trigger}$) and stretched sarcomeres (length $l_{s,stretched}$) close to the trigger points in the same muscle fiber [187]. The length of a sarcomere without trigger points is called resting length l_{s_0} .

within a fascicle without any nerve stimulus input [197] and form a contraction knot (Fig. 5.1) with an increased stiffness and diameter. The crossbridges between actin and myosin remain interconnected in the trigger point although the muscle fiber is not activated. In the extreme case of rigor muscle fibers, almost all crossbridges are permanently attached [38] and, thus, the entire fiber does not participate in biochemical reactions.

One application to reduce muscle tension is thermal treatment. Thermo- and cryotherapy have specific physiological effects and are applied for different muscular injuries. Both, heat and cold treatment, relieve pain and muscle spasms, however, inflammation, edema, tissue metabolism, connective tissue extensibility and blood flow are increased by thermotherapy and decreased by cryotherapy [144]. Specifically for trigger points, studies of different heat treatments showed reduced pain [157] and decreased stiffness [48], even stronger in combination with electrotherapy [122]. Cold treatment reduces the degree of activation in the trigger point, even stronger than heat treatment [162]. Besides heat and cold applications, trigger points can be treated in different ways, for example by ischemic compression, dry needling, transcutaneous electrical nerve stimulation, medication, etc. Nevertheless, temperature treatments are of high interest because they do not require professional assistance and can be performed easily at home.

For artificial muscles, the temperature dependent behavior has been studied using computational modeling, e.g. [111, 163, 196]. For soft tissues, [59] introduced a boundary element fractional model to describe the bio-thermomechanical properties of anisotropic soft tissues. Thermoelastic modeling of the skin layer was done by e.g. [134, 198, 236]. For biological muscles, a continuum model which includes thermomechanical reactions in the muscle was used in [17] to model the gastrocnemius muscle. However, no model investigates the temperature propagation in the muscle and describes its thermomechanical behavior on microstructure level.

Microstructural muscle models are essential to understand the mechanisms of heat and cold treatment of muscle tension and muscle injuries to reduce the pain.

To this end, we introduce a 3D thermomechanical multiscale continuum model for fascicles to study the influence of temperature propagation on the stress and strain development along a muscle fiber with a trigger point. Our two-phase fascicle model consisting of muscle fibers surrounded by endomysium allows to precisely investigate the mechanisms of heat and cold treatments in a tensed muscle fiber. Details regarding the influences of the trigger point and the neighboring fiber region to the relaxation of the entire fiber due heat and cold treatments are provided. A detailed understanding of the temperature influence on the mechanical response in tensed muscle fibers particularly provides information about its impact on relieving muscle tension and consequently on promoting the healing process.

5.3 Micro-thermomechanical model

An entire fascicle for a rat extensor digitorum longus (EDL) muscle is modeled with parallel oriented muscle fibers surrounded by the connective tissue endomysium (Fig. 5.2). The coupled thermomechanical analysis solves the heat equation

$$\rho_0 c_p \dot{T} = -\text{Div} \mathbf{Q} + \rho_0 r + T \frac{\partial [J \boldsymbol{\sigma} \cdot \mathbf{F}^{-T}]}{\partial T} : \dot{\mathbf{F}}, \quad (5.1)$$

and the balance of linear momentum

$$\rho_0 \ddot{\mathbf{u}} = \text{Div} (J \boldsymbol{\sigma} \cdot \mathbf{F}^{-T}) + \rho_0 \mathbf{b}, \quad (5.2)$$

simultaneously as the thermal behavior depends on the mechanical response and vice-versa. Here, ρ_0 denotes the material's density (in the reference configuration), c_p the specific heat capacity, T the temperature, t the time, \mathbf{Q} the heat flux vector, r the heat source, $J = \det \mathbf{F}$ the determinant of the deformation gradient \mathbf{F} , \mathbf{F}^{-T} the inverse of the transpose of the deformation gradient \mathbf{F} and $\boldsymbol{\sigma}$ the Cauchy stress tensor.

The thermoelastic coupling term $T \frac{\partial [J \boldsymbol{\sigma} \cdot \mathbf{F}^{-T}]}{\partial T} : \dot{\mathbf{F}}$ describes structural heating through elastic deformation. We neglect inelastic strains due to low strain rates and, thus, no self-heating is induced by plastic dissipation. The heat source r is zero because heat production in the fascicle, e.g. through electrochemical reactions during fiber activation, is negligible. Heating and cooling is applied via boundary conditions. The equation is discretized in time by the backward-difference method.

In the balance of linear momentum $\ddot{\mathbf{u}}$ is the acceleration vector and \mathbf{b} the specific body force vector. Inertia forces and body forces are neglected because they are much lower than the existing forces in fascicles⁹, thus, the balance of linear momentum reduces to its quasi-static

⁹Rough estimation reveals that the inertial force $\rho_0 \ddot{\mathbf{u}}$ in the trigger point of the muscle fiber is about 10^{10} times smaller than $\text{Div} (J \boldsymbol{\sigma} \cdot \mathbf{F}^{-T})$.

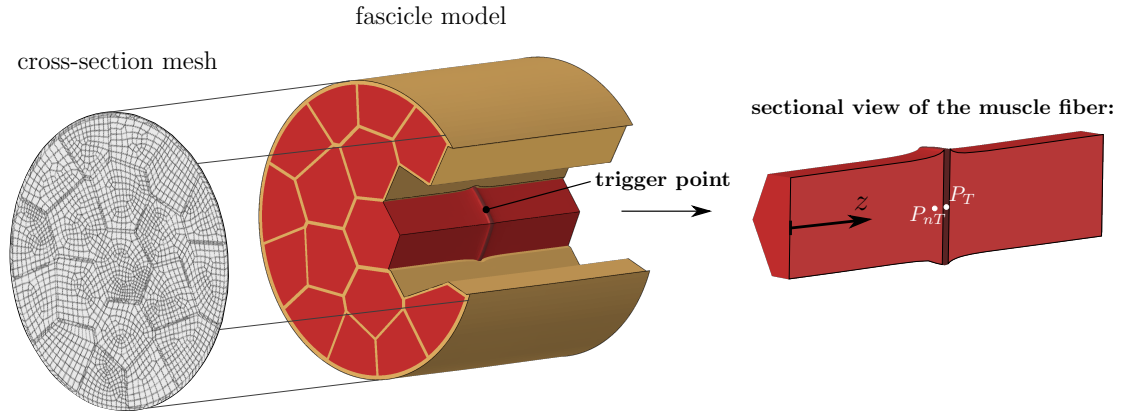


Figure 5.2: Computer model of a fascicle: 19 muscle fibers surrounded by endomysium. The central muscle fiber is permanently contracted in a thin region along the fiber which results in a compressed region forming a trigger point. Along the z -direction, the stress and strain values are evaluated in the central muscle fiber, for instance in the points P_T (trigger point) and P_{nT} (near the trigger point). The model is discretized with 141 960 linear reduced integrated hexahedral elements. The FE mesh of the cross-section is extruded along the fiber direction, with local mesh refinement ensuring good mesh quality in trigger points.

form

$$\mathbf{0} = \text{Div} (J\boldsymbol{\sigma} \cdot \mathbf{F}^{-T}). \quad (5.3)$$

The finite strain theory is applied because fascicles are subjected to large strains. In the following, we extend the elastic material models of our previous work [118] by including the thermo-mechanical behavior of muscle fibers and endomysium.

5.3.1 Endomysium

5.3.1.1 Endomysium: thermal constitutive equations

At resting muscle length, the collagen fibrils in the endomysium are randomly oriented and, thus, their distribution is assumed to be isotropic [23, 182, 214]. Thus, Fourier's law of heat conduction reads

$$\mathbf{Q}_{\text{endo}} = -k_{\text{endo}} \nabla T, \quad (5.4)$$

where k_{endo} represents the thermal conductivity, \mathbf{Q}_{endo} the heat flux density of the endomysium and ∇T the temperature gradient with respect to the material coordinates.

5.3.1.2 Endomysium: thermomechanical constitutive equations

The strain energy density function of endomysium Ψ_{endo} consists of a mechanical, thermomechanical and a thermal contribution:

$$\Psi_{\text{endo}} = \Psi_{\text{endo}_{\text{mech}}} + \Psi_{\text{endo}_{\text{thermomech}}} + \Psi_{\text{endo}_{\text{therm}}}. \quad (5.5)$$

The endomysium's highly nonlinear stress-strain behavior is described by the isotropic hyperelastic first order Ogden model¹⁰[45]

$$\begin{aligned} \Psi_{\text{endo}_{\text{mech}}} &= \frac{2\mu_{\text{endo}}}{\alpha_1^2} \left[\hat{\lambda}_1^{\alpha_1} + \hat{\lambda}_2^{\alpha_1} + \hat{\lambda}_3^{\alpha_1} - 3 \right] \\ &\quad + \frac{1}{2} \left[\lambda_{\text{endo}} + \frac{2\mu_{\text{endo}}}{3} \right] [J - 1]^2. \end{aligned} \quad (5.6)$$

The thermomechanical and thermal parts are given by

$$\Psi_{\text{endo}_{\text{thermomech}}} = -3 \left[\lambda_{\text{endo}} + \frac{2\mu_{\text{endo}}}{3} \right] \alpha_{\text{endo}} [T - T_0] [J - 1], \quad (5.7)$$

$$\Psi_{\text{endo}_{\text{therm}}} = c_{p_{\text{endo}}} \left[T - T_0 - T \ln \frac{T}{T_0} \right]. \quad (5.8)$$

λ_i are the principal stretches and $\hat{\lambda}_i = J^{-1/3} \lambda_i$ their distortional parts. λ_{endo} describes the first Lamé parameter, μ_{endo} the second Lamé parameter (i.e., the shear modulus) of endomysium and α_1 is a dimensionless constant of the Ogden model. α_{endo} denotes the thermal expansion coefficient and $c_{p_{\text{endo}}}$ the specific heat capacity of endomysium.

The Cauchy stress is derived from

$$\begin{aligned} \boldsymbol{\sigma}_{\text{endo}} &= \frac{2}{J} \mathbf{F} \cdot \frac{\partial \Psi_{\text{endo}}}{\partial \mathbf{C}} \cdot \mathbf{F}^T \\ &= \frac{2\mu_{\text{endo}} J^{-\frac{1}{3}\alpha_1 - 1}}{\alpha_1} \sum_{i=1}^3 \lambda_i^{\alpha_1} \left[\lambda_i^{-2} \mathbf{F} \cdot [\mathbf{e}_i \otimes \mathbf{e}_i] \cdot \mathbf{F}^T - \frac{1}{3} \mathbf{I} \right] \\ &\quad + \left[\lambda_{\text{endo}} + \frac{2\mu_{\text{endo}}}{3} \right] [J - 1] \mathbf{I} \\ &\quad - 3 \left[\lambda_{\text{endo}} + \frac{2\mu_{\text{endo}}}{3} \right] \alpha_{\text{endo}} [T - T_0] \mathbf{I}, \end{aligned} \quad (5.9)$$

where $\mathbf{C} = \mathbf{F}^T \cdot \mathbf{F}$ denotes the right Cauchy-Green tensor, \mathbf{F}^T the transpose of the deformation gradient \mathbf{F} and \mathbf{I} the second order identity tensor.

¹⁰Even at larger strains, there is still a substantial proportion of curvilinear collagen fibrils [214], thus, we assume an isotropic material behavior in our work.

5.3.2 Muscle fiber

5.3.2.1 Muscle fiber: thermal constitutive equations

Muscle fibers are assumed to be transversely isotropic. Thus, Fourier's law of heat conduction reads

$$\mathbf{Q}_{\text{fiber}} = \begin{bmatrix} -k_{x,\text{fiber}} & 0 & 0 \\ 0 & -k_{y,\text{fiber}} & 0 \\ 0 & 0 & -k_{z,\text{fiber}} \end{bmatrix} \cdot \nabla T, \quad (5.10)$$

where $k_{\bullet,\text{fiber}}$ are the thermal conductivities measured along x -, y - and z -direction, where the z -axis is parallel to the muscle fiber. $\mathbf{Q}_{\text{fiber}}$ is the heat flux density of the muscle fiber.

5.3.2.2 Muscle fiber: thermomechanical constitutive equations

A stretched and compressed muscle fiber exerts passive forces. If muscle fibers are electrically activated, the small contractile units, called sarcomeres, generate active forces by crossbridge cycling. The total Cauchy stress in muscle fibers is, thus, split into a passive and an active part [21, 87]

$$\boldsymbol{\sigma}_{\text{fiber}} = \boldsymbol{\sigma}_{\text{fiber}_{\text{pas}}} + \boldsymbol{\sigma}_{\text{fiber}_{\text{act}}}. \quad (5.11)$$

5.3.2.2.1 Passive behavior

The passive strain energy density function $\Psi_{\text{fiber}_{\text{pas}}}$ is split into a mechanical part $\Psi_{\text{fiber}_{\text{mech}}}$, a thermomechanical coupling $\Psi_{\text{fiber}_{\text{thermomech}}}$ and a thermal part $\Psi_{\text{fiber}_{\text{therm}}}$:

$$\Psi_{\text{fiber}_{\text{pas}}} = \Psi_{\text{fiber}_{\text{mech}}} + \Psi_{\text{fiber}_{\text{thermomech}}} + \Psi_{\text{fiber}_{\text{therm}}}, \quad (5.12)$$

$$\begin{aligned} \Psi_{\text{fiber}_{\text{mech}}} &= \frac{1}{2} \mu_{\text{fiber}} [\text{tr} \hat{\mathbf{C}} - 3] \\ &+ \frac{1}{2} \left[\lambda_{\text{fiber,Lamé}} + \frac{2\mu_{\text{fiber}}}{3} \right] [J - 1]^2, \end{aligned} \quad (5.13)$$

$$\Psi_{\text{fiber}_{\text{thermomech}}} = -3 \left[\lambda_{\text{fiber,Lamé}} + \frac{2\mu_{\text{fiber}}}{3} \right] \alpha_{\text{fiber}} [T - T_0] [J - 1], \quad (5.14)$$

$$\Psi_{\text{fiber}_{\text{therm}}} = c_{p\text{fiber}} \left[T - T_0 - T \ln \frac{T}{T_0} \right]. \quad (5.15)$$

The nearly-linear mechanical response of the muscle fiber observed by [138] in their experimental results is captured by the isotropic Neo-Hookean material model, which is used for muscle fibers in two-phase muscle models, see also [19, 203]. This hyperelastic model is characterized by the first Lamé parameter $\lambda_{\text{fiber,Lamé}}$ and the second Lamé parameter μ_{fiber} , respectively the fiber shear modulus. $\hat{\mathbf{C}} = J^{-2/3} \mathbf{C}$ is the distortional part of the right Cauchy-Green tensor. In the thermomechanical part, α_{fiber} denotes the thermal expansion coefficient of the fiber, $c_{p\text{fiber}}$ its specific heat capacity and T_0 the reference temperature.

Thus, the passive Cauchy stress tensor $\boldsymbol{\sigma}_{\text{fiberpas}}$ yields

$$\begin{aligned}\boldsymbol{\sigma}_{\text{fiberpas}} &= \frac{2}{J} \mathbf{F} \cdot \frac{\partial \Psi_{\text{fiberpas}}}{\partial \mathbf{C}} \cdot \mathbf{F}^T \\ &= \frac{\mu_{\text{fiber}}}{J} \left[\hat{\mathbf{B}} - \frac{1}{3} \text{tr}(\hat{\mathbf{B}}) \mathbf{I} \right] + \left[\lambda_{\text{fiber,Lamé}} + \frac{2\mu_{\text{fiber}}}{3} \right] [J - 1] \mathbf{I} \\ &\quad - 3 \left[\lambda_{\text{fiber,Lamé}} + \frac{2\mu_{\text{fiber}}}{3} \right] \alpha_{\text{fiber}} [T - T_0] \mathbf{I},\end{aligned}\quad (5.16)$$

where $\mathbf{B} = \mathbf{F} \cdot \mathbf{F}^T$ is the left Cauchy-Green tensor, $\hat{\mathbf{B}} = J^{-2/3} \mathbf{B}$ its distortional part and $\text{tr}(\hat{\mathbf{B}})$ the trace of $\hat{\mathbf{B}}$.

5.3.2.2.2 Active behavior

If muscle fibers are electrically activated, active stresses are generated in fiber direction. To account for this, the active part of the Cauchy stress tensor is extended (based on [119])

$$\boldsymbol{\sigma}_{\text{fiberact}} = \frac{P_{\text{max}35} P_{\text{max}35,\text{norm}}(T)}{J \lambda_{\text{fiber}}} \bar{\gamma} f(\lambda_{\text{fiber}}) \mathbf{a} \otimes \mathbf{a}. \quad (5.17)$$

$\bar{\gamma}$ represents the activation parameter, f the normalized force-length relation, which depends on the fiber stretch λ_{fiber} . $P_{\text{max}35}$ is the maximum isometric stress at 35° C [24], with 35° C being the reference temperature of rat muscles, and $P_{\text{max}35,\text{norm}}(T)$ is the temperature dependent maximum isometric stress normalized at 35° C. The current fiber direction in the deformed state is calculated via $\mathbf{a} = \mathbf{F} \cdot \mathbf{a}_0$, where \mathbf{a}_0 is the unit vector aligned in fiber direction in the reference configuration. The fiber stretch λ_{fiber} is determined by $\lambda_{\text{fiber}} = \sqrt{\text{tr}(\mathbf{C} \cdot [\mathbf{a}_0 \otimes \mathbf{a}_0])}$.

A fiber activation $\bar{\gamma} = 1$ indicates maximum activation and $\bar{\gamma} = 0$ a non-activated fiber. In this work, we assume a homogeneous degree of activation along the muscle fiber. The force-length relation characterizes the relationship between the sarcomere length and the generated force of a skeletal muscle fiber. Fibers exert maximum forces in the vicinity of the resting sarcomere length. The normalized force-length relation $f(\lambda_{\text{fiber}})$ from [240] describes this relationship and is formulated as a function of the fiber stretch λ_{fiber}

$$\begin{aligned}f(\lambda_{\text{fiber}}) = \max &\left(0.0015 \left[\frac{\lambda_{\text{fiber}} l_{s_0}}{l_{\text{norm}}} \right]^4 + 0.018 \left[\frac{\lambda_{\text{fiber}} l_{s_0}}{l_{\text{norm}}} \right]^3 \right. \\ &\left. - 0.935 \left[\frac{\lambda_{\text{fiber}} l_{s_0}}{l_{\text{norm}}} \right]^2 + 4.078 \frac{\lambda_{\text{fiber}} l_{s_0}}{l_{\text{norm}}} - 3.715; 0 \right),\end{aligned}\quad (5.18)$$

where the normalized length $l_{\text{norm}} = 1.0 \mu\text{m}$ creates consistent units and l_{s_0} denotes the resting sarcomere length. The current sarcomere length l_s is determined by the product of fiber stretch λ_{fiber} and the resting sarcomere length l_{s_0} .

The generated force of muscle fibers increases for higher temperatures. As opposed to stan-

standard materials, skeletal muscles have an outstanding maximum isometric stress-temperature curve (Fig. E.1). The unique maximum isometric stress-temperature dependence is described in Sect. E.2 (see also Fig. E.2). The force-producing crossbridge cycling is endothermic [233], thus, the generated force increases for higher muscle temperatures without increasing the number of attached crossbridges. The isometric stress-temperature-relationship can be fitted by the s-shaped sigmoidal curve, which is shown in [170],

$$P_{\max}(T) = 1 - \frac{1}{1 + e^{-\frac{\Delta H}{R} \left[\frac{1}{T} - \frac{1}{T_{0.5}} \right]}}, \quad (5.19)$$

where ΔH denotes the change in enthalpy between the non-force-producing and force-producing crossbridge states, $R = 8.314 \text{ J}/[\text{K mol}]$ the molar gas constant and $T_{0.5}$ the absolute temperature at 50% maximum isometric stress. The sigmoidal curve, which fits experimentally determined isometric stress-temperature values for the rat EDL muscle fiber from [172], is presented in Fig. E.1. As the maximum isometric stress at each temperature only scales the force-length relation [39, 55] (more information is provided in the Appendix and in Fig. E.2b), $P_{\max 35, \text{norm}}(T)$ is used as a factor in the active Cauchy stress tensor σ_{fiberact} (Eq. (5.17)).

The curves in Figs. E.1 - E.6 demonstrate the thermomechanical behavior of the entire fascicle model and its components. The material and geometrical data are summarized in the appendix.

5.4 3D computational model of fascicle

We generate¹¹ a computer model of a fascicle with a circular cross-section for a rat EDL muscle (Fig. 5.2) by using the Python codes from [120]. The model of the fascicle consists of 19 parallel aligned muscle fibers with polygonal cross-section embedded in the connective tissue endomysium, in line with experimental data [44]. By using Voronoi tessellation, fibers with irregular polygonal cross-section are generated. Our model includes randomly varying endomysium thicknesses between fibers to capture the variations of natural tissue.

The fiber volume fraction is chosen as 90%¹². Voronoi tessellation leads to slightly varying muscle fiber sizes with an average diameter of about 65 μm , in accordance with data for rat EDL muscles [177].

To minimize computational costs, we study a part of the entire fascicle and apply periodic boundary conditions in longitudinal direction. The influence of the surrounding connective tissue perimysium on the fascicle is neglected, since the mechanical behavior inside the fascicle is investigated. For the finite element simulations, the fascicle model is discretized with linear reduced integrated hexahedral elements with eight nodes per element. The muscle fibers and the endomysium share nodes at the interface and, thus, are perfectly bonded.

This work studies the mechanical influence of temperature on tensed muscle fibers on the fascicle level and focuses on the mechanisms of heat and cold treatment in trigger points. For

¹¹see [10] for a review on the generation of representative structures

¹²The volume fraction of 90% falls within the range identified in [129] for the entire muscle.

this purpose, the fascicle is heated or cooled on its surface, simulating the thermal treatment of trigger points by e.g. hot pack, sauna session, cold water immersion or cold pack.

To simulate a trigger point in the central muscle fiber, we assume a thin part of the fiber along the z -axis is permanently activated (activation $\bar{\gamma} = 1$, see Sect. 5.3.2.2.2) and to generate the same tension as in a tetanic contraction while the rest of the fiber is in a non-activated, passive state ($\bar{\gamma} = 0$). Thus, the fiber is compressed in the central region (Fig. 5.2) and stretched near the ends since the boundary conditions enforce a constant fascicle length.

With a reference temperature $T_0 = 35^\circ\text{C}$ [24] for the entire rat fascicle, the fascicle's surface is heated to $T = 38.8^\circ\text{C}$ as hot packs increase the fascicle's temperature by 3.8°C [47]. For cooled muscles, cold water immersion can result in muscle temperatures of approximately 30°C [174], thus, the fascicle's surface temperature is $T = 30^\circ\text{C}$ in this case. We assume that the observed fascicle temperatures after heating and cooling immediately appear on the fascicle surface at the beginning of the thermal treatment.

We distinguish between short-term (0.15 s) and long-term (20 min.) temperature treatment. For a short temperature treatment, we assume that temperature only influences the passive mechanical properties and does not affect the active behavior in the permanently contracted trigger points. Thus, the active stress in the contracted region remains constant. For a long-term treatment, the active tension in the trigger point decreases in the heated and cooled fascicles, which corresponds to in vivo behavior (Sect. 5.2). In this case, the muscle fiber model considers an electromyography (EMG) activity reduction of 15 % after 20 min. heat treatment and 23 % after 20 min. cold treatment, which is observed in injured muscles [162]. Therefore, the activation parameter in Eq. (5.17) is $\bar{\gamma} = 0.85$ after heating and $\bar{\gamma} = 0.77$ after cooling for the trigger point.

The thermal expansion coefficient of passive muscle fibers differs in active and rigor fibers. While passive fibers have a negative thermal expansion coefficient, the thermal expansion coefficient of active and rigor fibers is positive (see Sect. E.1.2 and Table E.2). For the trigger point, we use the same thermal expansion coefficient as for rigor fibers, since trigger points are also permanently contracted without nerve stimulation.

To verify the general validity of the model, the results of additional simulations with higher fiber volume fractions are presented in the supplementary material. These results show no differences to the ones presented in the following section.

5.5 Results: Computational modeling of thermomechanical behavior on the fascicle level

Heating or cooling the outer surface causes a heterogeneous temperature distribution in the fascicle. The heat/coldness propagates rapidly: most regions of the fascicle have already reached the applied surface temperature after 0.03 s (Fig. 5.3). After about 0.1 s, equilibrium temperature is reached in the fascicle (Fig. 5.3b and c). At the trigger point region, there are hardly any differences in the temperature-time curves, thus, a homogeneous temperature progression is

observed along the fascicle.

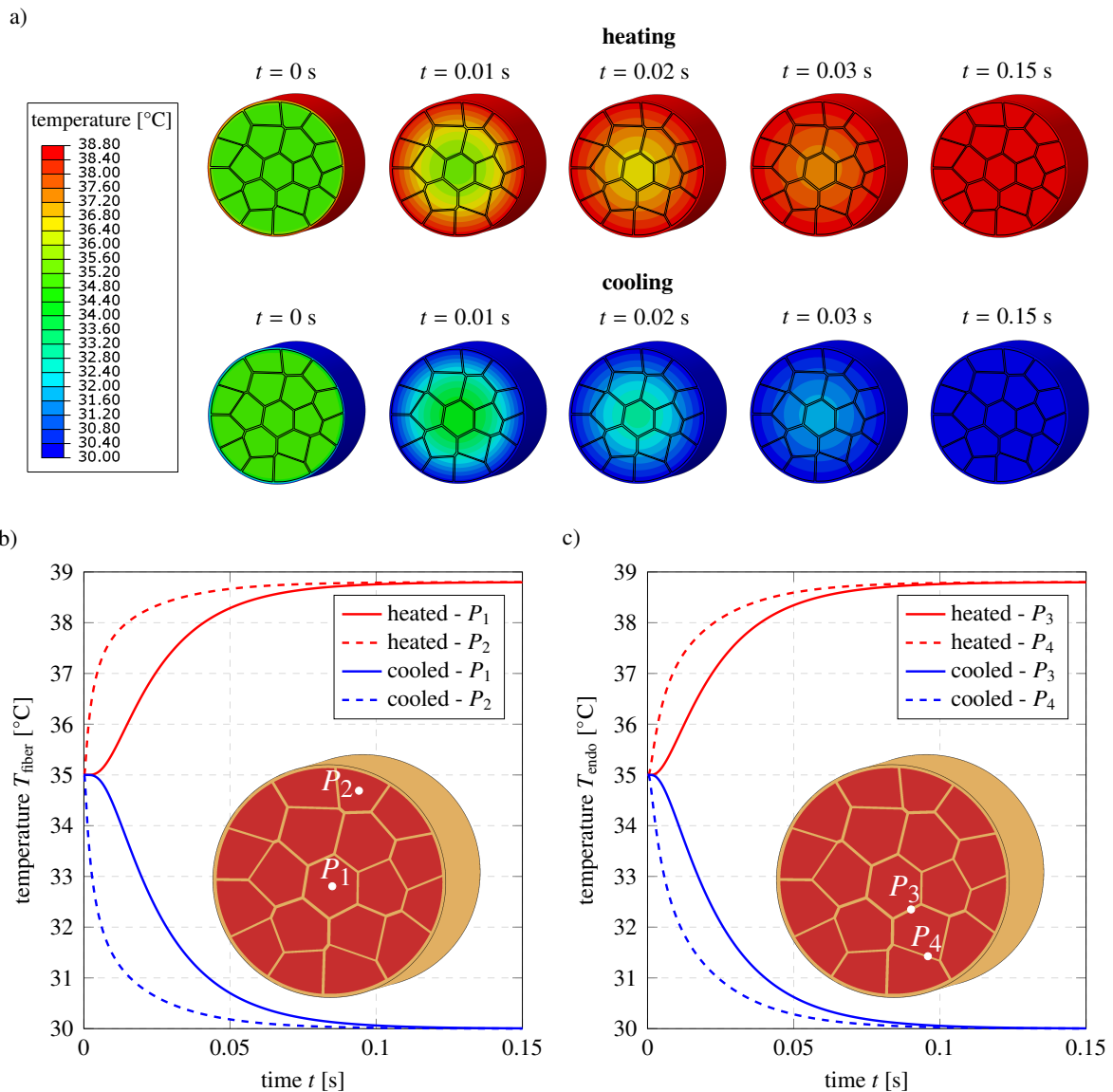


Figure 5.3: The fascicle has a reference temperature of 35°C and its outer surface is heated to 38.8°C or cooled to 30°C . a) The temperature distribution in the fascicle is depicted at different times. A fast relaxation is seen in both cases. b) and c): Temperature-time curves are exemplarily shown for two points in the muscle fibers (P_1 and P_2) as well as the endomysium (P_3 and P_4). The temperature equilibrates quickly. The fiber as well as the endomysium achieve the externally applied temperature after approximately $t = 0.1$ s.

In Fig. 5.4, the temperature influence on the mechanical behavior in the tensed central muscle fiber of the fascicle is investigated until $t = 0.15$ s (short-term treatment), thus, the active behavior in the trigger point is not affected by the temperature. The fiber contraction in the trigger point P_T before thermal treatment results in compressive strains and tensile stresses in this region. The total fiber tensile stress in the trigger point is due to the extremely high active tensile stress which is not fully compensated for by the passive compressive stress. Thus, the total stress

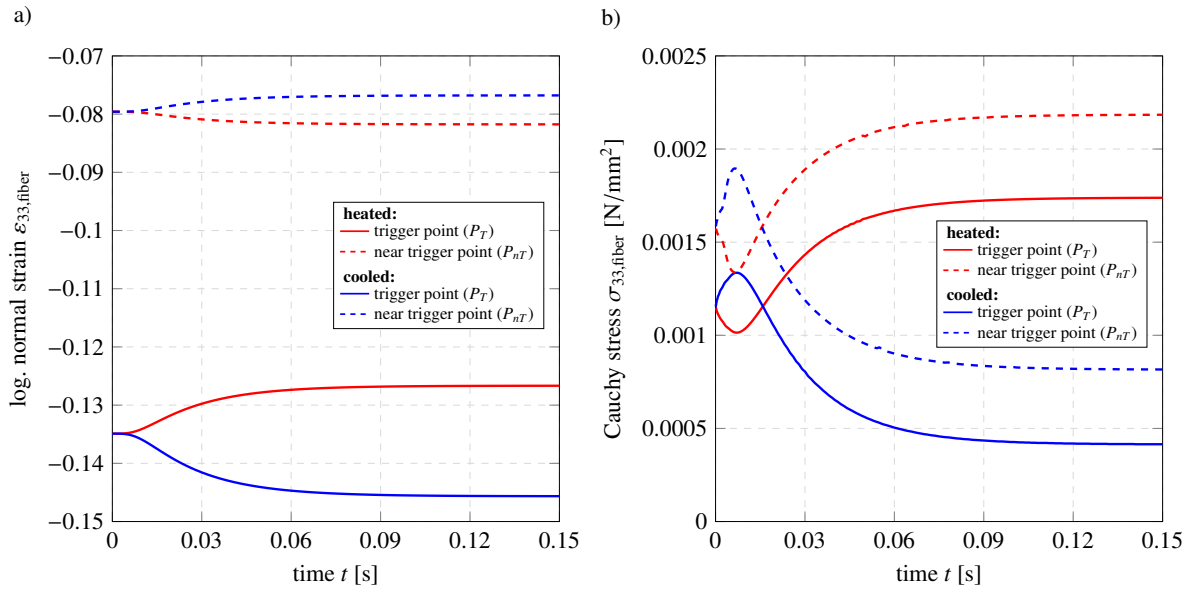


Figure 5.4: The progression of strains (a) and stresses (b) over time in the trigger point P_T and next to the trigger point P_{nT} are shown for fascicles heated to 38.8°C and fascicles cooled to 30°C. The strain and stress at $t = 0$ s (before thermal treatment) represent the values at reference temperature $T_0 = 35^\circ\text{C}$. a) The log. normal strain $\varepsilon_{33, \text{fiber}}$ in fiber direction increases for heating and decreases for cooling in the trigger point P_T and show the opposite behavior in the region P_{nT} next to the trigger point. b) Similar to the strains, the Cauchy stress $\sigma_{33, \text{fiber}}$ increases with higher temperature in the trigger point and decreases with lower temperature. The stresses next to the trigger point P_T exhibit the same behavior.

as the sum of the active and passive stresses results in a small tensile stress. In the passive adjacent fiber region, the Poisson's effect causes compression along the fiber direction despite the tensile stress.

Heating a tensed muscle fiber does not change the strains initially, as it takes time for the heat to reach the central muscle fiber. However, the stresses decrease because both regions are relieved by the increasing stresses in the warm surrounding fiber region. After $t = 0.01$ s, the temperature in the central muscle fiber increases, resulting in a reduction of the compressive strains in the trigger point but an increase of the compressive strains close to the trigger point (passive fiber region), as the thermal expansion coefficient is positive in rigor fibers and negative in passive fibers. The different absolute values of the thermal expansion coefficients of the two regions lead to thermal tensile stresses with temperature increase and, therefore, to an increase of the total stresses. When the temperature reaches its equilibrium value ($t = 0.1$ s), the strains and stresses remain constant. During cooling, the strains and stresses in both points show the inverse behavior compared to those during heating.

The strains and stresses in fiber direction before and after short-term (without EMG activity reduction) and long-term (EMG activity reduction is considered) thermal treatment are plotted along the center of the muscle fiber in Figs. 5.5 and 5.6, respectively. Figs. 5.5a and c show the strains in heated and cooled fascicles and Fig. 5.5b and d illustrate the strain difference which describes the subtraction between the strain at the end and the strain at the beginning of heat

and cold treatment.

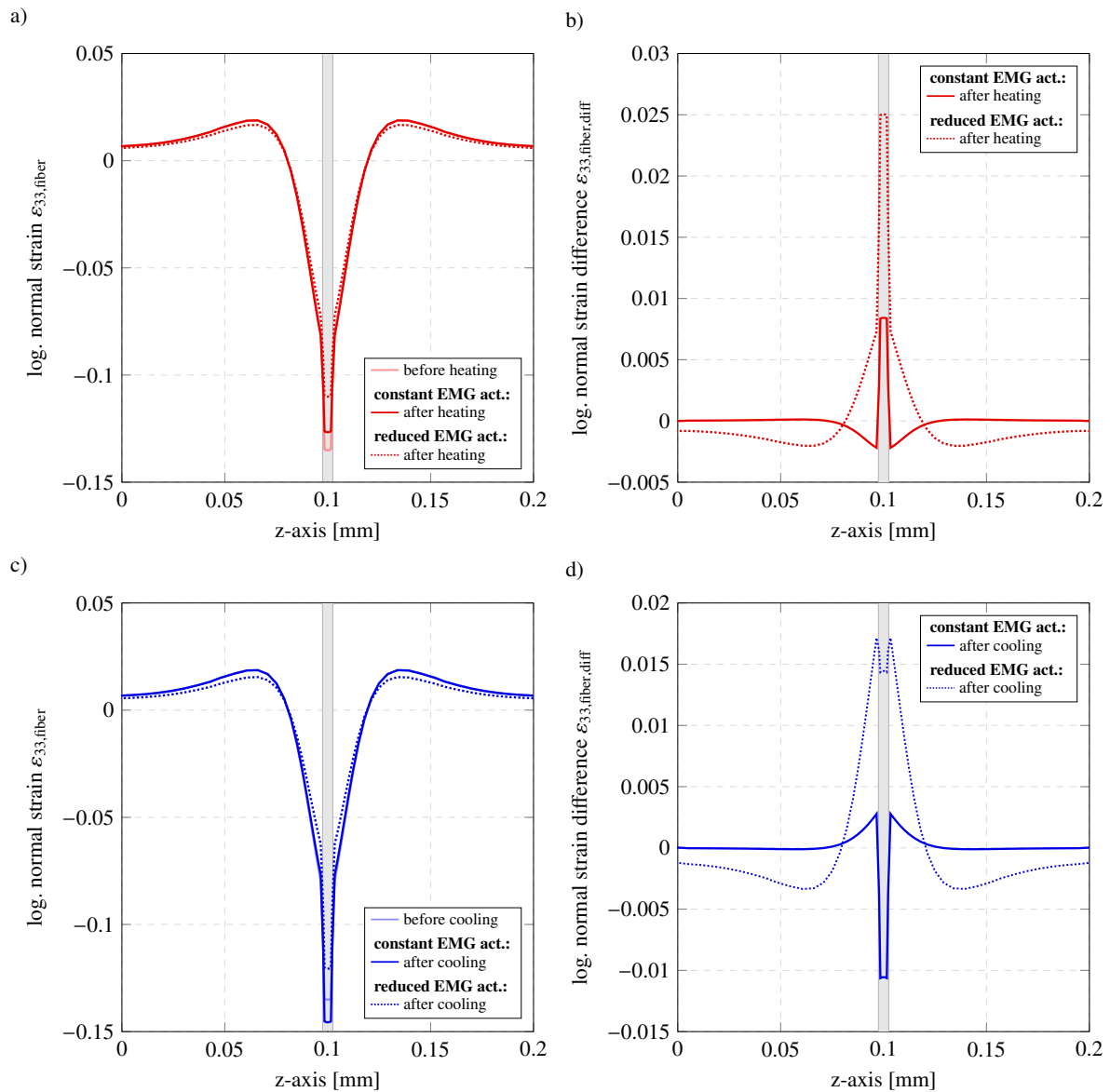


Figure 5.5: The strains along a tensed muscle fiber with a centrally located trigger point are depicted before and after heat and cold treatment of fascicles with constant and additionally reduced EMG activity. a) and c) show the log. normal strains in the fiber direction for heating and cooling and b) and d) present the strain difference (i.e., the difference between the strain at the end and the strain at the beginning of thermal treatment.) The region of the trigger point is illustrated by the gray region. a) and b): The high compressive strains in the trigger point are reduced in heated fascicles, even more if EMG activity reduction is also considered. The region near the trigger point is further compressed but relaxes if decreasing EMG activity is considered. c) and d): EMG activity reduction in cooled fascicles even reduces the compression in the trigger point, although further compression is observed for constant EMG activity. Furthermore, the compressed regions next to the trigger point relax more with decreasing than with constant EMG activity.

For a short-term treatment (constant EMG activity), heating/cooling results in reduction/increase of the compressive strain in the trigger point and compressive strain increase/reduction next to the trigger point, as already observed in Fig. 5.4. The tensile strains towards both fiber ends,

which compensate the compressive strains around the trigger point, are not affected by the temperature variations (Fig. 5.5b and d) since the boundary conditions reduce the effects at the fiber ends of the model.

For a long-term treatment (EMG activity reduction is considered), the compressive strains in the trigger point strongly decrease in heated fascicles. EMG activity strongly influences the region next to the trigger point causing its compressive strains to decrease as well, instead of increasing further. In cooled fascicles, EMG activity reduction also results in reduced compression in the trigger point although it shows the opposite behavior in the case of constant EMG activity. The strains next to the trigger point decrease even more than in the trigger point. Despite the stronger EMG activity reduction in the cooled case (23% after cooling compared to 15% after heating), the compressed region in the trigger point is more relaxed in the heated case. Outside the central region, the initially stretched fiber region is now affected by heat and cold treatment as the tensile strains are slightly reduced to compensate the strongly decreasing compression in and close to the trigger point.

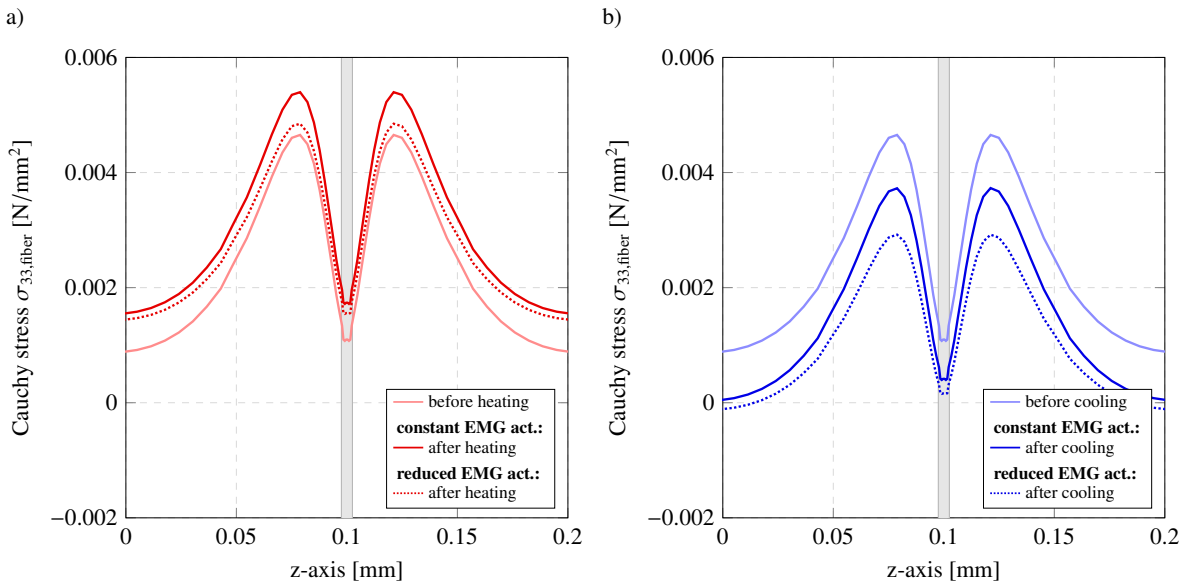


Figure 5.6: The Cauchy stresses in fiber direction are plotted along the tensed muscle fiber before and after heat and cold treatment without and with additionally considered EMG activity reduction. The gray area represents the region of the trigger point. For constant EMG activity, the low stresses along the fiber increase in heated fascicles and exhibit reverse behavior in cooled fascicles. Additional EMG activity reduction in heated fascicles results in a smaller stress increase than for constant EMG activity. For cooling, the stresses reduce even stronger with EMG activity reduction.

In a short-term treatment (constant EMG activity), the total Cauchy stresses increase along the entire fiber in heated fascicles (Fig. 5.6a), however, they drop in cooled fascicles (Fig. 5.6b). This is caused by the passive compressive stresses, which decrease with heating and increase with cooling (Fig. 5.7). In a long-term treatment (EMG activity reduction is considered), the passive compressive stress is reduced more during heating (Fig. 5.7). Since the active tensile stress decreases by EMG activity reduction, the total stress in the trigger point of heated fasci-

cles is lower than for short-term treatment (Fig. 5.6a). In cooled fascicles, EMG activity reduction causes further total stress drop in the tensed fiber (b). Despite the increase in passive compressive stress with constant EMG activity, the passive compressive stress strongly decreases with reduced EMG activity (Fig. 5.7). Since the active tensile stress is reduced for long-term cold treatment, compared to short-term treatment, the overall stress drops more in the trigger point. The strongest passive stress reduction occurs in long-term cooling, however, a stronger EMG activity reduction is assumed for cooling than for heating (Fig. 5.7).

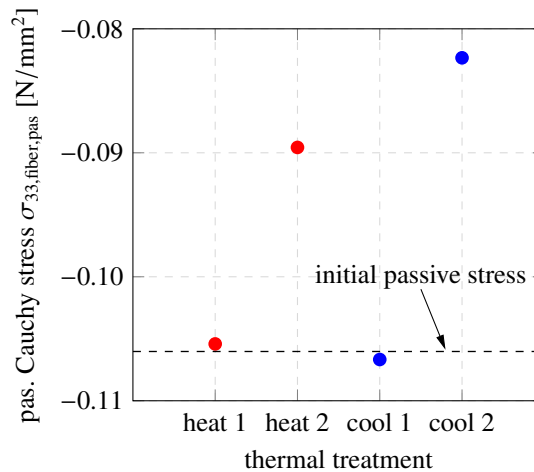


Figure 5.7: The passive Cauchy stress in fiber direction in the trigger point P_T after different thermal treatments is compared to the initial passive stress before treatment. After heat treatments, the passive Cauchy stress is reduced, however, after cooling, it is only reduced for decreasing EMG activity. Heat 1: short-term heating with constant EMG activity, heat 2: long-term heating with reduced EMG activity, cool 1: short-term cooling with constant EMG activity, cool 2: long-term cooling with reduced EMG activity.

5.6 Discussion

Short-term heating with constant EMG activity reduces the compressive strains in the trigger point. The adjacent fiber region supports the reduction of strains in the trigger points by further compression (Figs. 5.4a and 5.5b). The sign combination $-/+$ for the thermal expansion coefficients of the passive fiber region/rigor fiber region (trigger point) results in a maximum reduction of the strains in the trigger point (Fig. 5.8) because it leads to an expansion in the trigger point and a contraction in the passive adjacent fiber region - this optimal combination is exactly what is observed in tensed in vivo muscles.

Different thermal expansion coefficients result in thermal stresses that, in this case, lead to a reduction of passive stresses in the trigger point during heating (Fig. 5.7). This reduction is maximal for a $\alpha_{\text{fiber pas}}/\alpha_{\text{fiber rigor}}$ -combination of $-/+$ and $-/-$ (Fig. 5.8). The total tensile stress before heating is composed of strong passive compressive stresses due to contraction ($\approx -0.1056 \text{ N/mm}^2$) and slightly larger active tensile stresses ($\approx 0.1067 \text{ N/mm}^2$). Due to the larger absolute value of the thermal expansion coefficient in the passive adjacent fiber region,

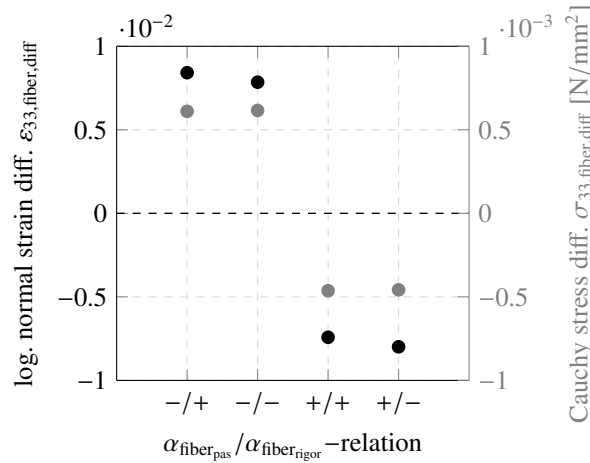


Figure 5.8: Log. normal strain difference and Cauchy stress difference in the trigger point P_T between the initial state ($t = 0$) and the state after short-term heating to 38.8°C are presented for various $\alpha_{\text{fiber_pas}}/\alpha_{\text{fiber_rigor}}$ -relations. The absolute value of the thermal expansion coefficients remain the same (as given in Table E.2) and only the sign varies. A negative passive thermal expansion coefficient $\alpha_{\text{fiber_pas}}$ results in a compressive strain reduction with a slightly larger difference for a positive $\alpha_{\text{fiber_rigor}}$ -value, however, the increase in tensile stress is nearly the same for a positive and negative $\alpha_{\text{fiber_rigor}}$ -value. A positive passive thermal expansion coefficient $\alpha_{\text{fiber_pas}}$ shows the opposite behavior with increasing compressive strains and reduced tensile stresses.

the compressive strains in the trigger point decrease stronger during heating which results in thermal tensile stresses in the trigger point (Fig. 5.8). They reduce the strong passive compressive stresses (Fig. 5.7) and, thus, relieve the muscle tension, which, however, results in slightly increased total tensile stresses due to the active tensile stresses (Figs. 5.4b and 5.6a).

In the passive adjacent fiber region, total tensile stresses occur before heating, however, the Poisson's effect causes a strong compression in fiber direction. Heating also slightly increases these stresses (Fig. 5.4b), since the adjacent passive fiber region is prevented from higher contractions due to the lower absolute value of the thermal expansion coefficient in the trigger point.

Short-term cooling with constant EMG activity does not reduce muscle tension. On the contrary, the compressive strains increase in the trigger point and are additionally supported by the adjacent expanding fiber regions (Figs. 5.4a and 5.5d). Thermal compressive stresses are generated in the adjacent fiber regions and in the trigger point, resulting in further increase of the passive compressive stresses in the trigger point (Fig. 5.7). This, however, leads to lower total tensile stresses (Figs. 5.4b and 5.6b).

Complete relaxation of the tensed muscle fiber is only achieved by reducing both passive and active stresses. The additional reduction of EMG activity during long-term thermal treatments strongly influences the relaxation of trigger points, which is supported by the entire muscle fiber. Reduced EMG activity softens the material in the trigger point. This relieves muscle tension during both heat and cold treatments.

The compressive strain reduction in the trigger point during heating is enhanced and during cooling, a reversed behavior is observed compared to a short-term treatment (constant EMG

activity), resulting in decreased compressive strains instead of further increased compressive strains (Fig. 5.5b and d). Although cooling causes a stronger reduction in EMG activity, the overall decrease in compressive strains in the trigger point is larger with heating (Fig. 5.5b and d). The stiffness reduction in the trigger point influences the behavior along the entire fiber, since, for long-term thermal treatments, the muscle fiber behaves similarly during heating and cooling (Fig. 5.5b and d). For both, the strongly varying strains along the fiber are reversed after treatment (Fig. 5.5a and c). Close to the trigger point, the compressive strains are strongly reduced, although for heating, an opposite behavior is expected due to the negative thermal expansion coefficient. This reduction of compressive strains in the trigger point and the adjacent region is compensated by a reduction of tensile strains in the rest fiber region. Thus, in the case of cooling, this region resists the expected expansion due to the negative thermal expansion coefficient.

Additional EMG activity reduction in long-term treatments not only decreases the active tensile stresses in the trigger point but also strongly reduces the passive compressive stresses after heating (Fig. 5.7). As the total stresses in the trigger point after treatment are higher compared to the initial state at $t = 0$ (Fig. 5.6a), the passive compressive stresses are more reduced than the active tensile stresses. Cooling also ensures a strong reduction of the passive compressive stresses in the trigger point, although for short-term treatments (constant EMG activity), the passive compressive stresses are even slightly increased (Fig. 5.7). Since, for cooling, the total stresses in the trigger point are significantly lower than in the initial state, the active tensile stresses are decreased stronger than the passive compressive stresses (Fig. 5.6b).

5.7 Conclusion

We developed a continuum thermomechanical model for EDL fascicles in which the thermomechanical behaviors of the muscle fiber and the endomysium are described in a two-phase model. A trigger point in the central muscle fiber and the influences of thermotherapy and cryotherapy on the tensed fiber are investigated.

Our results give new insights into the stress and strain development in the trigger point and in the adjacent fiber region during thermal treatments and the resulting relief of muscle tension in the fiber. We study short- and long-term heating and cooling and, therefore, EMG activity reduction in the trigger point.

In tensed fascicles, the thermomechanical muscle behavior facilitates the treatment of trigger points by short-term heating as the strong compressive strains and passive compressive stresses are reduced. For short-term cooling, on the other hand, compressive stresses and passive strains in the trigger point become worse. The sign combination $-/+$ of the thermal expansion coefficients $\alpha_{\text{fiber}_{\text{pas}}}/\alpha_{\text{fiber}_{\text{rigor}}}$ in tensed in vivo muscle fibers is in fact optimally suited for thermotherapy of trigger points, as it results in maximum relief of muscle tension and, thus, accelerates the healing process.

With the additional drop in EMG activity for long-term thermal treatment, the resulting reduction

in active stress and stiffness in the trigger point causes a significant decrease in compressive strains and passive compressive stresses in the trigger point, both during heating and cooling. EMG activity strongly influences the behavior in the trigger point but also along the entire fiber, therefore, the entire fiber facilitates the release of trigger points. Thus, trigger points can be treated by thermotherapy (which is in agreement with [183]), e.g. with hot packs or sauna sessions, but also by cryotherapy, e.g. with cold water immersion, despite the disadvantageous thermal expansion coefficient combination for cooling purposes.

This research underlines the immense benefit of thermal treatment: in addition to its simple application without professional assistance, no risk is related to the choice between thermotherapy and cryotherapy of trigger points.

A | Appendix of article 1

A set of representative output-files (.jnl) for each hierarchical level is included in the codes. These can directly be used in Abaqus. The following input values were used to obtain these output-files:

Level 1 (hexagonal sarcomere cross-section) - *sarcomere_hex.jnl*:

cross_section = "hex", r_myosin = 0.006 [μm], l_myosin = 1.6 [μm], r_actin = 0.003 [μm], l_actin = 1.0 [μm], thickness_z_disc = 0.05 [μm], l_sarcomere = 2.5 [μm], l_crossbridge = 0.02 [μm], number_crossbridges = 600

Level 1 (circular sarcomere cross-section) - *sarcomere_cir.jnl*:

cross_section = "cir", r_myosin = 0.006 [μm], l_myosin = 1.6 [μm], r_actin = 0.003 [μm], l_actin = 1.0 [μm], thickness_z_disc = 0.05 [μm], l_sarcomere = 2.5 [μm], l_crossbridge = 0.02 [μm], number_crossbridges = 600

Level 2 - *myofibril.jnl*:

l_sarcomere = 2.5 [μm], number_sarcomeres = 10, r_unit_cell = 0.03 [μm], number_unit_cells_per_sarcomere = 1000

Level 3 - *musclefiber.jnl*:

number_myofibrils = 100, vf_myofibril = 80 [%], vf_sarcoplasmic_reticulum = 15 [%], vf_sarcolemma = 5 [%], r_muscle_fiber = 30 [μm], l_muscle_fiber = 60 [μm]

Level 4 - *fascicle.jnl*:

number_muscle_fibers = 60, vf_muscle_fiber = 90 [%], r_fascicle = 250 [μm], l_fascicle = 500 [μm]

Level 5 - *muscle.jnl*:

number_fascicles = 20, vf_fascicle = 80 [%], vf_perimysium = 10 [%], vf_epimysium = 5 [%], vf_fascia = 5 [%], r_muscle = 2000 [μm], l_muscle = 4000 [μm]

B | Appendix of article 2

B.1 Chemoelectrical part of muscle fiber material model

The activation parameter $\gamma(t, f_s, \dot{l}_s)$ along the fiber is calculated via

$$\gamma(t, f_s, \dot{l}_s) = \frac{F_{hs}(t, f_s, \dot{l}_s) - F_{hs}(t, 0, 0)}{F_{hs_{\max}}(t, f_{s_{\max}}, 0) - F_{hs}(t, 0, 0)}, \quad (\text{B.1})$$

based on [88]. Here, F_{hs} is the generated force of a half-sarcomere in different states. $F_{hs}(t, 0, 0)$ denotes the half-sarcomere force at zero activation and for an isometric contraction.

$F_{hs_{\max}}(t, f_{s_{\max}}, 0)$ indicates the force for a maximum stimulation in the same isometric state. A maximum stimulation called tetanic stimulation is reached for a stimulation frequency of $f_{s_{\max}} = 100$ Hz. In this case, a motor unit is maximally stimulated by its motor neuron such that action potentials are emitted at a very high rate.

The half-sarcomere force F_{hs} at a given position and time t is calculated by

$$F_{hs}(t, f_s, \dot{l}_s) = \eta A_1(t, f_s) x_1(t, f_s, \dot{l}_s) + \eta A_2(t, f_s) x_2(t, f_s, \dot{l}_s), \quad (\text{B.2})$$

following [173]. Eq. (B.2) describes the force resulting from the crossbridge dynamics in a contraction process. A_1 indicates the number of crossbridges in the pre-power stroke state in which the crossbridges only attach to actin. The number of crossbridges in the post-power stroke state A_2 represents the state after force generation resulting in rotation of the crossbridges. Considering a non-isometric contraction, x_1 describes the average distortion on the crossbridges in state A_1 and x_2 specifies the average distortion in the A_2 state. $\eta = 4 \cdot 10^{-4} - 7 \cdot 10^{-4}$ N/m is the elastic stiffness coefficient of a single crossbridge [32].

The distortions x_1 and x_2 caused by filament sliding of actin and myosin [32] are obtained from

$$\frac{\partial x_1}{\partial t} = - \left[f_0 \frac{D_2}{A_1} + h' \frac{A_2}{A_1} \right] x_1 + h' \frac{A_2}{A_1} [x_2 - x_0] + \frac{\dot{l}_s}{2}, \quad (\text{B.3a})$$

$$\frac{\partial x_2}{\partial t} = -h_0 \frac{A_1}{A_2} [x_2 - [x_1 + x_0]] + \frac{\dot{l}_s}{2}. \quad (\text{B.3b})$$

In an isometric contraction, x_0 is the average distortion in the post-power stroke state A_2 . The

values for the constants $h' = 0.18$ and $h_0 = 0.24$ are taken from [199]. The differential equations for calculating the number of crossbridges in the attached states A_1 , A_2 and detached state D_2 are listed in Shorten et al. [199] as well as the function f_0 .

We apply the one-dimensional approach of [88] to a three-dimensional setting in the following way: The activation parameter $\gamma(t, f_s, \dot{l}_s)$ is first determined for any position along a one-dimensional muscle fiber. Subsequently, $\gamma(t, f_s, \dot{l}_s)$ at each node of the one-dimensional mesh is transferred by linear interpolation to the nodes of a three-dimensional extended mesh to obtain $\bar{\gamma}(t, f_s, \dot{l}_s)$.

Electrophysiological properties of biological tissues are generally described by the three-dimensional bidomain equations representing reaction-diffusion equations [164]. As there is no electrical activation from fibers to adjacent ones, we can reduce these equations to the one-dimensional monodomain equation [87]

$$\frac{\partial}{\partial s} \left[\sigma_c \frac{\partial V_m}{\partial s} \right] = A_m \left[C_m \frac{\partial V_m}{\partial t} + I_{\text{ion}} \right]. \quad (\text{B.4})$$

Furthermore, the electrical conductivity of the muscle parallel to the fiber direction is about ten times higher than transverse to the fiber direction [57]. The spatial variable s describes the position along the fiber, σ_c the conductivity, V_m the membrane voltage, A_m the ratio of membrane surface to volume and C_m represents the capacity of the cell membrane per unit area. Furthermore, I_{ion} denotes a nonlinear function for the transmembrane ionic current. To solve this equation, the first order accurate Godunov-type splitting technique [76] is applied, which separates the nonlinear reaction term from the diffusion term [87]:

$$\frac{V_m^* - V_m^k}{\Delta t} = -\frac{1}{C_m} I_{\text{ion}}(V_m^k) \quad (\text{reaction term}), \quad (\text{B.5a})$$

$$\frac{V_m^{k+1} - V_m^*}{\Delta t} = \frac{1}{A_m C_m} \frac{\partial}{\partial s} \left[\sigma_c \frac{\partial V_m^{k+1}}{\partial s} \right] \quad (\text{diffusion term}), \quad (\text{B.5b})$$

where k denotes the old time step, \star the intermediate value and $k + 1$ the current time step. To calculate the membrane voltage V_m^* in Eq. (B.5a) for each time increment Δt at a given point of the fiber, the extensive half-sarcomere model of Shorten et al. [199] is used which describes the force development in different muscle fibers using mathematical descriptions of the complex electrophysiological, subcellular processes taking place between excitation and contraction of the fiber. The model is divided into several parts including membrane electrophysiology, calcium release from sarcoplasmic reticulum, calcium and crossbridge dynamics and fatigue based on phosphate dynamics. The model employs parameters for slow-twitch (type-I) and fast-twitch (type-II) fibers of the mouse soleus and the extensor digitorum longus muscle to show the difference in their activation process. This model uses multiple ordinary differential equations which are solved numerically by the explicit Runge-Kutta-Fehlberg method to calculate the membrane voltage V_m^* during electrical stimulation.

An electrical activation results in an action potential in the middle of the muscle fiber spreading

along the fiber. This propagation is described by the diffusion equation (B.5b). The diffusion term is solved with the finite element method in space and the implicit backward Euler method in time. The reaction and diffusion terms interact with each other so that the temporal as well as the spatial change of the membrane voltage is considered. First, the reaction term is solved to obtain the intermediate result V_m^* and second, its value is used to calculate V_m^{k+1} in the diffusion term which represents the membrane voltage for the next time step. To determine the unknown quantities from Eqs. (B.3a) and (B.3b) which depend on the calculated value for the membrane voltage further differential equations of the extensive half-sarcomere model [199] are used. For a more detailed description how to solve the extensive package of differential equations and how they interact during simulation, see Heidlauf et al. [87] and Shorten et al. [199].

B.2 Further simulation results

B.2.1 Influence of the activation parameter $\bar{\gamma}$ on the stress-strain curve of fascicles

To determine the 1. Piola-Kirchhoff stress–fiber stretch relationship for fascicles for different electrically activated muscle fibers, the activation parameter $\bar{\gamma}$ is varied and the entire fascicle curve is determined by compression and tensile tests, see Fig. B.1. The results show that the stress–fiber stretch behavior continuously flattens for smaller $\bar{\gamma}$ -values. This is due to the fact that the active stresses in the fibers decrease and, thus, the influence of the passive properties of muscle fiber and endomysium on the entire behavior increases.

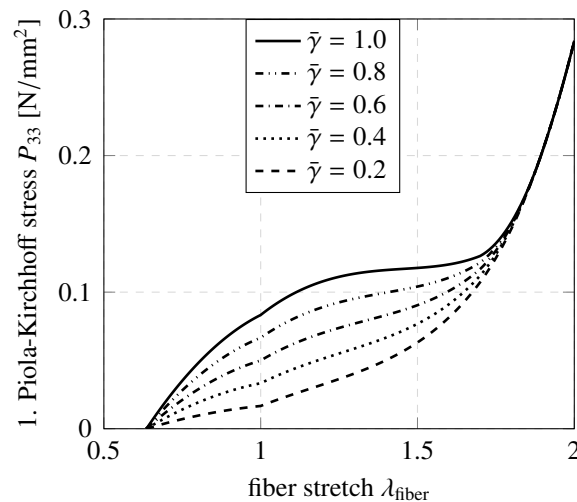


Figure B.1: 1. Piola-Kirchhoff stress–fiber stretch relationship for fascicle with various activation levels $\bar{\gamma}$ for muscle fibers.

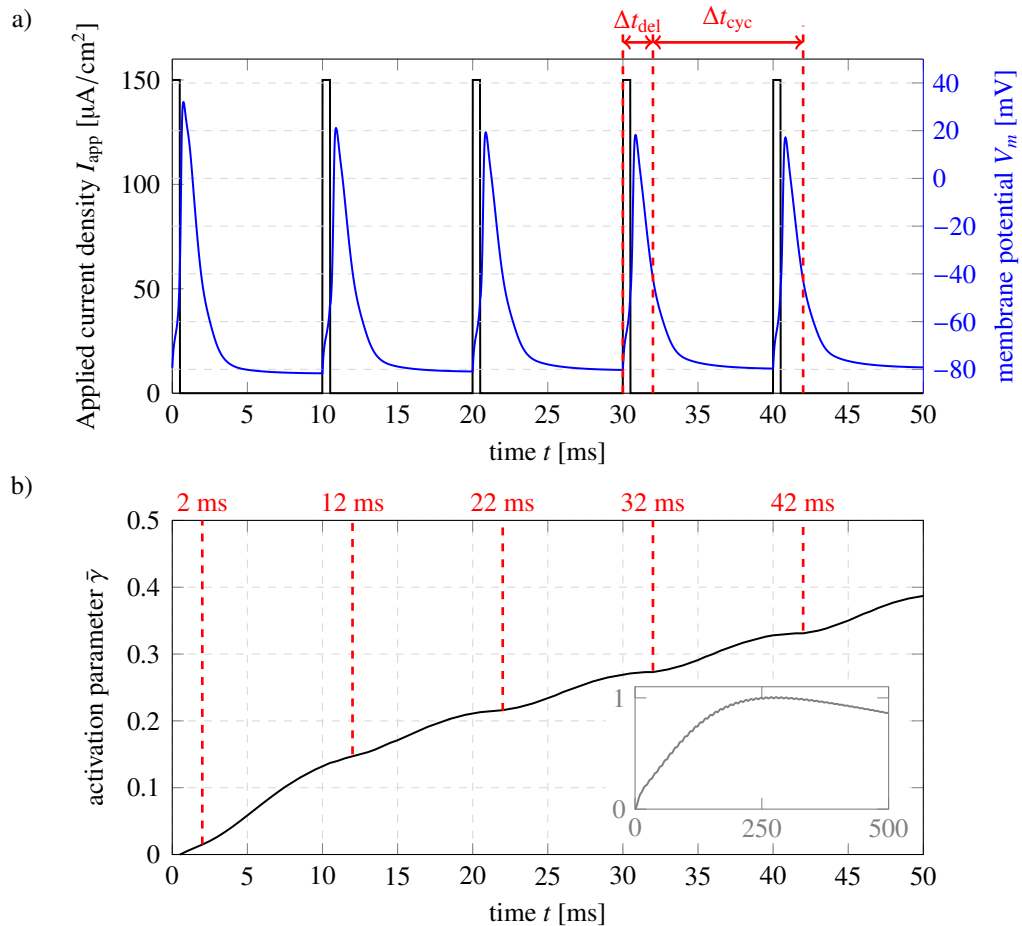


Figure B.2: Chemoelectrical processes in electrically activated fascicles and the associated temporal changes in the activation level of muscle fibers. a) The applied current density with an excitation frequency of 100 Hz as well as the membrane potential in the middle of the fiber are plotted over time. Activation causes an immediate short-term increase in the membrane potential that gradually decreases over a cycle. In b) the value of the activation parameter is plotted over the entire activation time of 500 ms and over a shorter time period where a delayed response to an activation impulse is observed.

B.2.2 Interaction of chemoelectrical processes and mechanical processes during fiber activation

The chemoelectrical processes in electrically activated muscle fibers lead to the stress distributions in an activation cycle (Fig. 3.9a). An activation with an electrical current density of $150 \mu\text{A}/\text{cm}^2$ and a frequency of 100 Hz causes an immediate short-term increase in the membrane potential V_m in the middle of the muscle fibers (see Fig. B.2a). Furthermore, the maximum membrane potential V_m decreases over time (Fig. B.2a). The membrane potential V_m initiated in the middle of the fiber propagates along the muscle fiber and influences the degree of activation $\bar{\gamma}$ in the middle of the fiber (see Fig. B.2b) as well as along the fiber. This is also demonstrated by the stress distributions for an activation cycle in Fig. 3.9a. Due to the transport and binding of Ca^{2+} as well as the activation of the crossbridges for rotation, the force generation in sarcomeres is

delayed [199]. This delay also affects the higher levels of hierarchy and is well captured by our model: in the contractile response a delay of about $\Delta t_{\text{delay}} = 2 \text{ ms}$ is visible.

B.2.3 Total fascicle RVE force in fascicles with varying states of stretch and compression depending on the speed of contraction

The generated muscle fiber force depends on the sarcomere length as well as the speed of contraction due to the viscoelastic properties of skeletal muscle fibers (Fig. 3.2). The electrochemical model can map the latter, i.e., the force-velocity relation of muscle fibers [88]. We study its influence on the total forces, including passive and active force components. Therefore, we correlate points on the force-velocity curve with the resulting total forces at different lengths.

Fascicles with varied stretch ($\lambda_{\text{fiber}} = 0.75$, $\lambda_{\text{fiber}} = 1.0$, $\lambda_{\text{fiber}} = 1.25$) are isometrically contracted (fascicles are tensed) until they generate the maximum force ($t = 250 \text{ ms}$). At $t = 250 \text{ ms}$, concentric and eccentric contractions of different velocities are performed and the total

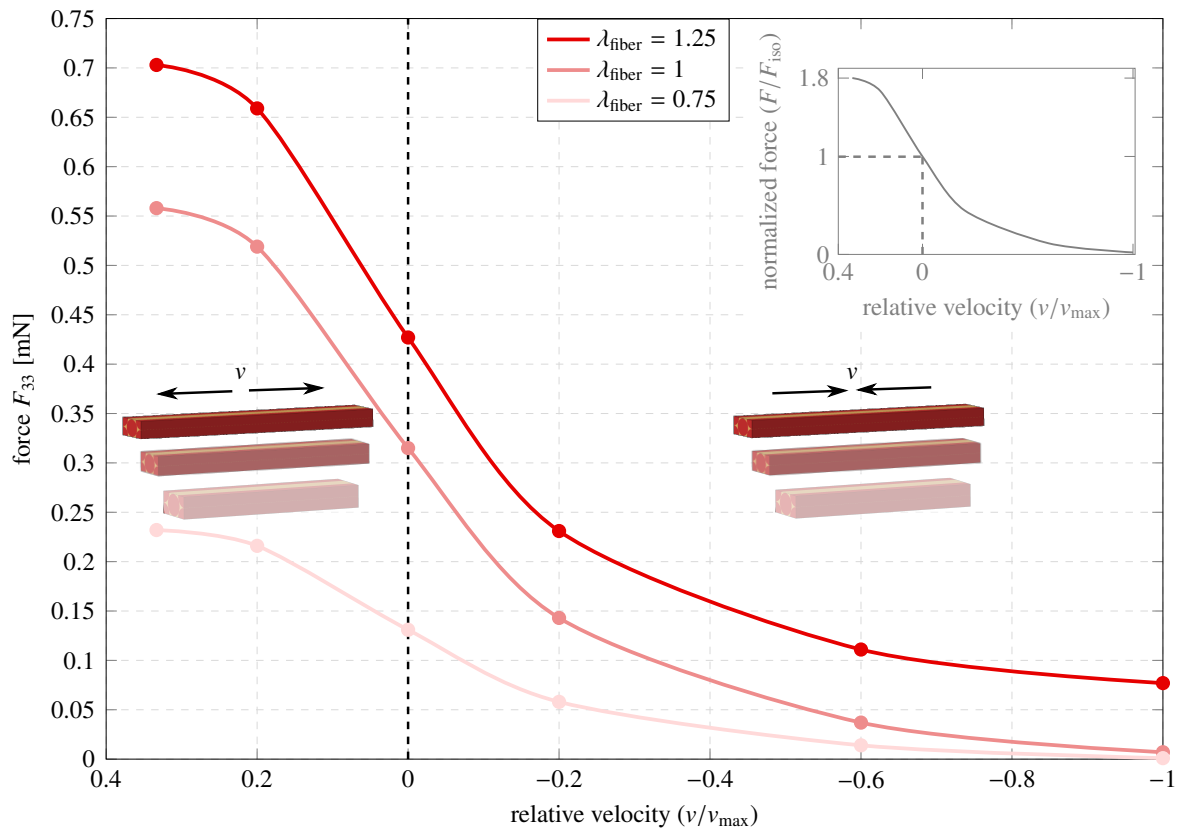


Figure B.3: Force vs. relative velocity in fully activated fascicle RVEs of the EDL muscle ($\lambda_{\text{fiber}} = 0.75$, $\lambda_{\text{fiber}} = 1.0$ and $\lambda_{\text{fiber}} = 1.25$). Additionally, the normalized force-velocity relationship of EDL muscle fibers is presented to demonstrate the influence of the velocity on the generated maximum force in muscle fibers normalized by the maximum value for an isometric contraction.

forces in the fascicle are determined directly for maximally stimulated muscle fibers ($\bar{\gamma} = 1$) at $t = 250$ ms. In Fig. B.3, the fascicle forces are plotted over the relative velocity, that is the velocity normalized by the maximum compression speed. The results for different velocities are marked by dots in Fig. B.3. In the inset graph, the forces of EDL muscle fibers for different contraction speeds are normalized by the force that can be generated in an isometric contraction. In our simulations, the normalized force-velocity curve only affects the active part of the muscle fibers.

The maximum normalized force value of 1.8 predicted for high eccentric contractions is in agreement with experimental studies in [8, 9, 51] which have measured maximum normalized force values close to 1.8. The trend of the force-velocity relation (inset graph) can also be observed in the three force-velocity curves of the fascicles with the S-shape becoming more pronounced for longer fascicles.

Generally, due to the force-length relation, the generated force and stress is maximal at $\lambda_{\text{fiber}} = 1.25$. As the forces are determined for maximally activated muscle fibers at $t = 250$ ms, the forces at contraction velocity $v = 0$ correspond to the values in Fig. 3.8b. With increasing concentric contraction speed, the generated force is significantly reduced. For maximum shortening velocity, the generated force in muscle fibers is approximately zero. The difference in the force values at this point is only caused by the passive forces in fascicles. In contrast, the exerted force in fibers increases for higher stretching velocities. The stretching speed generating the maximum force results in a multiplication of the force generated in isometric contractions by approximately 1.8 for fascicles stretched by $\lambda_{\text{fiber}} = 0.75$ and $\lambda_{\text{fiber}} = 1.0$. For $\lambda_{\text{fiber}} = 1.25$ passive forces are involved, but they are not influenced by the force-velocity relation, so that the factor is lower than 1.8.

The high forces and stresses resulting in fast eccentric movements lead to higher injury risk in skeletal muscles. For this reason, eccentric contractions during strength training need to be performed slowly and controlledly.

C | Appendix of article 3

C.1 Material Data

Tables C.1 and C.2 summarize the material and geometrical data used in the model. In the following, more detail on the choices and material modeling is given for each component.

C.1.1 Muscle fiber

C.1.1.1 Elastic parameters

The EDL fiber Young's modulus of 0.175 N/mm^2 is taken from experimental results [139]. Since the fiber's behavior is nearly incompressible, a Poisson's ratio of $\nu_{\text{fiber}} = 0.4999$ is chosen. Based on these values, the shear modulus μ_{fiber} and the bulk modulus κ_{fiber} can be calculated to be $\mu_{\text{fiber}} = 0.058 \text{ N/mm}^2$ and $\kappa_{\text{fiber}} = 291.7 \text{ N/mm}^2$.

The maximum isometric active stress in EDL muscle fibers $P_{\text{max}} = 0.107 \text{ N/mm}^2$ is obtained from the experimental data on wild-type mice [189]. Here, the median of the maximum muscle fiber forces is divided by the median of the cross sectional area of the fibers. For the activated state, we assume fully activated muscle fibers with a constant activation level of $\bar{\gamma} = 1.0$ along the entire fiber length.

C.1.1.2 Johnson-Cook model parameters for passive loading

Several studies [6, 27, 139] find reversible material behavior of a passively loaded muscle fiber for strains up to approximately 50%. Therefore, a simulation with a tensile loaded muscle fiber is performed using the Neo-Hookean material model of the fiber (see Sect. 4.3.1.1.1) to determine the passive yield stress $A_{\text{pas}} = 0.0924 \text{ N/mm}^2$ as the stress at a deformation of $\lambda_{\text{fiber}} = 1.5$.

Since detailed information about the stress-strain behavior for large deformations are missing for passive EDL muscle fibers, we use the tensile stress-strain behavior of raw porcine longissimus thoracis muscle fibers to failure [142] as reference. With a passive yield stress of $A_{\text{pas}}(\lambda_{\text{fiber}} = 1.5) = 0.0924 \text{ N/mm}^2$ and passive rupture stress of $\sigma_{\text{r,pas}} = 0.13 \text{ N/mm}^2$ [189] at a fiber stretch of about $\lambda_{\text{fiber}} = 1.75$ [189, 193]¹³ for EDL muscle fibers, the curve of [142] was fitted with the Johnson-Cook model. The parameters are determined, as described in [141], and

¹³Information from a private communication with the authors of [189].

Parameter	Value	Definition
E_{fiber}	0.175 N/mm ² [139]	fiber Young's modulus
μ_{fiber}	0.058 N/mm ²	fiber shear modulus
ν_{fiber}	0.4999	fiber Poisson's ratio
κ_{fiber}	291.7 N/mm ²	fiber bulk modulus
P_{max}	0.107 N/mm ² [189]	fiber maximum isometric stress
$\bar{\gamma}$	1.0	fiber activation parameter
l_{s0}	2.0 μm	resting sarcomere length
l_{norm}	1.0 μm	quantity to normalize the force-length relation
d_{fiber}	47.5 μm [189]	fiber diameter
φ_{fiber}	0.9	fiber volume fraction
h_1	3.2	constant for additional titin stress
h_2	4.6	constant for additional titin stress
h_3	-0.5	constant for additional titin stress
$\varepsilon_{\text{shift}}$	0.11 [34]	shift coefficient for additional titin stress
A_{pas}	0.0924 N/mm ²	passive fiber yield stress
A_{act}	0.1698 N/mm ²	active fiber yield stress
B	0.385	Johnson Cook strain hardening constant
n	0.739	Johnson Cook strain hardening coefficient
β	100	exponential damage parameter
$\lambda_{\text{fiber}_{\text{min}}}$	1.75	fiber stretch leads to myofibrillar failure
$\lambda_{\text{fiber}_{\text{max}}}$	1.8	fiber stretch leads to final rupture

Table C.1: Material and geometrical data of the EDL muscle fiber

we obtain $B = 0.385$ for the strain hardening constant and $n = 0.739$ for the strain hardening coefficient.

C.1.1.3 Johnson-Cook model parameters for active loading

In active muscle fibers, fiber damage occurs already at lower strains. If the muscle fiber is actively stretched (eccentric contraction) damage is first initiated at a fiber stretch of $\lambda_{\text{fiber}} = 1.1457$ [84]. The Johnson-Cook model is used starting from this fiber stretch. For an actively stretched fiber, the active yield stress $A_{\text{act}} = 0.1698 \text{ N/mm}^2$ is determined from an initial simulation at a fiber stretch of $\lambda_{\text{fiber}} = 1.1457$. Due to lack of information about the damage behavior of activated EDL muscle fibers, we assume the same Johnson-Cook parameters $B = 0.385$ and $n = 0.739$ as for the passive loading case.

C.1.1.4 Damage model parameters

Activated and nonactivated muscle fibers achieve the same fiber stretch until total fiber rupture although fiber damage starts earlier in activated fibers [28, 73]. Therefore, we choose the same fiber stretches for myofibrillar failure $\lambda_{\text{fiber,min}}$ and for total fiber rupture $\lambda_{\text{fiber,max}}$ as well as the same exponential damage parameter β for passive and active muscle fibers.

The fiber fails at a fiber stretch of $\lambda_{\text{fiber}} = 1.75$. We assume the maximum fiber stress to occur at this fiber stretch. Thus, this value is chosen as the starting point for the collective failure of myofibrils $\lambda_{\text{fiber,min}}$. For the immediate total failure, we select an exponential damage parameter of $\beta = 100$ and a fiber stretch at complete fiber rupture of $\lambda_{\text{fiber,max}} = 1.8$.

C.1.2 Connective tissue endomysium

The Young's modulus of endomysium is $E_{\text{endo}} = 0.2415 \text{ N/mm}^2$ [118]. With a Poisson's ratio of $\nu_{\text{endo}} = 0.4999$ for nearly incompressible material behavior, a bulk modulus of $\kappa_{\text{endo}} = 402.5 \text{ N/mm}^2$ and a shear modulus of $\mu_{\text{endo}} = 0.08 \text{ N/mm}^2$ are calculated and the constant $\alpha_1 = 7.95$ is used in the Ogden model [118].

Parameter	Value	Definition
E_{endo}	0.2415 N/mm^2	endomysium Young's modulus
μ_{endo}	0.08 N/mm^2	endomysium shear modulus
ν_{endo}	0.4999	endomysium Poisson's ratio
κ_{endo}	402.5 N/mm^2	endomysium bulk modulus
α_1	7.95	constant of the Ogden model used for endomysium
φ_{endo}	0.1	endomysium volume fraction

Table C.2: Material and geometrical data of the endomysium

C.2 Further simulation results

C.2.1 Damage behavior and injury of muscle fibers loaded in fiber direction

Tensile tests are modeled on an isolated EDL muscle fiber in fiber direction to predict its material behavior until total fiber rupture for the activated (eccentric contraction) and non-activated (passive) state. Compared to the passive state, the active Cauchy stress (Eq. (4.8)) resulting from electrically activated fibers has to be considered for an eccentric contraction as well as the force enhancement by titin (Eq. (4.9)).

The force–fiber stretch curve of the EDL muscle fiber model in fiber direction for eccentric contractions is compared to experimental results of rat EDL muscle fibers [211] in Fig. C.1. The forces are normalized to the maximum isometric force generated in fully activated muscle fibers.

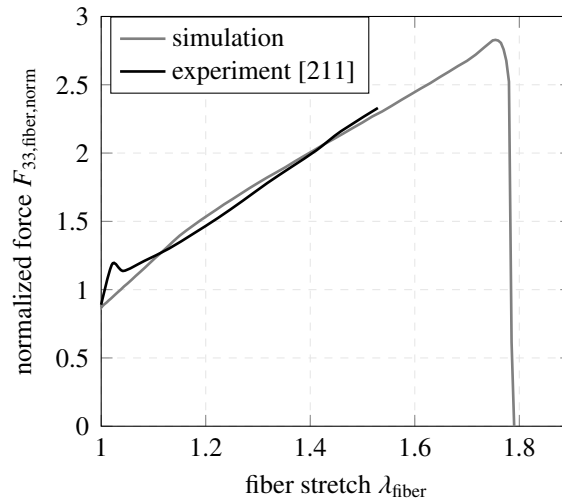


Figure C.1: Eccentric contraction. Our simulation results are in excellent agreement with the experimental results of a rat EDL muscle fiber [211]. Both fiber force–fiber stretch curves, normalized to the maximum isometric force for fully activated muscle fibers, show an almost linear increase in force, see also the results of [86, 180]. Based on further experimental data [211], we extrapolate linearly for higher strains until bundles of myofibrils rupture. Then, the force quickly drops to zero due to an immediate failure of the fiber. The maximum force value before fiber rupture is more than three times the force at the starting point of active strain.

In the experiment, the muscle fiber is actively stretched at an initial sarcomere length close to $2.0\ \mu\text{m}$, which corresponds to the initial sarcomere length used in the simulation. The simulation results correlate well with the experimental results. The total forces in both curves increase almost linearly, also in agreement with [86, 180]. Titin causes the force enhancement, as its strongly nonlinear increasing force resists the decreasing active force of the contracting units for higher strains. According to additional results [211], the progression is proceeded linearly, resulting in a force increase by more than three times from the beginning of active strain until rupture. The force drops sharply to zero above a fiber stretch of $\lambda_{\text{fiber}} = 1.75$, because ruptured bundles of myofibrils result in the sudden failure of the entire muscle fiber.

In Fig. C.2, the stress-strain curves for the fiber are depicted in the passive state and for an eccentric contraction in fiber direction. Due to titin's force enhancement, the stresses increase strongly during eccentric contraction. The rupture stress in an eccentric contraction is slightly more than four times higher than in a passively loaded fiber at the same strain. This is mainly attributed to the high stresses in titin, because the active stresses are almost zero at this fiber stretch.

These simulation results agree with the findings [73] that activated fibers have a higher tensile strength and can absorb considerably more energy than non-activated fibers, which protects activated fibers from injury. Furthermore, the damage range for activated fibers is much larger than for non-activated fibers. This can be explained by the activation capability being first declined by damage, especially, and only later the tensile properties are affected [148].

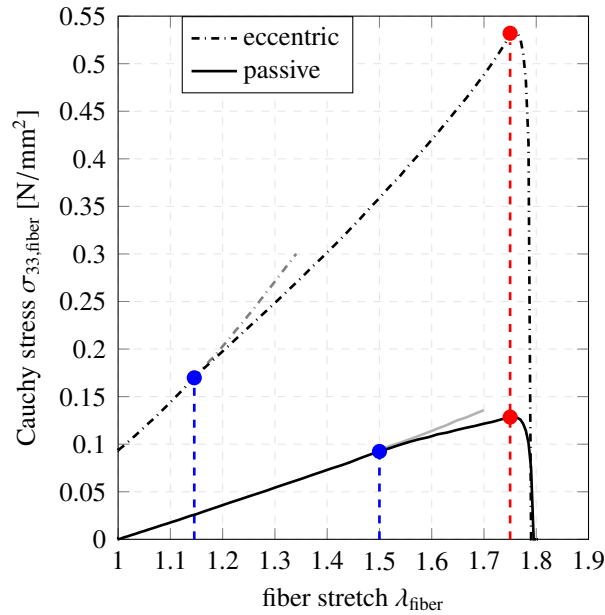


Figure C.2: Stress–fiber stretch relationship for muscle fibers (level 3) until total fiber fracture for the nonactivated, passive state and for an eccentric contraction. The blue dots mark the starting point for microcrack formation and the red dots denote the beginning of myofibrillar failure. The rupture of bundles of myofibrils immediately afterwards leads to total fiber failure, so that the stresses drop to zero. The gray curve sections after the blue dots indicate the course of the passive and eccentric curves without damage. Due to the high stresses, damage occurs earlier in activated fibers. However, the complete fiber fails at the same strain in both cases. As a result, activated fibers can absorb significantly more energy [73] than non-activated fibers.

C.2.2 Local strains in a 90 % pre-damaged muscle fiber at fascicle level in a realistic loading case

For an averaged 90 % pre-damage in the cross-section of the central fiber (intact titin), as studied in Sect. 4.5.2, the local strains in the muscle fibers of the large fascicle RVE are shown for a macroscopic fiber stretch of $\lambda_{\text{fiber}} = 1.4$ (Fig. C.3). This figure is a sectional view to visualize the strains in the pre-damaged fiber area and in the adjacent previously undamaged fibers.

In the pre-damaged fiber, the normal strain is maximal at the boundary of the fiber and minimal within the fiber, whereas the shear strain shows an inverse distribution. The maximum shear strains are more than two times larger than the maximum normal strains (Fig. C.3). Despite the lower normal strain within the pre-damaged fiber compared to the previously undamaged fibers, the maximum principal strains are larger in the pre-damaged one (Fig. 4.8) due to the immense shear strain differences (Figs. 4.9 and C.3) in the fascicle. For higher macroscopic strains ($\lambda_{\text{fiber}} > 1.4$), the normal strains in the pre-damaged fiber increase and approach the normal strains in the undamaged fiber. Therefore, the flattening of the maximum principal strains in the pre-damaged fiber (Fig. 4.8c) results from the decreasing shear strains (Fig. 4.9).

In general, to prevent early failure, it is necessary to reduce these high shear strains, which

increase sharply with higher pre-damage.

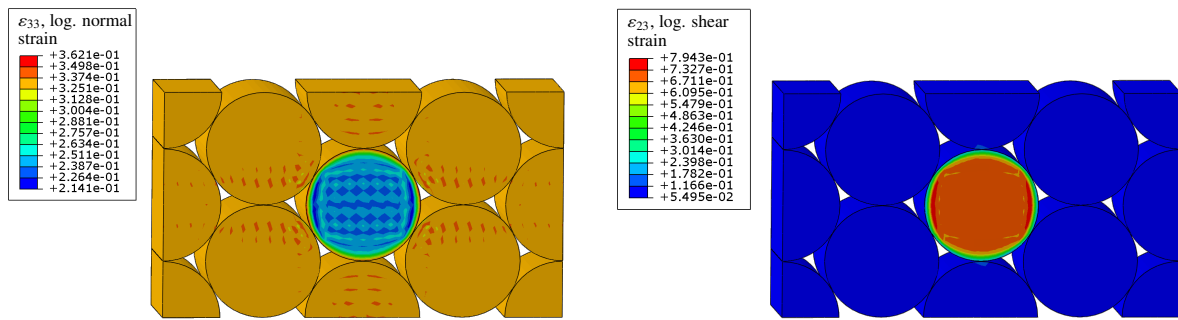


Figure C.3: Sectional views of the large fascicle RVE with a 90% pre-damaged central muscle fiber (intact titin) at fiber stretch $\lambda_{\text{fiber}} = 1.4$. The normal strains (left) and the shear strains (right) are presented in the cross-section of the fascicle, where the pre-damaged fiber part is located. The normal strains are maximal in the cross-section of the pre-damaged fiber area where the shear strains are minimal and vice versa. For a macroscopic fiber stretch of $\lambda_{\text{fiber}} = 1.4$, the maximum logarithmic shear strain is more than two times larger than the maximum logarithmic normal strain.

D | Supplementary Material of article 3

D.1 Validation of titin's and endomysium's observed behavior in pre-damaged fascicles

We investigate the general validity of the elaborated characteristics of titin and endomysium in pre-damaged fascicles by additional simulations with the large RVE (see Fig. 4.5) for varying fiber-endomysium-Young's modulus ratios, different muscle fiber shapes and larger fiber volume fractions. A realistic loading of the fascicle RVE consisting of normal and shear forces is modeled for a 90 % pre-damaged central muscle fiber (see Fig. 4.7) in the case of an eccentric contraction.

D.1.1 Comparison between different fiber-endomysium-Young's modulus ratios

Fiber-endomysium-Young's modulus ratios smaller than 1.0 are used as the endomysium is generally stiffer than the muscle fiber in different muscles and species [75]. A pre-damaged muscle fiber with equally pre-damaged titin and intact titin is investigated for stiffness ratios larger and smaller than 0.725, which is the value used in the main part of the paper (results shown in Fig. 4.8b and c and Fig. 4.9). The maximum principal logarithmic strains in the 90 % pre-damaged and neighboring undamaged fiber and the logarithmic shear strains at the same points (see Fig. D.1) show that stiffness ratios larger and smaller than 0.725 do not affect the results.

The strains in the thinnest endomysium area next to the 90 % pre-damaged cross-section of the central muscle fiber (titin is equally pre-damaged) are also examined for stiffness ratios larger and smaller than 0.725 (see Fig. D.2). The strain curves next to the pre-damaged and undamaged fiber are independent of different stiffness ratios.

D.1.2 Comparison between different fiber shapes and fiber volume fractions

We compare muscle fibers with circular and polygonal cross-sections and varying fiber volume fractions (90 %, 92.5 % and 95 %) for the case of muscle fibers with polygonal cross-section (see Fig. D.3). For all cases, the maximum principal logarithmic strains and the shear strains at the

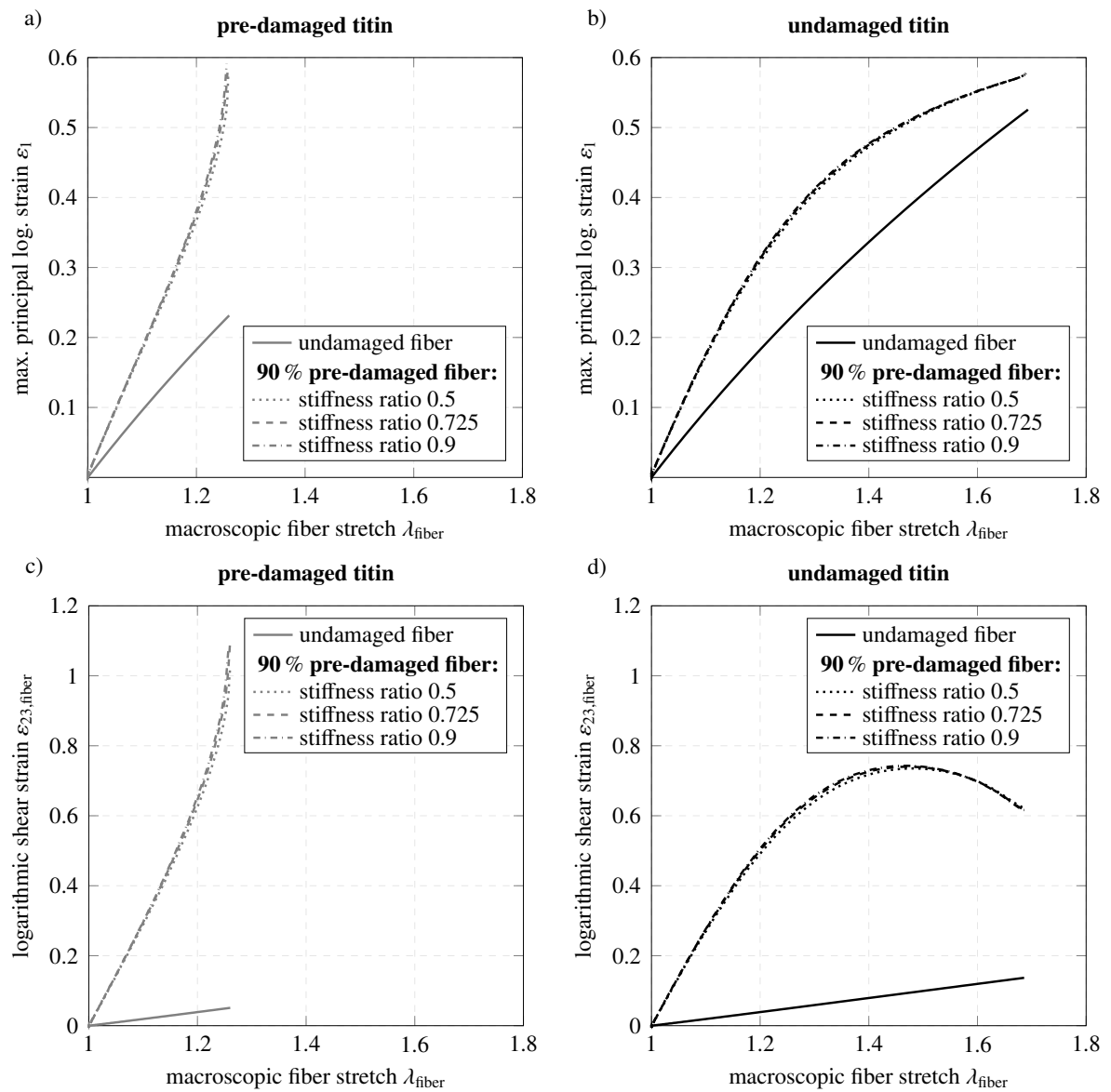


Figure D.1: Influence of titin on the damage behavior in pre-damaged fascicles with different fiber-endomysium-Young's modulus ratios: As done in the main part, the central muscle fiber of the large fascicle RVE is pre-damaged in one cross-section. The results for the maximum principal logarithmic strains (a) and b)) and logarithmic shear strains at the same points (c) and d)) in the pre-damaged and undamaged fiber for the case of equally pre-damaged and undamaged titin show that the stiffness ratio between muscle fiber and endomysium has no influence on the results. The curves for a stiffness ratio of 0.725 represent the results which are already shown in Figs. 4.8b and c and 4.9.

same points are investigated in a 90 % pre-damaged muscle fiber with equally pre-damaged titin as well as intact titin and in a neighboring undamaged fiber for both cases (see Fig. D.4). The results for an RVE with fibers with a circular cross-section and a fiber volume fraction of 90 % are already shown in the main part (see Fig. 4.8b and c and Fig. 4.9). The curves in Fig. D.4 demonstrate that both fiber shape and fiber volume fraction have no influence on the results and,

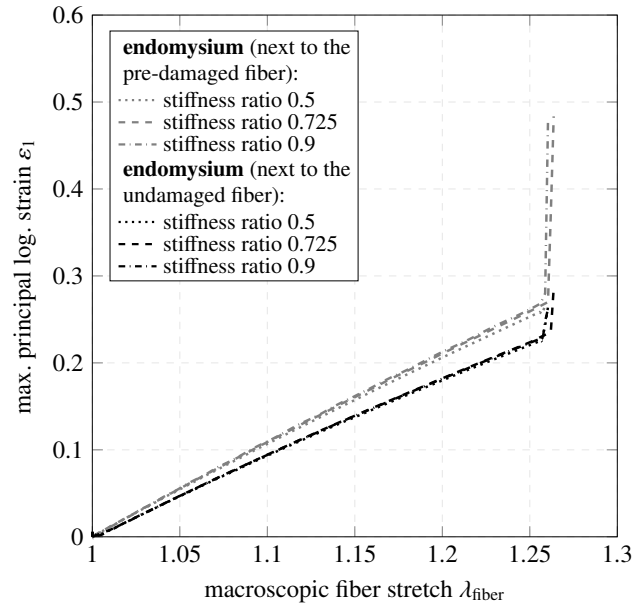


Figure D.2: Endomysium's protection properties for adjacent undamaged muscle fibers in the case of a 90 % pre-damaged muscle fiber (titin is equally pre-damaged) for different fiber-endomysium-Young's modulus ratios: The maximum principal logarithmic strains in the endomysium are examined where endomysium is thinnest next to the pre-damaged cross-section of the central muscle fiber. The curves indicate that the stiffness ratio has no effect on the results.

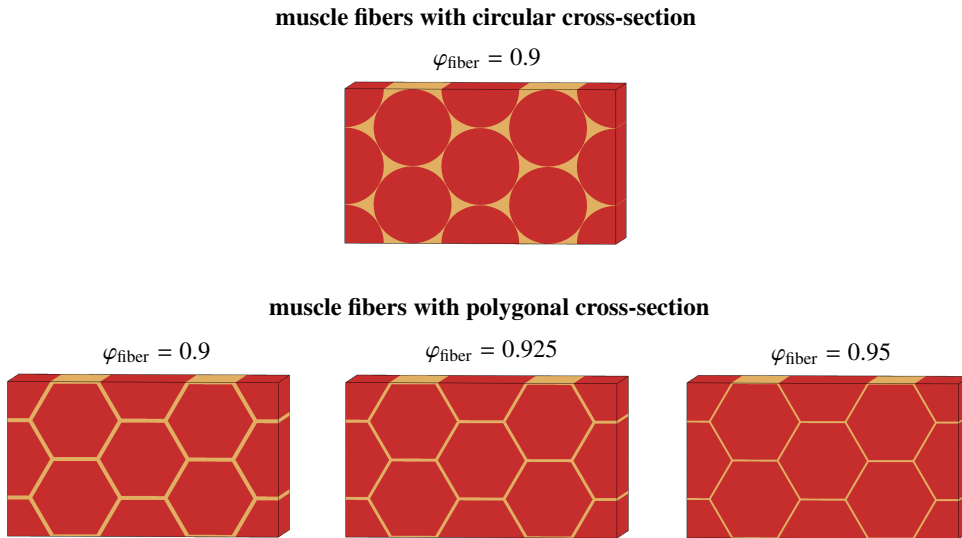


Figure D.3: RVEs with different muscle fiber shapes (circular and polygonal cross-section) and varying fiber volume fractions (90 %, 92.5 % and 95 %) are used to examine their influence on the damage behavior in fascicles. The arrangement of the polygonal muscle fibers results in equal endomysium thickness in the entire RVE.

thus, they underline titin's observed behavior in pre-damaged fascicles.

For all cases, the maximum principal logarithmic strains in endomysium next to the 90 % pre-damaged cross-section of the central muscle fiber (titin is equally pre-damaged) are investigated

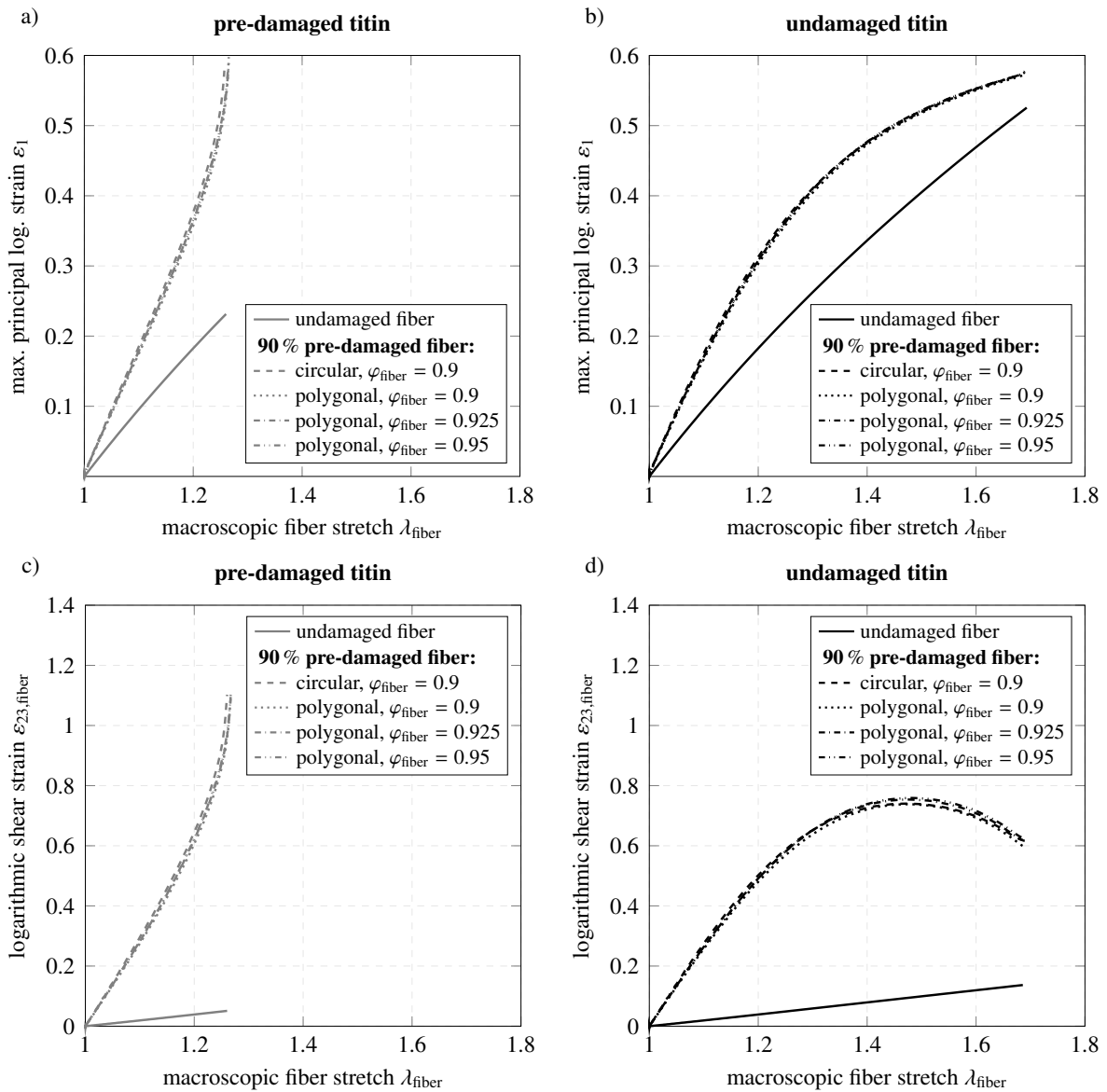


Figure D.4: Influence of titin on the damage behavior in pre-damaged fascicle RVEs with different muscle fiber cross-sections (circular and polygonal) and different fiber volume fractions (90 %, 92.5 % and 95 %): As done in the main part, the central muscle fiber of the large fascicle RVE is pre-damaged in one cross-section. The results for the maximum principal logarithmic strains (a) and b)) and logarithmic shear strains at the same points (c) and d)) in the pre-damaged and undamaged fiber for the case of equally pre-damaged and undamaged titin show that different muscle fiber shapes and larger fiber volume fractions than 90 % do not affect the mechanical behavior. An RVE with 90 % fiber volume fraction and muscle fibers with circular cross-section is used in the main part and its results are presented in Figs. 4.8b and c and 4.9.

at the same area where, for fibers with circular cross-section, the endomysium is thinnest (Fig. D.5). Both the cross-section of the fiber and larger fiber volume fractions hardly affect the strain curves next to the pre-damaged and next to the neighboring undamaged fiber.

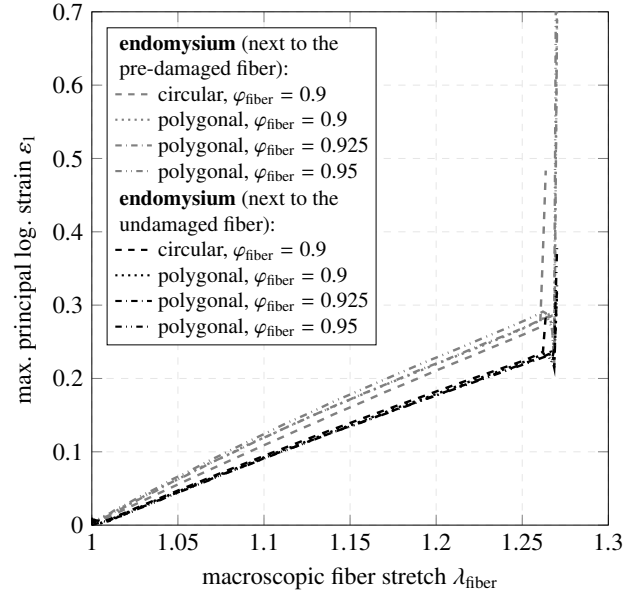


Figure D.5: Endomysium's protection properties for adjacent undamaged muscle fibers in the case of a 90% pre-damaged muscle fiber (titin is equally pre-damaged) for different muscle fiber shapes (circular and polygonal) and different fiber volume fractions (90%, 92.5% and 95%): The maximum principal logarithmic strains in the endomysium are examined next to the pre-damaged cross-section of the central muscle fiber in the same area for all cases which for muscle fibers with circular cross-sections is the thinnest endomysium area. Different cross-section shapes and larger fiber volume fractions than 90% have no significant impact on the results and, therefore, they confirm the concluded behavior of endomysium in pre-damaged fascicles based on the results of circular fibers in RVEs with 90% fiber volume fraction (see also Fig. 4.10).

D.2 Initiation of fiber rupture in RVEs with different arranged polygonal muscle fibers

In Fig. 4.6, the tensile- and shear-loaded small RVE consisting of muscle fibers with circular cross-sections demonstrates the highest risk for damage at the fiber boundary. The results are compared to equally loaded small RVEs with polygonal muscle fibers, one with a symmetrical arrangement and the other with an asymmetrical arrangement of the fibers (see Fig. D.6), in the case of an eccentric contraction. All have the same fiber volume fraction of 90%. The damaged polygonal RVEs confirm the conclusion in the main text that damage occurs first at the fiber boundary.

initiation of fiber rupture

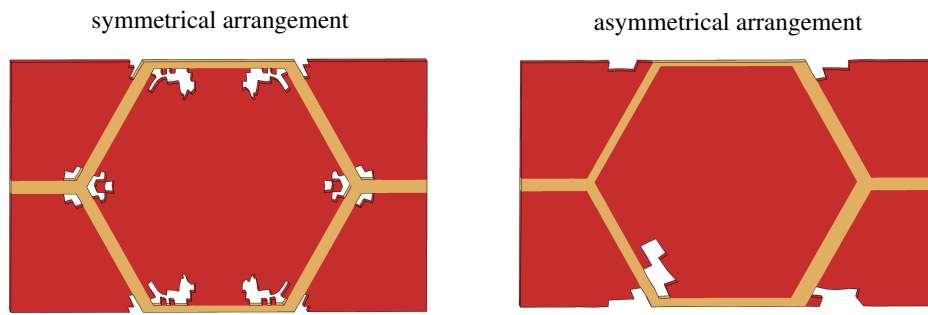


Figure D.6: Two small RVEs with polygonal muscle fibers, one with symmetrically arranged and the other with asymmetrically arranged fibers, are loaded and constraint in the same way as the small RVE with circular fibers (results are shown in Fig. 4.6) in the main part. The RVEs with polygonal muscle fibers confirm the results that the fiber boundary is at high risk for crack initiation.

E | Appendix of article 4

E.1 Material Data

The material and geometrical data for endomysium and muscle fibers are summarized in Tables E.1 and E.2.

E.1.1 Endomysium

The second Lamé parameter for endomysium $\mu_{\text{endo}} = 0.08 \text{ N/mm}^2$ is determined based on the elastic material parameters in Lamsfuss and Bargmann [118] and a Poisson's ratio of $\nu_{\text{endo}} = 0.49$ which is assumed to model nearly incompressible material behavior. This results in a first Lamé parameter of $\lambda_{\text{endo}} = 3.971 \text{ N/mm}^2$. The constant of the Ogden model $\alpha_1 = 7.95$ results from parameter fitting with validation against experimental data, done in Lamsfuss and Bargmann [118].

Parameter	Value	Definition
λ_{endo}	3.971 N/mm^2	first Lamé parameter
μ_{endo}	0.08 N/mm^2 [118]	second Lamé parameter
ν_{endo}	0.49	Poisson's ratio
ρ_{endo}	1174 kg/m^3 [58]	density
α_1	7.95 [118]	constant of the Ogden model for endomysium
α_{endo}	10^{-4} 1/K [151]	thermal expansion coefficient
k_{endo}	0.435 W/[mK] [228]	thermal conductivity
T_0	$308.15 \text{ K} = 35^\circ \text{ C}$ [24]	reference temperature
$c_{p_{\text{endo}}}$	3364 J/[kgK] [137]	specific heat capacity
φ_{endo}	0.1	volume fraction

Table E.1: Material and geometrical data of endomysium

We assume a linear isotropic thermal expansion coefficient of $\alpha_{\text{endo}} = 10^{-4} \text{ 1/K}$ obtained from a steer Achilles tendon and from gelatin [151]. The density $\rho_{\text{endo}} = 1174 \text{ kg/m}^3$ is an average value for tendons and ligaments [58] and is here used for the endomysium. $k_{\text{endo}} = 0.435 \text{ W/[mK]}$ is the average value for the thermal conductivity of connective tissue from [228]. For the specific heat capacity of endomysium, the calculated value $c_{p_{\text{endo}}} = 3364 \text{ J/[kgK]}$ [137] for ligaments and tendon is used.

E.1.2 Muscle fiber

The second Lamé parameter of the muscle fiber $\mu_{\text{fiber}} = 0.044 \text{ N/mm}^2$ is calculated from rat EDL experimental data [143] and a fiber Poisson's ratio of 0.49 for nearly incompressible material behavior. Thus, the first Lamé parameter of the muscle fiber $\lambda_{\text{fiber,Lamé}} = 2.154 \text{ N/mm}^2$ is obtained. For both, tensile and compressive behavior, the same Lamé parameters are assumed.

Parameter	Value	Definition
$\lambda_{\text{fiber,Lamé}}$	2.154 N/mm^2	first Lamé parameter
μ_{fiber}	0.044 N/mm^2 [143]	second Lamé parameter
ν_{fiber}	0.49	Poisson's ratio
ρ_{fiber}	1095 kg/m^3	density
$P_{\text{max}_{35}}$	0.175 N/mm^2 [191]	maximum isometric stress at 35°C
$\bar{\gamma}$	1.0	fiber activation parameter
$\alpha_{\text{fiber}_{\text{pas}}}$	-0.001 1/K [169]	passive linear isotropic thermal expansion coefficient
$\alpha_{\text{fiber}_{\text{rigor}}}$	$3.2 \cdot 10^{-5} \text{ 1/K}$ [15]	rigor linear isotropic thermal expansion coefficient
$\alpha_{\text{fiber}_{\text{act}}}$	$3.2 \cdot 10^{-5} \text{ 1/K}$	active linear isotropic thermal expansion coefficient
ΔH	82 kJ/mol	enthalpy change
R	8.314 J/[K mol]	molar gas constant
$T_{0.5}$	280.15 K	temperature at 50 % maximum isometric stress
$k_{x,\text{fiber}}, k_{y,\text{fiber}}$	0.543 W/[mK]	thermal conductivity (across fibers)
$k_{z,\text{fiber}}$	0.491 W/[mK]	thermal conductivity (along fibers)
T_0	$308.15 \text{ K} = 35^\circ \text{C}$ [24]	reference temperature
$c_{p_{\text{fiber}}}$	3317 J/[kgK]	specific heat capacity
l_{s0}	$2.0 \text{ }\mu\text{m}$	resting sarcomere length
l_{norm}	$1.0 \text{ }\mu\text{m}$	quantity to normalize the force-length relation
d_{fiber}	$65 \text{ }\mu\text{m}$ [177]	diameter
φ_{fiber}	0.9	volume fraction

Table E.2: Material and geometrical data of rat EDL muscle fiber

The muscle fibers are assumed to be maximally activated with a constant activation parameter of $\bar{\gamma} = 1.0$ along the entire fiber. $P_{\text{max}_{35}} = 0.175 \text{ N/mm}^2$ is the average value of the measured maximum isometric stresses at 35°C in a rat EDL muscle fiber [191]. The parameters for the sigmoidal function $P_{\text{max}}(T)$ in Eq. (5.19) used to describe the temperature dependent maximum isometric stress are calculated via the van't Hoff equation. We plot $\ln(P_{\text{max}_{\text{exp}}}/(P_{\text{max}} - P_{\text{max}_{\text{exp}}}))$ versus $1/T$, as done in [170]. $P_{\text{max}_{\text{exp}}}$ is the temperature dependent maximum isometric stress from experiments with a rat EDL muscle fiber [172] and P_{max} is the total maximum isometric stress. We obtain an approximately linear curve, thus, with the linear form of the van't Hoff

equation given in the form

$$\ln \left(P_{\max_{\text{exp}}} / [P_{\max} - P_{\max_{\text{exp}}}] \right) = -\frac{\Delta H}{RT} + \frac{\Delta S}{R} \quad (\text{E.1})$$

the temperature independent change in enthalpy $\Delta H \approx 82000 \text{ J/mol}$ and the change in entropy $\Delta S \approx 293 \text{ J/[K mol]}$ are determined. The absolute temperature at 50% maximum isometric stress $T_{0.5}$ indicates the temperature for $\ln(P_{\max_{\text{exp}}}/[P_{\max} - P_{\max_{\text{exp}}}] = 0$, which results in $T_{0.5} \approx 7^\circ \text{ C} = 280.15 \text{ K}$. Our sigmoidal curve for the temperature dependent maximum isometric stress (Eq. (5.19)) is in excellent agreement with the experimental results of a rat EDL muscle fiber [172] (Fig. E.1).

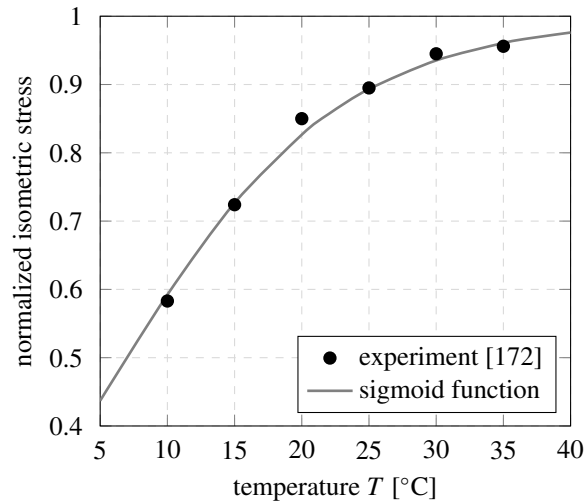


Figure E.1: The maximum isometric stress-temperature dependence of muscle fibers represented by a sigmoid function: The model reproduces the experimental behavior of the rat EDL muscle fiber very well.

The linear isotropic thermal expansion coefficient of the fiber α_{fiber} differs between passive, active and rigor muscle fibers. Therefore, α_{fiber} in Eqs. (5.14) and (5.16) needs to be replaced by $\alpha_{\text{fiber}_{\text{pas}}}$ in the passive state, by $\alpha_{\text{fiber}_{\text{act}}}$ in the active state and by $\alpha_{\text{fiber}_{\text{rigor}}}$ in case of a rigor fiber. In the passive state, the thermal expansion coefficient of muscle fibers $\alpha_{\text{fiber}_{\text{pas}}} = -0.001 \text{ 1/K}$ (taken from [169]) is negative (see also [95] for the entire passive muscle), however, in active and rigor fibers, the linear isotropic thermal expansion coefficient is positive. Since the abrupt tension decrease with temperature increase is similar in active contraction and in rigor, see [77], the same thermal expansion coefficient is assumed for both cases. We set $\alpha_{\text{fiber}_{\text{rigor}}} = \alpha_{\text{fiber}_{\text{act}}} = 3.2 \cdot 10^{-5} \text{ 1/K}$ [15] which agrees with the measured thermal expansion coefficient and thermoelastic heat in rigor [14, 74, 113] and in tetanic contraction [234]. Over time, the stress increases with increasing temperature in active muscle fibers (see [77]) due to the isometric stress-temperature dependence. This is in contrast to rigor fibers which are not able to generate more active force as a result of rigidity. Thus, the isometric stress is assumed to be constant over temperature in rigor muscle fibers. We assume constant thermal expansion coefficients independent of the sarcomere length as similar thermal expansion coefficients are observed

for shorter and longer sarcomeres [77]. The difference in the stress-temperature behavior for passive, active and rigor fibers as well as for endomysium is compared in Figs. E.3 and E.4.

The rule of mixture is used to calculate the density, heat capacity and thermal conductivity parallel and perpendicular to fiber direction for fiber matrix composites:

$$\rho_{\text{muscle}} = \rho_{\text{fiber}}\varphi_{\text{fiber}} + \rho_{\text{endo}}\varphi_{\text{endo}}, \quad (\text{E.2})$$

$$c_{p_{\text{muscle}}} = c_{p_{\text{fiber}}}\varphi_{\text{fiber}} + c_{p_{\text{endo}}}\varphi_{\text{endo}}, \quad (\text{E.3})$$

$$k_{z,\text{muscle}} = k_{z,\text{fiber}}\varphi_{\text{fiber}} + k_{\text{endo}}\varphi_{\text{endo}}, \quad (\text{E.4})$$

$$\frac{1}{k_{x,\text{muscle}}} = \frac{\varphi_{\text{fiber}}}{k_{x,\text{fiber}}} + \frac{\varphi_{\text{endo}}}{k_{\text{endo}}}. \quad (\text{E.5})$$

With the muscle density $\rho_{\text{muscle}} = 1103 \text{ kg/m}^3$ (average value from [37, 58, 97, 160]), the fiber volume fraction $\varphi_{\text{fiber}} = 0.9$, the endomysium volume fraction $\varphi_{\text{endo}} = 0.1$, the muscle specific heat capacity $c_{p_{\text{muscle}}} = 3322 \text{ J/[kgK]}$ (average value from [50, 54, 89]) and the muscle thermal conductivity $k_{z,\text{muscle}} = 0.485 \text{ W/[mK]}$ [96] along and $k_{x,\text{muscle}} = k_{y,\text{muscle}} = 0.53 \text{ W/[mK]}$ [96] across the muscle fibers, we obtain the values given in Table E.2.

E.2 Influence of temperature on active muscle fiber force

In muscle fibers, temperature not only influences the passive material properties but also the active ones. For small physiological temperatures, the tetanic fiber force varies strongly and increases with temperature until the maximum value is reached. At higher physiological temperatures, studies [13, 42, 171] even observed a low fall in tetanic fiber force. Compared to the twitch tension, only the absolute tetanic force value is affected by temperature while its temporal course of fiber activation is temperature-independent [13, 46].

The crossbridges between actin and myosin in sarcomeres, which provide the basis for force generation, are influenced by temperature. Raising temperatures increase (i) the probability for crossbridge formation [43] and (ii) the generated force per crossbridge [168] which in total leads to higher tetanic fiber force.

In different species and muscles, the normalized tetanic fiber force-temperature relationships show varying thermal dependences (see [168]) with the maximum tetanic fiber force occurring at different temperatures (Fig. E.2a). Tetanic force-temperature dependences are described by the Q_{10} -value [13]: small Q_{10} -values represent a small thermal dependence and high Q_{10} -values a strong influence of temperature on the generated fiber force.

The adaptability to different living conditions such as the common ambient temperature could explain the varying Q_{10} -values. Compared to approximately constant body temperatures in homeotherms, poikilothermic animals change their body temperature with ambient temperature, thus, their muscles are exposed to large temperature ranges. This can be a reason for the generally lower tetanic force-temperature dependences (lower Q_{10} -value) in poikilothermic animals such as amphibians [13] and reptiles (see also the lizard and frog muscles in Fig. E.2a) than in

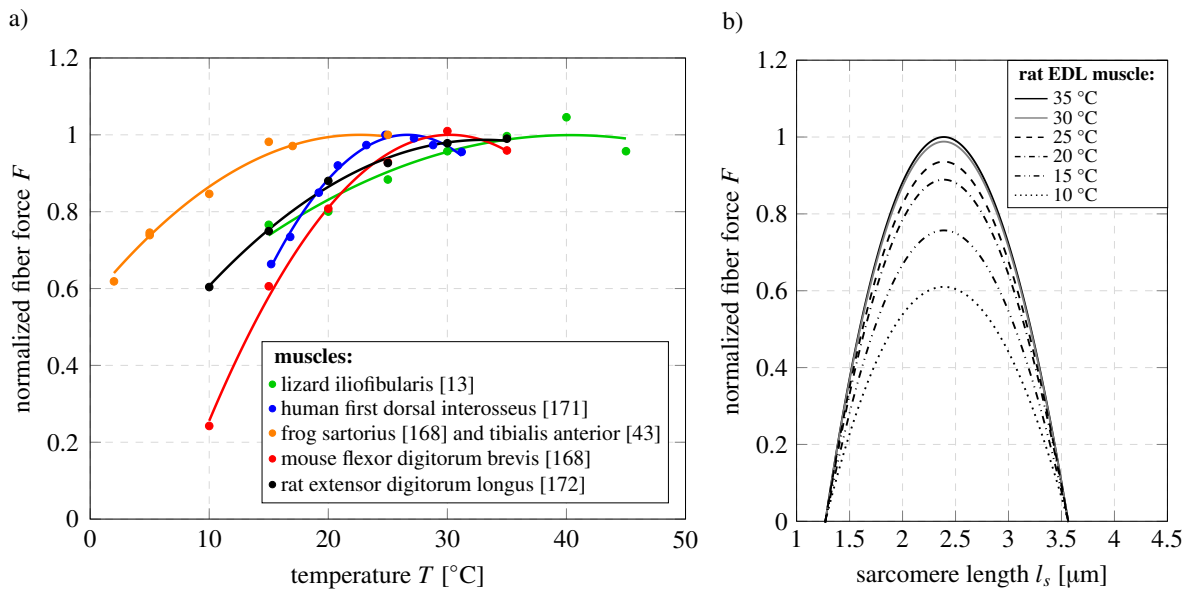


Figure E.2: a) Temperature dependence of the generated active forces for muscle fibers of various species obtained from experiments. The tetanic forces are normalized by the maximum tetanic force of the respective muscle fiber. In all cases, the fiber force increases with temperature over long ranges. However, the strength of force increase and the position of maximum fiber force varies for different species. b) Influence of temperature on the force-length-relation of the rat EDL muscle. The force length-relation is only scaled for different temperatures, thus, the maximum force is generated at the same sarcomere length.

homeotherms as mammals [39, 55, 171] (see also the human and mouse muscles in Fig. E.2a). However, further studies are required here as homeotherms can have similarly small tetanic force-temperature dependences as poikilothermic animals [13, 104] (compare the results of rat EDL muscle with the lizard and frog muscles in Fig. E.2a). Living conditions of the species also influences the temperature at which maximum tetanic tension is generated. The maximum fiber force is normally reached at physiological temperatures to which living organisms are mainly exposed [12, 168]. For example, the myotomal muscles of the Antarctic fish bullrout, whose body temperature varies between 2°C and 17°C [109], generate maximum tetanic tension around 15°C , whereby human muscle temperature can range between 20°C and 40°C [185] and the maximum tetanic tension of the human first dorsal interosseous muscle is reached at ca. 30°C [171]. Maximum tetanic tensions occur similar temperatures in humans, mice and rats, however, they occur at different temperatures in lizards and frogs (Fig. E.2a). In accordance with rather cold environmental temperatures, the analyzed frog muscle fibers generate maximum forces around 20°C . Since the lizard *Dipsosaurus dorsalis* lives in hot desert regions [13], their muscle fibers can generate maximum forces at much higher temperatures.

In Fig. E.2b, the temperature dependence of the force-length-relation normalized at a temperature of 35°C is shown for the rat EDL muscle (normalized stress-temperature data from [172]). Changing the muscle temperature only results in a scaled force-length curve while the maximum force is always reached at the same sarcomere length [39, 55].

E.3 Further results

Figs. E.3 - E.5 illustrate the general thermomechanical behavior of the entire fascicle and its components muscle fiber and endomysium. The fascicle is homogeneously heated to 40° C and cooled to 30° C and the fascicle length remains constant. The stresses during heating are comparable to those during an induced heating of muscle fibers by sport activities, since activated fibers heat up very slowly over several minutes [7, 18] and due to the fast temperature propagation within the fascicle (e.g. Fig. 5.3a), almost a homogeneous temperature increase can be assumed.

For passive muscle fibers, the negative thermal expansion coefficient results in tensile stresses during heating and compressive stresses during cooling which increase with temperature (Fig. E.3a).

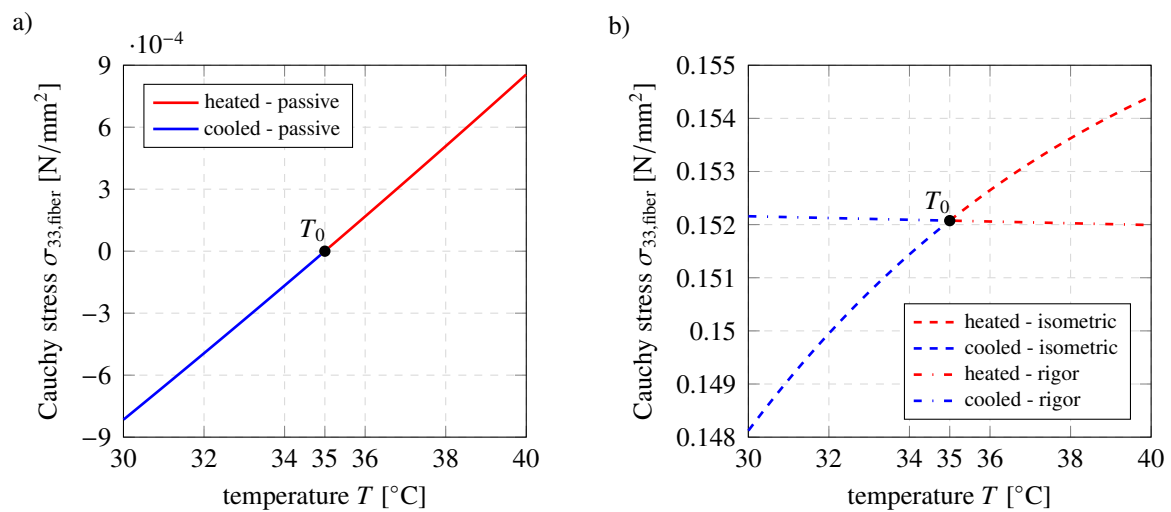


Figure E.3: Thermal stresses in the fiber for heated and cooled fascicles. a) Tensile stresses are generated in heated passive muscle fibers and compressive stresses in cooled fibers. b) The positive thermal expansion of rigor muscle fibers slightly reduces the tensile stress during heating and increases the stress during cooling. Isometrically contracted fibers exhibit the same thermal expansion behavior. However, the fiber responds differently due to the isometric stress–temperature dependence resulting in tensile stresses that increase with heating and decrease with cooling.

In rigor muscle fibers, which are permanently contracted, we assume a constant active stress over temperature. Starting from the active tensile stress at resting sarcomere length l_{s0} and reference temperature T_0 , the thermomechanical behavior of rigor muscle fibers exhibits inverse behavior compared to passive fibers (Fig. E.3b). The low positive thermal expansion coefficient leads to slightly decreasing tensile stresses during heating and slightly increasing tensile stresses during cooling. The same thermal expansion coefficient is assumed for isometrically contracted muscle fibers, however, heating generates thermal tensile stresses and cooling thermal compressive stresses in this case. The generated active forces varying with temperature (Fig. E.1) strongly influence the total stress response over temperature in contrast to the small positive thermal expansion coefficient. Thus, the isometric curve in Fig. E.3b adopts a similar

shape as in Fig. E.1.

In a passive fascicle, endomysium is subjected to compressive stresses during heating and to tensile stresses during cooling due to the positive sign of the thermal expansion coefficient (Fig. E.4). In fascicles with rigor muscle fibers or isometrically contracted fibers, heating/cooling results in compressive/tensile stresses in endomysium which are about 85 % lower than those in passive fascicles. This is caused by the high active tensions in the muscle fibers relieving the endomysium.

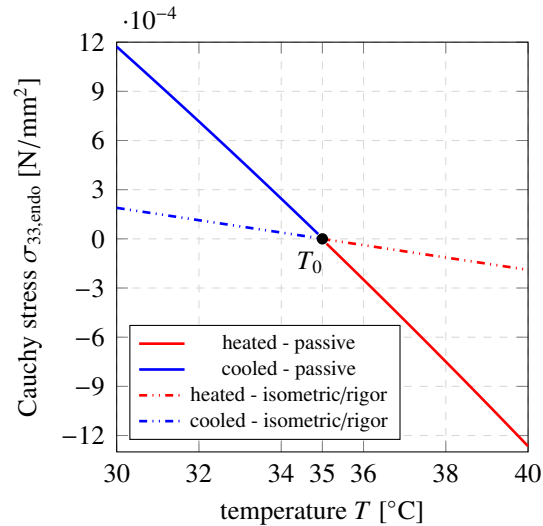


Figure E.4: Thermal stresses in endomysium. The positive thermal expansion coefficient results in compressive stresses during heating and tensile stresses during cooling. If the endomysium is surrounded by rigor or activated muscle fibers, the absolute value of the thermal stresses in endomysium is smaller compared to purely passive fiber behavior.

We only consider the thermal expansion and neglect the temperature dependence of the stiffness, which would result in stiffer muscle behavior at lower temperatures [149]. The passive muscle fiber shows an approximately linear increase of stress (Fig. E.5). In isometric contraction, the behavior is dominated by the force-length relation until, at very large strains, no active force can be generated anymore and only passive forces exist in the fiber. The endomysium exhibits a strongly nonlinear stress-strain behavior. The curves for 20° C and 40° C (Fig. E.5a) match well with the results in Figs. E.3 and E.4 as thermal tensile stresses are generated in heated passive and active fibers and small thermal compressive stresses in heated endomysium. The overall stress-strain curves for fascicle in an isometric contraction as well as in the passive state (Fig. E.5b) indicate that thermal stresses in the muscle fiber are dominant due to the higher volume fraction, as the total stresses are larger at higher temperatures.

A short-term thermal treatment of a cramped fascicle is examined. The muscle fibers in cramped fascicles are involuntarily and permanently contracted as the connection between actin and myosin via crossbridges cannot be detached due to ATP deficit. We assume the fibers to generate the same tension as in a tetanic contraction and to be fully activated with an activation parameter $\bar{\gamma} = 1$. The EMG activation is hardly affected by a short temperature treatment and,

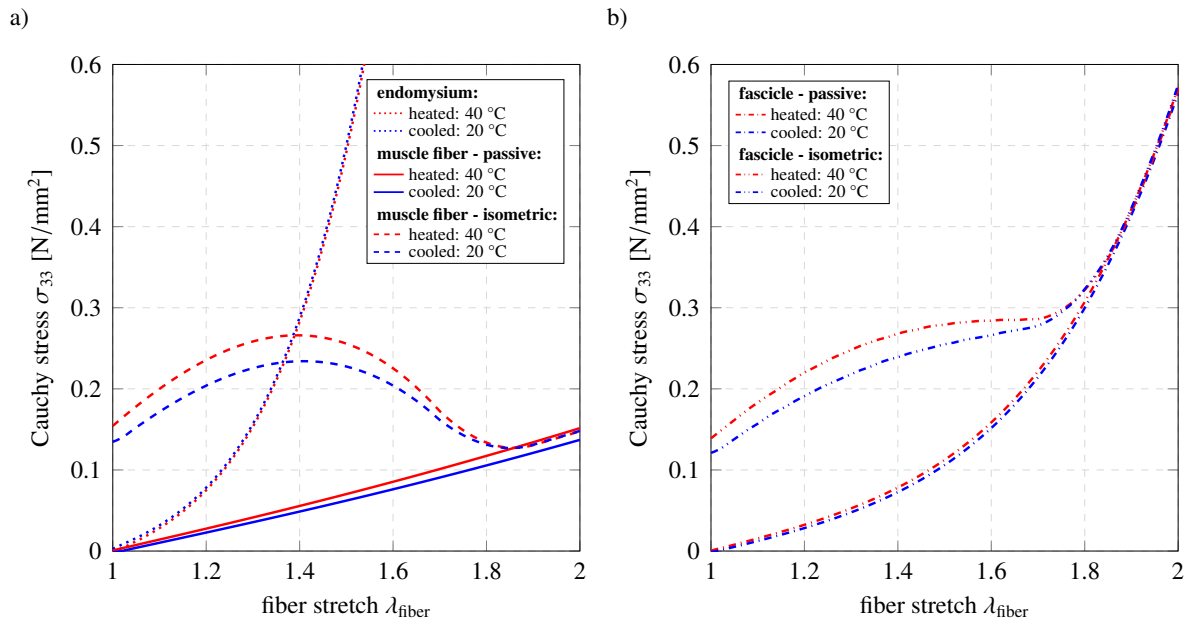


Figure E.5: Stress-strain curve at 20 °C and 40 °C for muscle fiber, endomysium and fascicle. a) The negative thermal expansion coefficient of passive muscle fibers results in higher stresses with increasing temperature. The same holds true for an isometric contraction despite the positive thermal expansion coefficient, as the isometric stress–temperature dependence dominates the behavior. The small positive thermal expansion coefficient of endomysium leads to slightly smaller stresses at higher temperatures. b) The thermal stresses in the muscle fiber dominate the overall stress-strain response of the fascicle during temperature variation, thus, higher temperatures cause higher stresses.

thus, $\bar{\gamma}$ remains constant. Since rigor represents a type of muscle cramp, the same properties as in the rigor case are assumed for the fibers, therefore, the isometric stress is assumed to be constant over temperature.

The fascicle is heated to 38.8 °C and cooled to 30 °C at the outer surface (Fig. 5.3) and the Cauchy stresses in fiber direction at points P_1 – P_4 (Fig. E.6) are evaluated over temperature. The fascicle length remains constant. For the muscle fiber and the endomysium heating causes a short stress increase rather than an immediate stress reduction (Figs. E.3b and E.4) and cooling exhibits the opposite behavior. This behavior is more pronounced in the inner point. Due to the heterogeneous temperature distribution, the outer fibers and the outer endomysium are affected earlier by a temperature change (Fig. 5.3) and, thus, a stress variation. To compensate the increase/decrease in stress in the outer region, the inner point experiences slightly lower/higher stresses. Thus, at equal temperatures, different stress values are obtained in different regions, which are, however, nearly identical when a homogeneous temperature distribution is achieved in the entire fascicle (Fig. E.6).

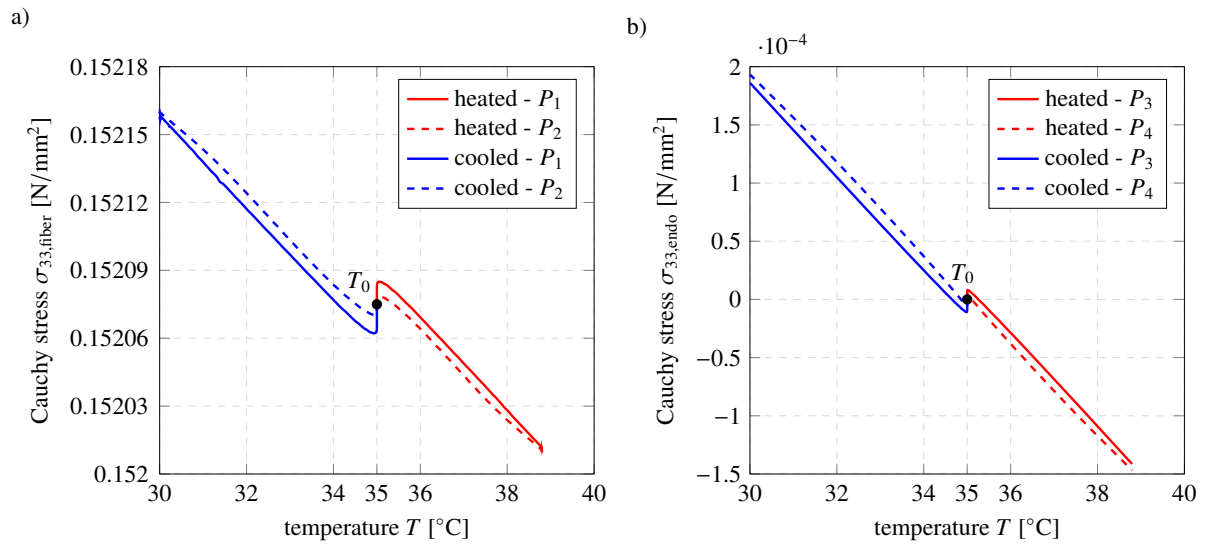


Figure E.6: Temperature influence on the Cauchy stress in muscle fibers and endomysium in a cramped fascicle for a short-term temperature treatment: The outer surface of the fascicle is heated to 38.8° C and cooled to 30° C and the development of Cauchy stresses at different points (Fig. 5.3) are investigated. Consistent with the positive thermal expansion coefficients, heating leads to compressive stresses in the endomysium and reduced tensile stresses in the muscle fiber and cooling causes reverse behavior. However, at a temperature of 35° C, first, a stress increase is observed in heated fascicles and a stress decrease in cooled fascicles, which is more pronounced in the inner points. Thus, different stresses occur in inner and outer muscle fibers and in inner and outer endomysium despite equal temperature values.

F | Supplementary Material of article 4

F.1 Validation of the observed influence of thermal treatment on muscle fibers with trigger points - Variation of the fiber volume fraction

We investigate the general validity of the observed influence of thermotherapy and cryotherapy on muscle fibers with trigger points by varying the fiber volume fraction (Fig. F.1). As in the main part of this work, the fascicle has a reference temperature of $T = 35\text{ }^{\circ}\text{C}$ and its surface is heated to $T = 38.8\text{ }^{\circ}\text{C}$ or cooled to $T = 30\text{ }^{\circ}\text{C}$.

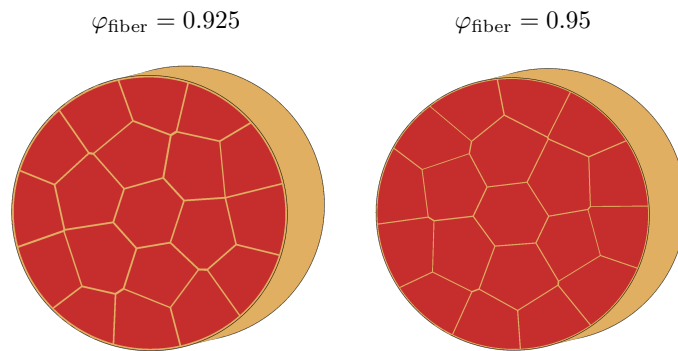


Figure F.1: Fascicle models with fiber volume fractions of 92.5% (left) and 95% (right).

We compare the strains and stresses in fiber direction along the center of the tensed muscle fiber in fascicles with 90%, 92.5% and 95% fiber volume fraction (Figs. F.2 - F.4)¹⁴. Higher fiber volume fractions have no influence on the development of strains and stresses after short-term (without EMG activity reduction) and long-term (EMG activity reduction is considered) heat and cold treatment. Thus, they confirm the observed impact of thermotherapy and cryotherapy on a tensed muscle fiber.

¹⁴The results for a fascicle with 90% fiber volume fraction are already shown in the main part (see Fig. 5.5a and c and Fig. 5.6).

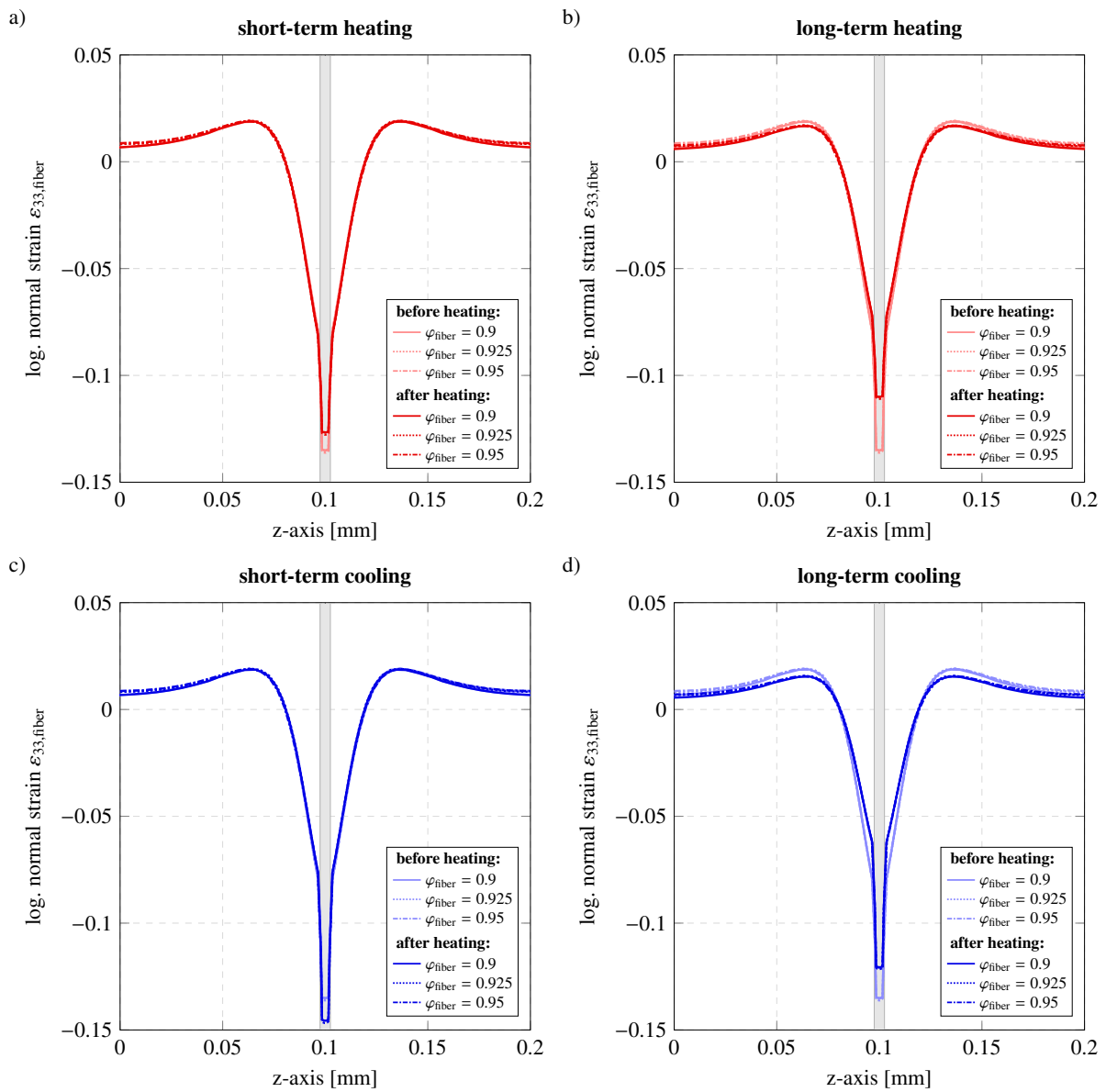


Figure F.2: Influence of short-term and long-term heating (a) and b)) and cooling (c) and d)) on the strains in a tensed muscle fiber for fascicles with different fiber volume fractions (90 %, 92.5 % and 95 %): The grey bar represents the region of the trigger point. The plotted strains in fiber direction show that fiber volume fractions larger than 90 % do not affect the influence of thermotherapy and cryotherapy. The fascicle model with 90 % fiber volume fraction is used in the main part of the paper and its strain results are presented in Fig. 5.5a and c.

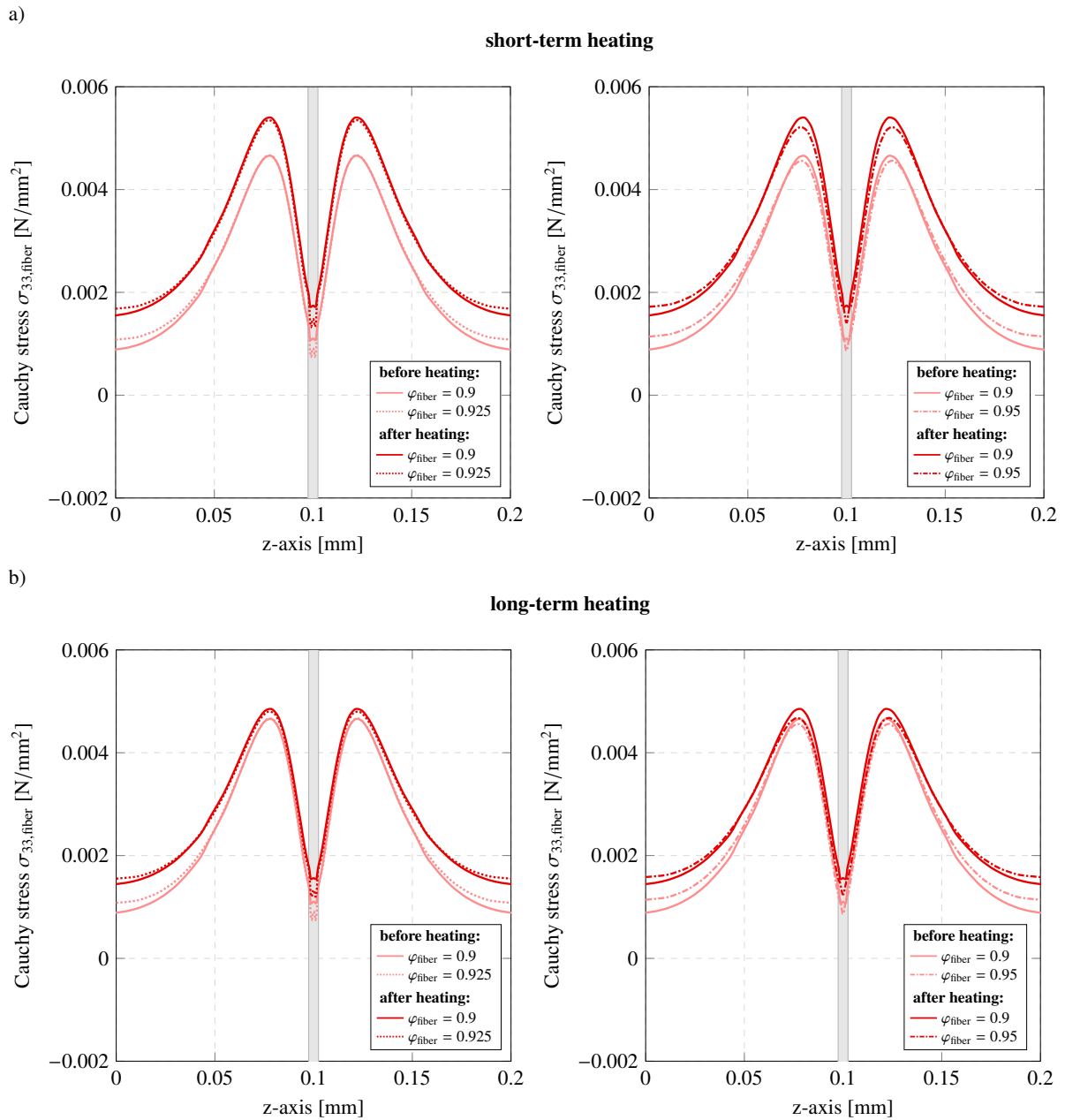


Figure F.3: Influence of short-term (a) and long-term (b) heating on the Cauchy stresses in a tensed muscle fiber for fascicles with different fiber volume fractions (90 %, 92.5 % and 95 %): The grey bar represents the region of the trigger point. The plotted stresses in fiber direction show that fiber volume fractions larger than 90 % do not influence the impact of thermotherapy observed in the main part. The curves for 90 % fiber volume fraction represent the results which are already shown in the main part of the paper in Fig. 5.6a.

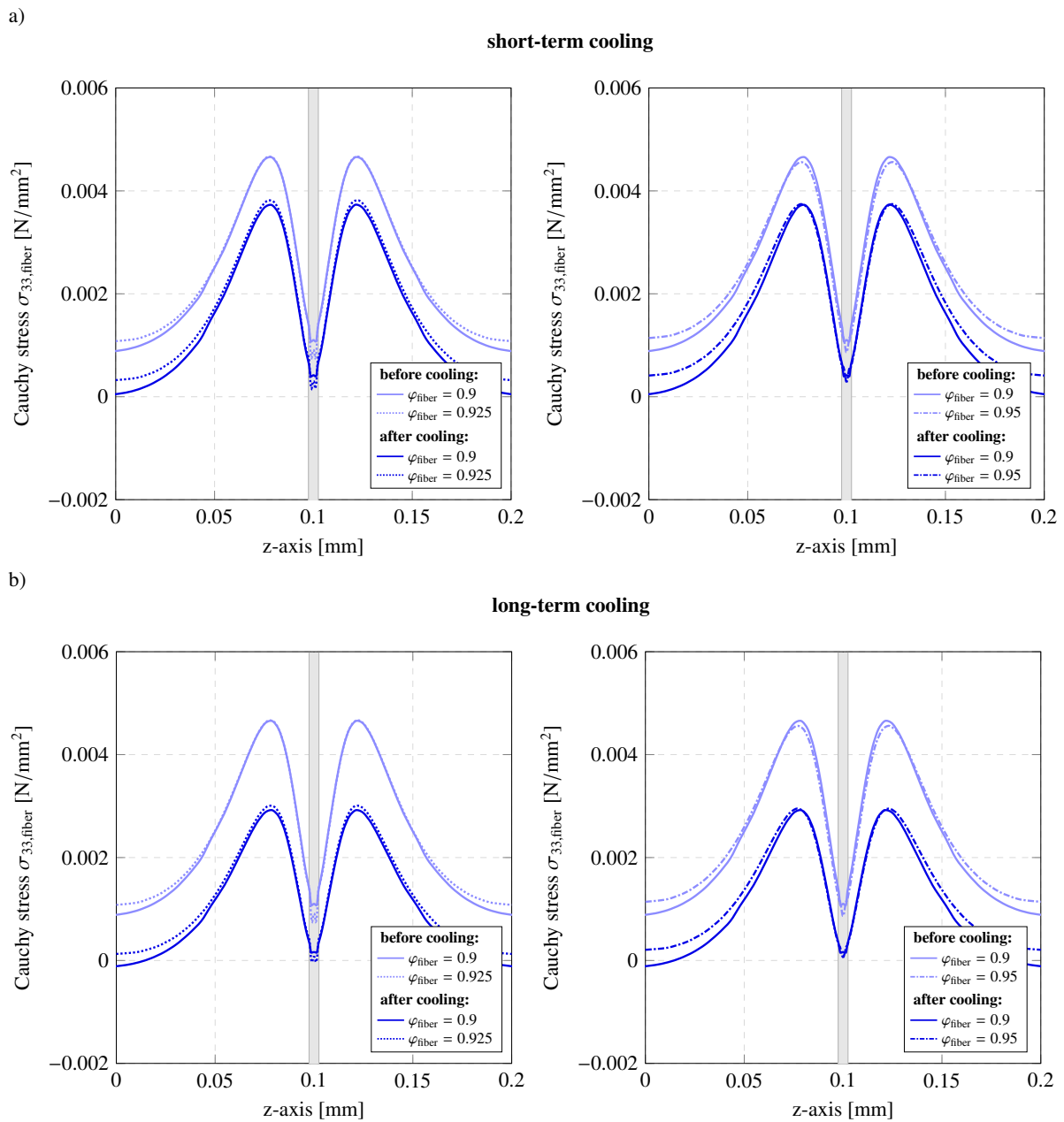


Figure F.4: Influence of short-term (a) and long-term (b) cooling on the Cauchy stresses in a tensed muscle fiber for fascicles with different fiber volume fractions (90 %, 92.5 % and 95 %): The grey bar represents the region of the trigger point. The plotted stresses in fiber direction show that the observed influence of cold treatment in the main part does not change for fascicles with fiber volume fractions larger than 90 %. The curves for 90 % fiber volume fraction are already shown in the main part of the paper in Fig. 5.6b.

Bibliography

- [1] K. Alam, A. V. Mitrofanov, and V. V. Silberschmidt. Finite element analysis of forces of plane cutting of cortical bone. *Computational Materials Science*, 46(3):738–743, 2009.
- [2] B. R. Anderson, J. Bogomolovas, S. Labeit, and H. Granzier. The effects of PKCa phosphorylation on the extensibility of titin's PEVK element. *Journal of Structural Biology*, 170(2):270–277, 2010.
- [3] K. Anderson, S. M. Strickland, and R. Warren. Hip and groin injuries in athletes. *The American Journal of Sports Medicine*, 29(4):521–533, 2001.
- [4] R. B. Armstrong, R. W. Ogilvie, and J. A. Schwane. Eccentric exercise-induced injury to rat skeletal muscle. *Departments of Physiology and Anatomy*, 54(1):80–93, 1983.
- [5] J. A. Ashton-Miller, Y. He, V. A. Kadhiresan, D. A. McCubbrey, and J. A. Faulkner. An apparatus to measure in vivo biomechanical behavior of dorsi- and plantarflexors of mouse ankle. *Journal of Applied Physiology*, 72(3):1205–1211, 1992.
- [6] E. Asmussen. Über die Längenspannungskurven des ruhenden und des aktiven Muskels. *Skandinavisches Archiv für Physiologie*, 74(2):129–141, 1936.
- [7] E. Asmussen and O. Bøje. Body temperature and capacity for work. *Acta Physiologica Scandinavica*, 10(1):1–22, 1945.
- [8] X. Aubert. *Le couplage énergétique de la contraction musculaire*. 1956.
- [9] E. Azizi and T. J. Roberts. Geared up to stretch: Pennate muscle behavior during active lengthening. *Journal of Experimental Biology*, 217(3):376–381, 2014.
- [10] S. Bargmann, B. Klusemann, J. Markmann, J. Schnabel, K. Schneider, C. Soyarslan, and J. Wilmers. Generation of 3D representative volume elements for heterogeneous materials: A review. *Progress in Materials Science*, 96:322–384, 2018.
- [11] M. L. Bartoo, W. A. Linke, and G. H. Pollack. Basis of passive tension and stiffness in isolated rabbit myofibrils. *American Journal of Physiology - Cell Physiology*, 273(1):C266–C276, 1997.

- [12] A. F. Bennett. Thermal dependence of muscle function. *American Journal of Physiology-Regulatory, Integrative and Comparative Physiology*, 247(2):R217–R229, 1984.
- [13] A. F. Bennett. Temperature and muscle. *Journal of Experimental Biology*, 115(1):333–334, 1985.
- [14] S. Y. Bershitsky and A. K. Tsaturyan. Thermoelastic properties of cross-bridges in skinned skeletal muscle fibers of the frog under a condition of rigor. *Biofizika*, 31(3):532–533, 1986.
- [15] S. Y. Bershitsky and A. K. Tsaturyan. Effect of joule temperature jump on tension and stiffness of skinned rabbit muscle fibers. *Biophysical Journal*, 56(5):809–816, 1989.
- [16] R.-J. Bianco, P.-J. Arnoux, J.-M. Mac-Thiong, E. Wagnac, and C.-E. Aubin. Biomechanical analysis of pedicle screw pullout strength. *Computer Methods in Biomechanics and Biomedical Engineering*, 16(sup1):246–248, 2013.
- [17] A. Bielak and A. Bednarski, R. Wojciechowski. 3D Modeling of Leg Muscle Using Mechanochemical Representations of Muscular Tissue and Solid Fibers. In *Information Technologies in Biomedicine*, pages 442–454. Springer, 2018.
- [18] D. Bishop. Warm Up I. *Sports Medicine*, 33(6):439–454, 2003.
- [19] C. Bleiler, P. P. Castañeda, and O. Röhrle. A microstructurally-based, multi-scale, continuum-mechanical model for the passive behaviour of skeletal muscle tissue. *Journal of the Mechanical Behavior of Biomedical Materials*, 97:171–186, 2019.
- [20] S. S. Blemker, P. M. Pinsky, and S. L. Delp. A 3D model of muscle reveals the causes of nonuniform strains in the biceps brachii. *Journal of Biomechanics*, 38(4):657–665, 2005.
- [21] M. Böl. Micromechanical modelling of skeletal muscles: from the single fibre to the whole muscle. *Archive of Applied Mechanics*, 80(5):557–567, 2010.
- [22] M. Böl, A. E. Ehret, K. Leichsenring, C. Weichert, and R. Kruse. On the anisotropy of skeletal muscle tissue under compression. *Acta Biomaterialia*, 10(7):3225–3234, 2014.
- [23] T. K. Borg and J. B. Caulfield. Morphology of connective tissue in skeletal muscle. *Tissue and Cell*, 12(1):197–207, 1980.
- [24] E. Briese. Normal body temperature of rats: the setpoint controversy. *Neuroscience & Biobehavioral Reviews*, 22(3):427–436, 1998.
- [25] C. Bron and J. D. Dommerholt. Etiology of myofascial trigger points. *Current Pain and Headache Reports*, 16(5):439–444, 2012.
- [26] S. V. Brooks and J. A. Faulkner. Contractile properties of skeletal muscles from young, adult and aged mice. *The Journal of Physiology*, 404(1):71–82, 1988.

- [27] F. Buchthal. *The mechanical properties of the single striated muscle fibre at rest and during contraction and their structural interpretation*. Det KGL Danske Videnskabernes Selskab Biologiske Meddelelser, 1942.
- [28] T. A. Butterfield. Eccentric exercise in vivo: strain-induced muscle damage and adaptation in a stable system. *Exercise and Sport Sciences Reviews*, 38(2):51–60, 2010.
- [29] D. Caillerie, A. Mourad, and A. Raoult. Cell-to-muscle homogenization. Application to a constitutive law for the myocardium. *ESAIM: Mathematical Modelling and Numerical Analysis*, 37(4):681–698, 2003.
- [30] D. G. Caldwell, N. Tsagarakis, P. Artrit, and G. A. Medrano-Cerda. Bio-mimetic principles in actuator design for a humanoid robot: Mobile robotics: Climbing and walking robots. *European Journal of Mechanical and Environmental Engineering*, 44(2):75–80, 1999.
- [31] B. Calvo, E. Peña, M. A. Martinez, and M. Doblaré. An uncoupled directional damage model for fibred biological soft tissues. Formulation and computational aspects. *International Journal for Numerical Methods in Engineering*, 69(10):2036–2057, 2007.
- [32] K. B. Campbell, M. V. Razumova, R. D. Kirkpatrick, and B. K. Slinker. Nonlinear myofilament regulatory processes affect frequency-dependent muscle fiber stiffness. *Biophysical Journal*, 81(4):2278–2296, 2001.
- [33] K. S. Campbell. Interactions between connected half-sarcomeres produce emergent mechanical behavior in a mathematical model of muscle. *PLOS Computational Biology*, 5(11):e1000560, 2009.
- [34] A. O. Cankaya, U. Pamuk, and C. A. Yucesoy. The effects of an activation-dependent increase in titin stiffness on whole muscle properties using finite element modeling. *Journal of Biomechanics*, 116:110197, 2021.
- [35] S.-W. Chi, J. Hodgson, J.-S. Chen, V. R. Edgerton, D. D. Shin, R. A. Roiz, and S. Sinha. Finite element modeling reveals complex strain mechanics in the aponeuroses of contracting skeletal muscle. *Journal of Biomechanics*, 43(7):1243–1250, 2010.
- [36] S. J. Choi and J. J. Widrick. Calcium-activated force of human muscle fibers following a standardized eccentric contraction. *American Journal of Physiology-Cell Physiology*, 299(6):C1409–C1417, 2010.
- [37] C. E. Clauser, J. T. McConville, and J. W. Young. Weight, volume, and center of mass of segments of the human body. *Wright-Patterson Air Force Base, Ohio, Aerospace Medical Research Laboratory, AMRL-TR-69-70*, 1969.
- [38] R. Cooke and K. Franks. All myosin heads form bonds with actin in rigor rabbit skeletal muscle. *Biochemistry*, 19(10):2265–2269, 1980.

- [39] P. J. Cullingham, A. R. Lind, and R. J. Morton. The maximal isometric tetanic tensions developed by mammalian muscle, in situ, at different temperatures. *Quarterly Journal of Experimental Physiology and Cognate Medical Sciences: Translation and Integration*, 45(2):142–156, 1960.
- [40] M. Daners. *Anatomisch-Physiologische Bewegungsanalyse als empirisch analytische Betrachtungsweise von Bewegungen*. GRIN Verlag, München, 2003.
- [41] H. De Marées. *Sportphysiologie*. Köln: Sport und Buch Strauß, 2002.
- [42] C. J. De Ruitter, D. A. Jones, A. J. Sargeant, and A. De Haan. Temperature effects on the rates of isometric force development and relaxation in the fresh and fatigued human adductor pollicis muscle. *Experimental Physiology*, 84(6):1137–1150, 1999.
- [43] V. Decostre, P. Bianco, V. Lombardi, and G. Piazzesi. Effect of temperature on the working stroke of muscle myosin. *Proceedings of the National Academy of Sciences*, 102(39):13927–13932, 2005.
- [44] E. I. Dedkov, T. Y. Kostrominova, A. B. Borisov, and B. M. Carlson. Reparative myogenesis in long-term denervated skeletal muscles of adult rats results in a reduction of the satellite cell population. *The Anatomical Record: An Official Publication of the American Association of Anatomists*, 263(2):139–154, 2001.
- [45] A. Dorfmann and A. Muhr. *Constitutive models for rubber*. CRC Press, 1999.
- [46] A. N. Doudoumoroulos and P. O. Chatfield. Effects of temperature on function of mammalian (rat) muscle. *American Journal of Physiology*, 196(6):1197–1199, 1959.
- [47] D. O. Draper, S. T. Harris, S. Schulthies, E. Durrant, K. L. Knight, and M. Ricard. Hot-pack and 1-MHz ultrasound treatments have an additive effect on muscle temperature increase. *Journal of Athletic Training*, 33(1):21–24, 1998.
- [48] D. O. Draper, C. Mahaffey, D. Kaiser, D. Eggett, and J. Jarmin. Thermal ultrasound decreases tissue stiffness of trigger points in upper trapezius muscles. *Physiotherapy Theory and Practice*, 26(3):167–172, 2010.
- [49] C. Duan, M. D. Delp, D. A. Hayes, P. D. Delp, and R. B. Armstrong. Rat skeletal muscle mitochondrial [Ca²⁺] and injury from downhill walking. *Journal of Applied Physiology*, 68(3):1241–1251, 1990.
- [50] F. A. Duck. *Physical properties of tissues - A comprehensive reference book*. Academic Press, San Diego, CA, 1990.
- [51] K. A. P. Edman. Double-hyperbolic force-velocity relation in frog muscle fibres. *Journal of Physiology*, 404(1):301–321, 1988.

- [52] A. E. Ehret, M. Böl, and M. Itskov. A continuum constitutive model for the active behaviour of skeletal muscle. *Journal of the Mechanics and Physics of Solids*, 59(3):625–636, 2011.
- [53] J. Ekstrand, M. Hägglund, and M. Waldén. Injury incidence and injury patterns in professional football: The UEFA injury study. *British Journal of Sports Medicine*, 45(7):553–558, 2011.
- [54] M. A. El-Brawany, D. K. Nassiri, G. Terhaar, A. Shaw, I. Rivens, and K. Lozhken. Measurement of thermal and ultrasonic properties of some biological tissues. *Journal of Medical Engineering and Technology*, 33(3):249–256, 2009.
- [55] M. H. Elmubarak and K. W. Ranatunga. Temperature sensitivity of tension development in a fast-twitch muscle of the rat. *Muscle and Nerve: Official Journal of the American Association of Electrodiagnostic Medicine*, 7(4):298–303, 1984.
- [56] M. Engelhardt. *Sportverletzungen*. 2006.
- [57] B. R. Epstein and K. R. Foster. Anisotropy in the dielectric properties of skeletal muscle. *Medical & Biological Engineering & Computing*, 21(1):51–55, 1983.
- [58] W. S. Erdmann and T. Gos. Density of trunk tissues of young and medium age people. *Journal of Biomechanics*, 23(9):945–947, 1990.
- [59] M. A. Fahmy. Boundary element modeling and simulation algorithm for fractional biothermomechanical problems of anisotropic soft tissues. In *Recent Developments in the Solution of Nonlinear Differential Equations*. InTech Open, 2021.
- [60] J. W. Fernandez, M. L. Buist, D. P. Nickerson, and P. J. Hunter. Modelling the passive and nerve activated response of the rectus femoris muscle to a flexion loading: A finite element framework. *Medical Engineering & Physics*, 27(10):862–870, 2005.
- [61] P. Fratzl. *Collagen*. 2008.
- [62] P. Fratzl and R. Weinkamer. Nature’s hierarchical materials. *Progress in Materials Science*, 52(8):1263–1334, nov 2007.
- [63] J. Fridén. Changes in human skeletal muscle induced by long-term eccentric exercise. *Cell and Tissue Research*, 236(2):365–372, 1984.
- [64] J. Fridén and R. L. Lieber. Structural and mechanical basis of exercise-induced muscle injury. *Medicine and Science in Sports and Exercise*, 24(5):521–530, 1992.
- [65] J. Fridén, M. Sjöström, and B. Ekblom. A morphological study of delayed muscle soreness. *Experientia*, 37(5):506–507, 1981.
- [66] J. A. Friederich and R. A. Brand. Muscle fiber architecture in the human lower limb. *Journal of Biomechanics*, 23(1):91–95, 1990.

- [67] T. Funatsu, E. Kono, H. Higuchi, S. Kimura, S. Ishiwata, T. Yoshioka, K. Maruyama, and S. Tsukita. Elastic filaments in situ in cardiac muscle: Deep-etch replica analysis in combination with selective removal of actin and myosin filaments. *The Journal of Cell Biology*, 120(3):711–724, 1993.
- [68] Y. Gao, T. Y. Kostrominova, J. A. Faulkner, and A. S. Wineman. Age-related changes in the mechanical properties of the epimysium in skeletal muscles of rats. *Journal of Biomechanics*, 41(2):465–469, 2008.
- [69] Y. Gao, A. M. Waas, and A. S. Wineman. Mechanics of injury to muscle fibers. *Journal of Mechanics in Medicine and Biology*, 7(04):381–394, 2007.
- [70] Y. Gao, A. S. Wineman, and A. M. Waas. Mechanics of muscle injury induced by lengthening contraction. *Annals of Biomedical Engineering*, 36(10):1615–1623, 2008.
- [71] A. Garo, P. J. Arnoux, E. Wagnac, and C. E. Aubin. Calibration of the mechanical properties in a finite element model of a lumbar vertebra under dynamic compression up to failure. *Medical & Biological Engineering & Computing*, 49(12):1371–1379, 2011.
- [72] W. E. Garrett, P. K. Nikolaou, B. M. Ribbeck, R. R. Glisson, and A. V. Seaber. The effect of muscle architecture on the biomechanical failure properties of skeletal muscle under passive extension. *The American Journal of Sports Medicine*, 16(1):7–12, 1988.
- [73] W. E. Garrett JR, M. R. Safran, A. V. Seaber, R. R. Glisson, and B. M. Ribbeck. Biomechanical comparison of stimulated and nonstimulated skeletal muscle pulled to failure. *The American Journal of Sports Medicine*, 15(5):448–454, 1987.
- [74] S. H. Gilbert and L. E. Ford. The thermoelastic effect in rigor muscle of the frog. *Journal of Muscle Research and Cell Motility*, 7(1):35–46, 1986.
- [75] A. R. Gillies and R. L. Lieber. Structure and function of the skeletal muscle extracellular matrix. *Muscle and Nerve*, 44(3):318–331, 2011.
- [76] S. K. Godunov. A difference method for numerical calculation of discontinuous solutions of the equations of hydrodynamics. *Matematicheskii Sbornik*, 89(3):271–306, 1959.
- [77] Y. E. Goldman, J. A. Mc Cray, and K. W. Ranatunga. Transient tension changes initiated by laser temperature jumps in rabbit psoas muscle fibres. *Journal of Physiology*, 392(1):71–95, 1987.
- [78] A. M. Gordon, A. F. Huxley, and F. J. Julian. The variation in isometric tension with sarcomere length in vertebrate muscle fibres. *The Journal of Physiology*, 184(1):170–192, 1966.

- [79] G. E. Goslow, W. E. Cameron, and D. G. Stuart. Ankle flexor muscles in the cat: Length-active tension and muscle unit properties as related to locomotion. *Journal of Morphology*, 153(1):23–37, 1977.
- [80] H. Granzier and S. Labeit. Cardiac titin: an adjustable multi-functional spring. *The Journal of Physiology*, 541(2):335–342, 2002.
- [81] H. Granzier and S. Labeit. Structure-function relations of the giant elastic protein titin in striated and smooth muscle cells. *Muscle and Nerve*, 36(6):740–755, 2007.
- [82] R. W. Gülch. Force-velocity relations in human skeletal muscle. *International Journal of Sports Medicine*, 15(S1):S2–S10, 1994.
- [83] M. Günther and S. Schmitt. A macroscopic ansatz to deduce the Hill relation. *Journal of Theoretical Biology*, 263(4):407–418, 2010.
- [84] C. T. Hasselman, T. M. Best, A. V. Seaber, and W. E. Garrett. A threshold and continuum of injury during active stretch of rabbit skeletal muscle. *The American Journal of Sports Medicine*, 23(1):65–73, 1995.
- [85] M. Haug, B. Reischl, G. Prölb, C. Pollmann, T. Buckert, C. Keidel, S. Schürmann, M. Hock, S. Rupitsch, M. Heckel, T. Pöschel, T. Scheibel, C. Haynl, L. Kiriaev, SI Head, and O. Friedrich. The MyoRobot: A novel automated biomechatronics system to assess voltage/Ca²⁺ biosensors and active/passive biomechanics in muscle and biomaterials. *Biosensors and Bioelectronics*, 102:589–599, 2018.
- [86] T. Heidlauf, T. Klotz, C. Rode, E. Altan, C. Bleiler, T. Siebert, and O. Röhrle. A multi-scale continuum model of skeletal muscle mechanics predicting force enhancement based on actin – titin interaction. *Biomechanics and Modeling in Mechanobiology*, 15(6):1423–1437, 2016.
- [87] T. Heidlauf and O. Röhrle. Modeling the chemoelectromechanical behavior of skeletal muscle using the parallel open-source software library openCMISS. *Computational and Mathematical Methods in Medicine*, 2013:14 pages, 2013.
- [88] T. Heidlauf and O. Röhrle. A multiscale chemo-electro-mechanical skeletal muscle model to analyze muscle contraction and force generation for different muscle fiber arrangements. *Frontiers in Physiology*, 5:498, 2014.
- [89] F. C. Henriques JR and A. R. Moritz. Studies of thermal injury: I. The conduction of heat to and through skin and the temperatures attained therein. A theoretical and an experimental investigation. *The American Journal of Pathology*, 23(5):530–549, 1947.
- [90] B. Hernández-Gascón, J. Grasa, B. Calvo, and J. F. Rodríguez. A 3D electro-mechanical continuum model for simulating skeletal muscle contraction. *Journal of Theoretical Biology*, 335:108–118, 2013.

- [91] W. Herzog. *Skeletal muscle mechanics: from mechanisms to function*. 2000.
- [92] W. Herzog, M. Duvall, and T. R. Leonard. Molecular mechanisms of muscle force regulation: a role for titin? *Exercise and Sport Sciences Reviews*, 40(1):50–57, 2012.
- [93] A. V. Hill. The heat of shortening and the dynamic constants of muscle. *Proceedings of the Royal Society of London. Series B - Biological Sciences*, 126(843):136–195, 1938.
- [94] A. V. Hill. *First and last experiments in muscle mechanics*. 1970.
- [95] A. V. Hill and W. Hartree. The thermo-elastic properties of muscle. *Philosophical Transactions of the Royal Society of London. Series B, Containing Papers of a Biological Character*, 210(372-381):153–173, 1921.
- [96] J. E. Hill, J. D. Leitman, and J. E. Sunderland. Thermal conductivity of various meats. *Food Technology*, 21(8):1143, 1967.
- [97] H. K. Huang and S. C. Wu. The evaluation of mass densities of the human body in vivo from CT Scans. *Computers in Biology and Medicine*, 6(4):337–343, 1976.
- [98] A. F. Huxley. Muscle structure and theories of contraction. *Progress in Biophysics and Biophysical Chemistry*, 7:255–318, 1957.
- [99] A. F. Huxley. Muscular contraction. *The Journal of Physiology*, 243(1):1–43, 1974.
- [100] H. E. Huxley. Electron microscope studies of the organisation of the filaments in striated muscle. *Biochimica et Biophysica Acta*, 12(1-2):387–394, 1953.
- [101] H. E. Huxley. The mechanism of muscular contraction: Recent structural studies suggest a revealing model for cross-bridge action at variable filament spacing. *Science*, 164(3886):1356–1366, 1969.
- [102] H. E. Huxley. Fifty years of muscle and the sliding filament hypothesis. *European Journal of Biochemistry*, 271(8):1403–1415, 2004.
- [103] D. Ito, E. Tanaka, and S. Yamamoto. A novel constitutive model of skeletal muscle taking into account anisotropic damage. *Journal of the Mechanical Behavior of Biomedical Materials*, 3(1):85–93, 2010.
- [104] R. S. James. A review of the thermal sensitivity of the mechanics of vertebrate skeletal muscle. *Journal of Comparative Physiology B: Biochemical, Systemic, and Environmental Physiology*, 183(6):723–733, 2013.
- [105] T. A. H. Järvinen, T. L. N. Järvinen, M. Kääriäinen, H. Kalimo, and M. Järvinen. Muscle injuries: Biology and treatment. *The American Journal of Sports Medicine*, 33(5):745–764, 2005.

- [106] G. Jenkins and G. Tortora. *Anatomy and physiology*. Wiley, 2016.
- [107] B. Ji and H. Gao. Mechanical Principles of Biological Nanocomposites. *Annual Review of Materials Research*, 40:77–100, 2010.
- [108] T. Johansson, P. Meier, and R. Blickhan. A finite-element model for the mechanical analysis of skeletal muscles. *Journal of Theoretical Biology*, 206(1):131–149, 2000.
- [109] I. A. Johnston and B. D. Sidell. Differences in temperature dependence of muscle contractile properties and myofibrillar ATPase activity in a cold-temperate fish. *Journal of Experimental Biology*, 111(1):179–189, 1984.
- [110] M. Kammoun, R. Ternifi, V. Dupres, P. Pouletaut, S. Môme, W. Môme, F. Szeremeta, J. Landoulsi, J.-M. Constans, F. Lafont, M. Subramaniam, J. R. Hawse, and S. F. Bensamoun. Development of a novel multiphysical approach for the characterization of mechanical properties of musculotendinous tissues. *Scientific Reports*, 9(1):7733, 2019.
- [111] F. Karami and Y. Tadesse. Modeling of twisted and coiled polymer (TCP) muscle based on phenomenological approach. *Smart Materials and Structures*, 26(12):125010, 2017.
- [112] T. Kashiwagi, J. N. McClure, and R. D. Wetzel. Headache and psychiatric disorders. *Diseases of the Nervous System*, 33(10):659–663, 1972.
- [113] K. Kometani and K. Yamada. Thermoelastic effect in chemically skinned frog skeletal muscle in rigor. *The Japanese Journal of Physiology*, 34(3):389–396, 1984.
- [114] J. F. Kragh, S. J. Svoboda, J. C. Wenke, D. E. Brooks, T. G. Bice, and T. J. Walters. The role of epimysium in suturing skeletal muscle lacerations. *Journal of the American College of Surgeons*, 200(1):38–44, 2005.
- [115] R. Kuravi, K. Leichsenring, R. Trostorf, E. Morales-Orcajo, M. Böl, and A. E. Ehret. Predicting muscle tissue response from calibrated component models and histology-based finite element models. *Journal of the mechanical behavior of biomedical materials*, 117:104375, 2021.
- [116] C. D. Kuthe and R. V. Uddanwadiker. Investigation of effect of fiber orientation on mechanical behavior of skeletal muscle. *Journal of Applied Biomaterials and Functional Materials*, 14(2):e154–e162, 2016.
- [117] D. Labeit, K. Watanabe, C. Witt, H. Fujita, Y. Wu, S. Lahmers, T. Funck, S. Labeit, and H. Granzier. Calcium-dependent molecular spring elements in the giant protein titin. *Proceedings of the National Academy of Sciences*, 100(23):13716–13721, 2003.
- [118] J. Lamsfuss and S. Bargmann. Skeletal muscle: Modeling the mechanical behavior by taking the hierarchical microstructure into account. *Journal of the Mechanical Behavior of Biomedical Materials*, 122:104670, 2021.

- [119] J. Lamsfuss and S. Bargmann. Computational modeling of damage in the hierarchical microstructure of skeletal muscles. *Journal of the Mechanical Behavior of Biomedical Materials*, 134:105386, 2022.
- [120] J. Lamsfuss and S. Bargmann. Python codes to generate skeletal muscle models on each hierarchical level. *Software Impacts*, 14:100437, 2022.
- [121] J. Lamsfuss and S. Bargmann. Mechanisms of thermal treatments in trigger points of the skeletal muscle: Computational microstructural modeling. *European Journal of Mechanics - A/Solids*, 99:104906, 2023.
- [122] J. C. Lee, D. T. Lin, and C. Z. Hong. The effectiveness of simultaneous thermotherapy with ultrasound and electrotherapy with combined AC and DC current on the immediate pain relief of myofascial trigger points. *Journal of Musculoskeletal Pain*, 5(1):81–90, 1997.
- [123] G. J. Lewis and P. P. Purslow. The strength and stiffness of perimysial connective tissue isolated from cooked beef muscle. *Meat Science*, 26(4):255–269, 1989.
- [124] R. L. Lieber. Skeletal muscle adaptability. I: Review of basic properties. *Development Medicine & Child Neurology*, 28(3):390–397, 1986.
- [125] R. L. Lieber, B. M. Fazeli, and M. J. Botte. Architecture of selected wrist flexor and extensor muscles. *The Journal of hand surgery*, 15(2):244–250, 1990.
- [126] R. L. Lieber and J. Fridén. Muscle damage is not a function of muscle force but active muscle strain. *Journal of Applied Physiology*, 74(2):520–526, 1993.
- [127] R. L. Lieber and J. Fridén. Functional and clinical significance of skeletal muscle architecture. *Muscle & Nerve: Official Journal of the American Association of Electrodiagnostic Medicine*, 23(11):1647–1666, 2000.
- [128] R. L. Lieber, M. D. Jacobson, B. M. Fazeli, R. A. Abrams, and M. J. Botte. Architecture of selected muscles of the arm and forearm: Anatomy and implications for tendon transfer. *Journal of Hand Surgery*, 17(5):787–798, 1992.
- [129] R. L. Lieber, E. Runesson, F. Einarsson, and J. Fridén. Inferior mechanical properties of spastic muscle bundles due to hypertrophic but compromised extracellular matrix material. *Muscle & Nerve*, 28(4):464–471, 2003.
- [130] R. L. Lieber, T. M. Woodburn, and J. Fridén. Muscle damage induced by eccentric contractions of 25% strain. *Journal of Applied Physiology*, 70(6):2498–2507, 1991.
- [131] W. A. Linke and M. Krüger. The giant protein titin as an integrator of myocyte signaling pathways. *Physiology*, 25(3):186–198, 2010.

- [132] H. Maas and T. G. Sandercock. Force transmission between synergistic skeletal muscles through connective tissue linkages. *Journal of Biomedicine and Biotechnology*, 2010:575672, 2010.
- [133] L. Marcucci, C. Reggiani, A. N. Natali, and P. G. Pavan. From single muscle fiber to whole muscle mechanics: a finite element model of a muscle bundle with fast and slow fibers. *Biomechanics and Modeling in Mechanobiology*, 16(6):1833–1843, 2017.
- [134] A. McBride, S. Bargmann, D. Pond, and G. Limbert. Thermoelastic modelling of the skin at finite deformations. *Journal of Thermal Biology*, 62:201–209, 2016.
- [135] K. K. McCully and J. A. Faulkner. Injury to skeletal muscle fibers of mice following lengthening contractions. *Journal of Applied Physiology*, 59(1):119–126, 1985.
- [136] M. P. McHugh and T. F. Tyler. Muscle strain injury vs muscle damage: Two mutually exclusive clinical entities. *Translational Sports Medicine*, 2(3):102–108, 2019.
- [137] R. L. Mcintosh and V. Anderson. A comprehensive tissue properties database provided for the thermal assessment of a human at rest. *Biophysical Reviews and Letters*, 5(03):129–151, 2010.
- [138] G. A. Meyer and R. L. Lieber. Elucidation of extracellular matrix mechanics from muscle fibers and fiber bundles. *Journal of Biomechanics*, 23(1):1–7, 2011.
- [139] G. A. Meyer, A. D. McCulloch, and R. L. Lieber. A Nonlinear Model of Passive Muscle Viscosity. *Journal of Biomechanical Engineering*, 133(9):1–9, 2011.
- [140] A. Minajeva, M. Kulke, J. M. Fernandez, and W. A. Linke. Unfolding of titin domains explains the viscoelastic behavior of skeletal myofibrils. *Biophysical Journal*, 80(3):1442–1451, 2001.
- [141] M. Murugesan and D. W. Jung. Johnson Cook material and failure model parameters estimation of AISI-1045 medium carbon steel for metal forming applications. *Materials*, 12(4):609, 2019.
- [142] G. Mutungi, P. Purslow, and C. Warkup. Structural and mechanical changes in raw and cooked single porcine muscle fibres extended to fracture. *Meat Science*, 40(2):217–234, 1995.
- [143] G. Mutungi and K. W. Ranatunga. Temperature-dependent changes in the viscoelasticity of intact resting mammalian (rat) fast- and slow-twitch muscle fibres. *Journal of Physiology*, 508(1):253–265, 1998.
- [144] S. F. Nadler, K. Weingand, and R. J. Kruse. The physiologic basis and clinical applications of cryotherapy and thermotherapy for the pain practitioner. *Pain Physician*, 7(3):395–400, 2004.

- [145] D. J. Newham, G. McPhail, K. R. Mills, and R. H. T. Edwards. Ultrastructural changes after concentric and eccentric contractions of human muscle. *Journal of the Neurological Sciences*, 61(1):109–122, 1983.
- [146] P. K. Nikolaou, B. L. Macdonald, R. R. Glisson, A. V. Seaber, and W. E. Garrett JR. Biomechanical and histological evaluation of muscle after controlled strain injury. *The American Journal of Sports Medicine*, 15(1):9–14, 1987.
- [147] K. C. Nishikawa, J. A. Monroy, T. E. Uyeno, S. H. Yeo, D. K. Pai, and S. L. Lindstedt. Is titin a 'winding filament'? A new twist on muscle contraction. *Proceedings of the Royal Society B: Biological Sciences*, 279(1730):981–990, 2012.
- [148] T. J. Noonan, T. M. Best, A. V. Seaber, and W. E. Garrett. Identification of a threshold for skeletal muscle injury. *The American Journal of Sports Medicine*, 22(2):257–261, 1994.
- [149] T. J. Noonan, T. M. Best, A. V. Seaber, and W. E. Garrett JR. Thermal effects on skeletal muscle tensile behavior. *The American Journal of Sports Medicine*, 21(4):517–522, 1993.
- [150] T. J. Noonan and W. E. Garrett JR. Muscle strain injury: diagnosis and treatment. *JAAOS-Journal of the American Academy of Orthopaedic Surgeons*, 7(4):262–269, 1999.
- [151] Y. Okamoto and K. Saeki. Phase transition of collagen and gelatin. *Kolloid-Zeitschrift und Zeitschrift für Polymere*, 194(2):124–135, 1964.
- [152] C. W. J. Oomens, M. Maenhout, C. H. Van Oijen, M. R. Drost, and F. P. Baaijens. Finite element modelling of contracting skeletal muscle. *Philosophical Transactions of the Royal Society B: Biological Sciences*, 358(1437):1453–1460, 2003.
- [153] E. Passerieux, R. Rossignol, T. Letellier, and J. P. Delage. Physical continuity of the perimysium from myofibers to tendons: Involvement in lateral force transmission in skeletal muscle. *Journal of Structural Biology*, 159(1):19–28, 2007.
- [154] E. Pate and R. Cooke. A model of crossbridge action: the effects of ATP, ADP and Pi. *Journal of Muscle Research & Cell Motility*, 10(3):181–196, 1989.
- [155] S. E. Peters. Structure and function in vertebrate skeletal muscle. *Integrative and Comparative Biology*, 29(1):221–234, 1989.
- [156] B. J. Petrof, J. B. Shrager, H. H. Stedman, A. M. Kelly, and H. L. Sweeney. Dystrophin protects the sarcolemma from stresses developed during muscle contraction. *Proceedings of the National Academy of Sciences of the United States of America*, 90(8):3710–3714, 1993.
- [157] J. Petrofsky, M. Laymon, and H. Lee. Local heating of trigger points reduces neck and plantar fascia pain. *Journal of Back and Musculoskeletal Rehabilitation*, 33(1):21–28, 2020.

- [158] W. Pfuhl. Die gefiederten Muskeln, ihre Form und ihre Wirkungsweise. *Zeitschrift für Anatomie und Entwicklungsgeschichte*, 106(6):749–769, 1937.
- [159] B. Pillet, P. Badel, P. Edouard, and B. Pierrat. Hamstring muscles rupture under traction, peeling and shear lap tests: A biomechanical study in rabbits. *Journal of the Mechanical Behavior of Biomedical Materials*, 116:104324, 2021.
- [160] H. F. Poppendiek, R. Randall, J. A. Breeden, J. E. Chambers, and J. R. Murphy. Thermal conductivity measurements and predictions for biological fluids and tissues. *Cryobiology*, 3(4):318–327, 1967.
- [161] K. Powers, G. Schappacher-Tilp, A. Jinha, T. Leonard, K. Nishikawa, and W. Herzog. Titin force is enhanced in actively stretched skeletal muscle. *Journal of Experimental Biology*, 217(20):3629–3636, 2014.
- [162] W. E. Prentice JR. An electromyographic analysis of the effectiveness of heat or cold and stretching for inducing relaxation in injured muscle. *Journal of Orthopaedic and Sports Physical Therapy*, 3(3):133–140, 1982.
- [163] A. Price, A. Edgerton, C. Cocaud, H. Naguib, and A. Jnifene. A study on the thermo-mechanical properties of shape memory alloys-based actuators used in artificial muscles. *Journal of Intelligent Material Systems and Structures*, 18(1):11–18, 2007.
- [164] A. J. Pullan, M. L. Buist, and L. K. Cheng. *Mathematically modelling the electrical activity of the heart: From cell to body surface and back again*. 2005.
- [165] P. P. Purslow. Strain-induced reorientation of an intramuscular connective tissue network: Implications for passive muscle elasticity. *Journal of Biomechanics*, 22(1):21–31, 1989.
- [166] P. P. Purslow and J. A. Trotter. The morphology and mechanical properties of endomysium in series-fibred muscles: variations with muscle length. *Journal of Muscle Research & Cell Motility*, 15(3):299–308, 1994.
- [167] P. P. Purslow, T. J. Wess, and D. W. L. Hukins. Collagen orientation and molecular spacing during creep and stress-relaxation in soft connective tissues. *Journal of Experimental Biology*, 201(1):135–142, 1998.
- [168] J. A. Rall and R. C. Woledge. Influence of temperature on mechanics and energetics of muscle contraction. *American Journal of Physiology-Regulatory, Integrative and Comparative Physiology*, 259(2):R197–R203, 1990.
- [169] K. W. Ranatunga. Thermal stress and Ca-independent contractile activation in mammalian skeletal muscle fibers at high temperatures. *Biophysical Journal*, 66(5):1531–1541, 1994.
- [170] K. W. Ranatunga. Force and power generating mechanism(s) in active muscle as revealed from temperature perturbation studies. *Journal of Physiology*, 588(19):3657–3670, 2010.

- [171] K. W. Ranatunga, B. Sharpe, and B. Turnbull. Contractions of a human skeletal muscle at different temperatures. *The Journal of Physiology*, 390(1):383–395, 1987.
- [172] K. W. Ranatunga and S. R. Wylie. Temperature-dependent transitions in isometric contractions of rat muscle. *Journal of Physiology*, 339(1):87–95, 1983.
- [173] M. V. Razumova, A. E. Bukatina, and K. B. Campbell. Stiffness-distortion sarcomere model for muscle simulation. *Journal of Applied Physiology*, 87(5):1861–1876, 1999.
- [174] N. Rech. Intramuscular temperature of rectus femoris during cold water immersion. *All Graduate Plan b and Other Reports*, 255, 2013.
- [175] M. R. Rehorn, A. K. Schroer, and S. S. Blemker. The passive properties of muscle fibers are velocity dependent. *Journal of Biomechanics*, 47(3):687–693, 2014.
- [176] H. Reichel. *Muskelfysiologie*. 1960.
- [177] B. Reid, C. R. Slater, and G. S. Bewick. Synaptic vesicle dynamics in rat fast and slow motor nerve terminals. *Journal of Neuroscience*, 19(7):2511–2521, 1999.
- [178] D. Remache, M. Semaan, J. M. Rossi, M. Pithioux, and J. L. Milan. Application of the Johnson-Cook plasticity model in the Finite Element simulations of the nanoindentation of the cortical bone. *Journal of the Mechanical Behavior of Biomedical Materials*, 101:103426, 2020.
- [179] S. M. Roche, J. P. Gumucio, S. V. Brooks, C. L. Mendias, and D. R. Clafin. Measurement of maximum isometric force generated by permeabilized skeletal muscle fibers. *Journal of Visualized Experiments*, (100):e52695, 2015.
- [180] C. Rode, T. Siebert, R. Blickhan, C. Rode, T. Siebert, and R. Blickhan. Titin-induced force enhancement and force depression: A ‘sticky-spring’ mechanism in muscle contractions? *Journal of Theoretical Biology*, 259(2):350–360, 2009.
- [181] O. Röhrle, J. B. Davidson, and A. J. Pullan. Bridging scales: A three-dimensional electromechanical finite element model of skeletal muscle. *SIAM Journal on Scientific Computing*, 30(6):2882–2904, 2008.
- [182] R. W. D. Rowe. Morphology of perimysial and endomysial connective tissue in skeletal muscle. *Tissue and Cell*, 13(4):681–690, 1981.
- [183] A. K. Royce. *The effectiveness of cryotherapy versus thermotherapy post-dry needling on active myofascial trigger points in the infraspinatus muscle*. PhD thesis, University of Johannesburg (South Africa), 2012.
- [184] A. Ryan. Quadriceps strain, rupture and charlie horse. *Medicine and Science in Sports*, 1(2):106–111, 1969.

- [185] A. J. Sargeant. Effect of muscle temperature on leg extension force and short-term power output in humans. *European Journal of Applied Physiology*, 56(6):693–698, 1987.
- [186] S. Schleifenbaum, M. Schmidt, R. Möbius, T. Wolfskämpf, C. Schröder, R. Grunert, N. Hammer, and T. Prietzel. Load and failure behavior of human muscle samples in the context of proximal femur replacement. *BMC Musculoskeletal Disorders*, 17(1):1–7, 2016.
- [187] R. Schleip, T. W. Findley, L. Chaitow, and P. Huijing. *Fascia: the tensional network of the human body-e-book: the science and clinical applications in manual and movement therapy*. Elsevier Health Sciences, 2013.
- [188] H. Schmalbruch. *Skeletal muscle*. 1985.
- [189] D. Schneidereit, S. Nübler, G. Prölb, B. Reischl, S. Schürmann, O. J. Müller, and O. Friedrich. Optical prediction of single muscle fiber force production using a combined biomechanics and second harmonic generation imaging approach. *Light: Science and Applications*, 7(1):1–14, 2018.
- [190] H. R. C. Screen, D. A. Lee, D. L. Bader, and J. C. Shelton. An investigation into the effects of the hierarchical structure of tendon fascicles on micromechanical properties. *Proceedings of the Institution of Mechanical Engineers, Part H: Journal of Engineering in Medicine*, 218(2):109–119, 2004.
- [191] S. S. Segal, J. A. Faulkner, and T. P. White. Skeletal muscle fatigue in vitro is temperature dependent. *Journal of Applied Physiology*, 61(2):660–665, 1986.
- [192] D. Sen and M. J. Buehler. Structural hierarchies define toughness and defect-tolerance despite simple and mechanically inferior brittle building blocks. *Scientific Reports*, 1:1–9, 2011.
- [193] S. B. Shah, J. M. Love, A. O’Neill, R. M. Lovering, and R. J. Bloch. Influences of desmin and keratin 19 on passive biomechanical properties of mouse skeletal muscle. *Journal of Biomedicine and Biotechnology*, 2012:12, 2012.
- [194] B. Sharafi, E. G. Ames, J. W. Holmes, and S. S. Blemker. Strains at the myotendinous junction predicted by a micromechanical model. *Journal of Biomechanics*, 44(16):2795–2801, 2011.
- [195] B. Sharafi and S. S. Blemker. A micromechanical model of skeletal muscle to explore the effects of fiber and fascicle geometry. *Journal of Biomechanics*, 43(16):3207–3213, 2010.
- [196] S. Sharafi and G. Li. A multiscale approach for modeling actuation response of polymeric artificial muscles. *Soft Matter*, 11(19):3833–3843, 2015.
- [197] J. Sharkey. *The concise book of neuromuscular therapy: A trigger point manual*. North Atlantic Books, 2008.

- [198] W. Shen, J. Zhang, and F. Yang. Modeling and numerical simulation of bioheat transfer and biomechanics in soft tissue. *Mathematical and Computer Modelling*, 41(11-12):1251–1265, 2005.
- [199] P. R. Shorten, P. O’Callaghan, J. B. Davidson, and T. K. Soboleva. A mathematical model of fatigue in skeletal muscle force contraction. *Journal of Muscle Research and Cell Motility*, 28(6):293–313, 2007.
- [200] J. C. Simo. On a fully three-dimensional finite-strain viscoelastic damage model: Formulation and computational aspects. *Computer Methods in Applied Mechanics and Engineering*, 60(2):153–173, 1987.
- [201] D. G. Simons and S. Mense. Understanding and measurement of muscle tone as related to clinical muscle pain. *Pain*, 75(1):1–17, 1998.
- [202] L. A. Spyrou, M. Agoras, and K. Danas. A homogenization model of the Voigt type for skeletal muscle. *Journal of Theoretical Biology*, 414:50–61, 2017.
- [203] L. A. Spyrou, S. Brisard, and K. Danas. Multiscale modeling of skeletal muscle tissues based on analytical and numerical homogenization. *Journal of the mechanical behavior of biomedical materials*, 92:97–117, 2019.
- [204] M. Stefanati, C. Villa, Y. Torrente, and J. F. Rodriguez Matas. A mathematical model of healthy and dystrophic skeletal muscle biomechanics. *Journal of the Mechanics and Physics of Solids*, 134:103747, 2020.
- [205] U. Stoecker, I. A. Telley, E. Stüssi, and J. Denoth. A multisegmental cross-bridge kinetics model of the myofibril. *Journal of Theoretical Biology*, 259(4):714–726, 2009.
- [206] S. F. Street. Lateral transmission of tension in frog myofibers: a myofibrillar network and transverse cytoskeletal connections are possible transmitters. *Journal of Cellular Physiology*, 114(3):346–364, 1983.
- [207] D. Taylor, N. O’Mara, E. Ryan, M. Takaza, and C. Simms. The fracture toughness of soft tissues. *Journal of the Mechanical Behavior of Biomedical Materials*, 6:139–147, 2012.
- [208] A. Teklemariam, E. Hodson-Tole, N. D. Reeves, and G. Cooper. A micromechanical muscle model for determining the impact of motor unit fiber clustering on force transmission in aging skeletal muscle. *Biomechanics and Modeling in Mechanobiology*, 18(5):1401–1413, 2019.
- [209] B. Tillmann. Binde und Stützgewebe des Bewegungsapparates. In *H. Leonhardt, B. Tillmann, G. Töndury, K. Zilles: Rauber/Kopsch, Anatomie des Menschen Bd III*, pages 14–49. Thieme, Stuttgart-New York, 1987.

- [210] K. Tittel. *Beschreibende und funktionelle Anatomie des Menschen*. München, Jena : Urban und Fischer, 2000.
- [211] A. Tomalka, C. Rode, J. Schumacher, and T. Siebert. The active force-length relationship is invisible during extensive eccentric contractions in skinned skeletal muscle fibres. *Proceedings of the Royal Society B: Biological Sciences*, 284(1854):20162497, 2017.
- [212] B. Tondu, S. Ippolito, J. Guiochet, and A. Daidie. A seven-degrees-of-freedom robot-arm driven by pneumatic artificial muscles for humanoid robots. *The International Journal of Robotics Research*, 24(4):257–274, 2005.
- [213] J. A. Trotter. Functional morphology of force transmission in skeletal muscle. *Cells Tissues Organs*, 146(4):205–222, 1993.
- [214] J. A. Trotter and P. P. Purslow. Functional morphology of the endomysium in series fibered muscles. *Journal of Morphology*, 212(2):109–122, 1992.
- [215] C. P. Tsui, C. Y. Tang, C. P. Leung, K. W. Cheng, Y. F. Ng, D. H. K. Chow, and C. K. Li. Active finite element analysis of skeletal muscle-tendon complex during isometric, shortening and lengthening contraction. *Bio-Medical Materials and Engineering*, 14(3):271–279, 2004.
- [216] P. Uebliacker, H. W. Müller-Wohlfahrt, and J. Ekstrand. Epidemiological and clinical outcome comparison of indirect ('strain') versus direct ('contusion') anterior and posterior thigh muscle injuries in male elite football players: UEFA Elite League study of 2287 thigh injuries (2001-2013). *British Journal of Sports Medicine*, 49(22):1461–1465, 2015.
- [217] G. J. van Ingen Schenau, M. F. Bobbert, G. J. Ettema, J. B. de Graaf, and P. A. Huijing. A simulation of rat edl force output based on intrinsic muscle properties. *Journal of Biomechanics*, 21(10):815–824, 1988.
- [218] R. Versluys, A. Desomer, G. Lenaerts, O. Pareit, B. Vanderborght, G. Perre, L. Peeraer, and D. Lefeber. A biomechatronical transtibial prosthesis powered by pleated pneumatic artificial muscles. *International Journal of Modelling, Identification and Control*, 4(4):394–405, 2008.
- [219] K. M. Virgilio, K. S. Martin, S. M. Peirce, and S. S. Blemker. Multiscale models of skeletal muscle reveal the complex effects of muscular dystrophy on tissue mechanics and damage susceptibility. *Interface Focus*, 5(2), 2015.
- [220] H. Vogel. A better way to construct the sunflower head. *Mathematical Biosciences*, 44(3-4):179–189, 1979.
- [221] H. Wagner and R. Blickhan. Stabilizing function of skeletal muscles: an analytical investigation. *Journal of Theoretical Biology*, 199(2):163–179, 1999.

- [222] K. Wang, R. McCarter, J. Wright, J. Beverly, and R. Ramirez-Mitchell. Viscoelasticity of the sarcomere matrix of skeletal muscles - The titin-myosin composite filament is a dual-stage molecular spring. *Biophysical Journal*, 64(4):1161–1177, 1993.
- [223] S. R. Ward, C. M. Eng, L. H. Smallwood, and R. L. Lieber. Are current measurements of lower extremity muscle architecture accurate? *Clinical Orthopaedics and Related Research*, 467(4):1074–1082, 2009.
- [224] S. R. Ward, T. M. Winters, S. M. O'Connor, and R. L. Lieber. Non-linear scaling of passive mechanical properties in fibers, bundles, fascicles and whole rabbit muscles. *Frontiers in Physiology*, 11:1–9, 2020.
- [225] G. Waycaster, S.-K. Wu, and X. Shen. Design and control of a pneumatic artificial muscle actuated above-knee prosthesis. *Journal of Medical Devices*, 5(3):9, 2011.
- [226] U. G. K. Wegst and M. F. Ashby. The mechanical efficiency of natural materials. *Philosophical Magazine*, 84(21):2167–2186, 2004.
- [227] J. Weickenmeier, M. Itskov, E. Mazza, and M. Jabareen. A physically motivated constitutive model for 3D numerical simulation of skeletal muscles. *International Journal for Numerical Methods in Biomedical Engineering*, 30(5):545–562, 2014.
- [228] J. Werner and M. Buse. Temperature profiles with respect to inhomogeneity and geometry of the human body. *Journal of Applied Physiology*, 65(3):1110–1118, 1988.
- [229] B. B. Wheatley, G. M. Odegard, K. R. Kaufman, and T. L. Haut Donahue. Modeling skeletal muscle stress and intramuscular pressure: A whole muscle active-passive approach. *Journal of Biomechanical Engineering*, 140(8):1–8, 2018.
- [230] M. E. T. Willems and P. P. Purslow. Mechanical and structural characteristics of single muscle fibres and fibre groups from raw and cooked pork Longissimus muscle. *Meat Science*, 46(3):285–301, 1997.
- [231] J. Wilmers and S. Bargmann. Nature's design solutions in dental enamel: Uniting high strength and extreme damage resistance. *Acta Biomaterialia*, 2020.
- [232] R. D. Woittiez, P. A. Huijing, and R. H. Rozendal. Influence of muscle architecture on the length-force diagram of mammalian muscle. *Pflügers Archiv European Journal of Physiology*, 399(4):275–279, 1983.
- [233] R. C. Woledge, C. J. Barclay, and N. A. Curtin. Temperature change as a probe of muscle crossbridge kinetics: a review and discussion. *Proceedings of the Royal Society B: Biological Sciences*, 276(1668):2685–2695, 2009.
- [234] R. C. Woledge, N. A. Curtin, and E. Homsher. Energetic aspects of muscle contraction. *Monographs of the physiological society*, 41:1–357, 1985.

- [235] H. G. Wolff. Headache and other head pain, 1963.
- [236] F. Xu, T. Wen, T. J. Lu, and K. A. Seffen. Skin biothermomechanics for medical treatments. *Journal of the Mechanical Behavior of Biomedical Materials*, 1(2):172–187, 2008.
- [237] C. Zhang and Y. Gao. Finite element analysis of mechanics of lateral transmission of force in single muscle fiber. *Journal of Biomechanics*, 45(11):2001–2006, 2012.
- [238] Y. Zhang, J.-S. Chen, Q. He, X. He, R. R. Basava, J. Hodgson, U. Sinha, and S. Sinha. Microstructural analysis of skeletal muscle force generation during aging. *Numerical Methods in Biomedical Engineering*, 36(1):e3295, 2020.
- [239] A. M. Zöllner, O. J. Abilez, M. Böhl, and E. Kuhl. Stretching skeletal muscle: chronic muscle lengthening through sarcomerogenesis. *PLoS ONE*, 7(10):e45661, 2012.
- [240] C. J. Zuurbier, J. W. Heslinga, M. B. E. Lee-de Groot, and W. J. Van der Laarse. Mean sarcomere length-force relationship of rat muscle fibre bundles. *Journal of Biomechanics*, 28(1):83–87, 1995.